UNIVERSITY OF BIRMINGHAM

Machine Learning Enabled Intelligent Microfluidics for Bioparticle Detection and Monitoring

by

JIAHAO ZHENG

A thesis submitted to the University of Birmingham for the degree of

DOCTOR IN PHILOSOPHY

Department of Mechanical Engineering

School of Engineering

College of Engineering and Physical Sciences

The University of Birmingham

October 2024

ABSTRACT

Traditional detection and monitoring methods in environmental and biomedical applications are often centralised, high-cost, and time-consuming, requiring specialised laboratories, complex instruments, and trained personnel. These limitations have been highlighted by recent global challenges such as disease control and environmental issues. The COVID-19 pandemic underscored the urgent need for decentralised, rapid, and accurate diagnostic tools. Additionally, environmental issues like climate change and its effect on public health demand real-time monitoring solutions that are accessible and efficient.

Microfluidics, as a multidisciplinary technology, offers significant advantages in developing low-cost, rapid, and portable testing platforms by integrating sample preparation, pretreatment, and detection into compact devices. Despite its potential, traditional microfluidic systems often struggle to fully meet the needs for decentralisation and affordability due to complex fabrication processes and the requirement for supporting analytical equipment. Concurrently, advancements in artificial intelligence, particularly machine learning (ML) and convolutional neural networks (CNNs), have revolutionised data processing and analysis in vision-based applications. Integrating microfluidics with ML, which forms intelligent microfluidics, holds the promise of retaining the benefits of microfluidic data collection while leveraging ML for efficient data analysis, optimisation, and improved detection methods.

The thesis presents the development of two innovative platforms. The first is an Automated and Intelligent Microfluidic Platform (AIMP) designed for environmental monitoring, specifically

for microalgae detection and analysis. Utilising components with total cost < £170 and a trained ML model, the AIMP demonstrated high accuracy in detecting and classifying various microalgae species, facilitating efficient and decentralised environmental surveillance.

The second platform is an Artificial Intelligence-Driven Point-of-Care Testing (AID-POCT) device for biomedical diagnostics. This platform employs magnetic microbeads coated with specific antibodies to capture target cytokines, forming distinct patterns under a magnetic field. By capturing and analysing these patterns using a mobile phone and a deployed ML model, the AID-POCT platform enables rapid and quantitative detection of biomarkers such as interferon-gamma, with demonstrated adaptability to detect other cytokines.

By overcoming the limitations of traditional methods, these intelligent microfluidic systems offer accessible, efficient, and accurate diagnostic solutions. The thesis lays the groundwork for the broader adoption of intelligent microfluidics, highlighting its transformative potential in environmental monitoring and healthcare.

ACKNOWLEDGEMENTS

First and foremost, I wish to express my profound gratitude to my leading supervisor, Dr. Shiyang Tang. It was his passion and dedication to scientific research that inspired me to embark on the journey of Ph.D. study. Whenever I felt lost, whether in my studies or life, he was always the first to unreservedly share his experiences with me and offer his selfless assistance. I feel incredibly fortunate to have met such an academic supervisor and life guide, both a mentor and a friend, at this pivotal stage of my life. No matter where life takes me in the future, I will always cherish his mentoring and help and take him as a role model to maintain my enthusiasm for life and work.

I also extend my heartfelt thanks to Dr. Chengchen Zhang from the University of Southampton. She has selflessly provided me with immense assistance and guidance in interdisciplinary research in bioengineering. Her professionalism commands my utmost respect. Moreover, whenever I faced difficulties in life, she was always there to lend a helping hand.

I would also like to express my gratitude to my other two supervisors at the University of Birmingham, Prof. Yi Wang and Dr. Nan Gao. Throughout the various stages of my Ph.D. study, they have provided me with sincere encouragement, valuable advice, and unwavering support.

Moreover, I wish to acknowledge the mentors and friends who have encouraged and supported me throughout my education journey: Prof. Weihua Li, Dr. Shuaishuai Sun, Dr. Dan Yuan, and Dr. Guolin Yun. Crossing paths with you at various times has provided me with role models and inspiration, empowering me with the courage and perseverance to pursue my dreams step by step.

I wish to thank my group mates and dear friends during my PhD studies: Yuxin Zhang, Bayinqiaoge, Tim Cole, Feifan Zhao, Yiwen Wu, Jitao Zhang, Lu Qian, and others. Your presence has made this period of my life more vibrant. I will forever treasure these unforgettable times.

Lastly, I wish to convey my deepest appreciation to my family, especially my parents, Mr. Wenwu Zheng and Mrs. Ping Zhang, and my fiancée, Ms. Zixuan Zhou. You have always been the pillar of my life and the source of my motivation.

TABLE OF CONTENTS

LIST OF PUBLICATIONS

Publications included in this thesis

1. **J. Zheng**, T. Cole, Y. Zhang, J. Kim and S.-Y. Tang (2021). "Exploiting machine learning for bestowing intelligence to microfluidics." Biosensors and Bioelectronics **194**: 113666. **(Chapter 3)**
2. **J. Zheng**, T. Cole, Y. Zhang, Bayinqiaoge, D. Yuan and S.-Y. Tang (2024). "An automated and intelligent microfluidic platform for microalgae detection and monitoring." Lab on a Chip **24**(2): 244-253. **(Chapter 4)**
3. **J. Zheng**, Y. Zhang, Bayinqiaoge, T. Cole, Y. Wang, S.-Y. Tang, and C. Zhang (2024). "Biomarker conjugation enabled microbead patterns for intelligent point-of-care biosensing." submitted for publication. **(Chapter 5)**

Other Publications during PhD

4. G. Yun, T. Cole, Y. Zhang, **J. Zheng**, S. Sun, Y. Ou-yang, J. Shu, H. Lu, Q. Zhang, Y. Wang, D. Pham, T. Hasan, W. Li, S. Zhang and S.-Y. Tang (2023). "Electro-mechano responsive elastomers with self-tunable conductivity and stiffness." Science Advances **9**(4): eadf1141.
5. Bayinqiaoge, Y. Zhang, T. Cole, **J. Zheng**, J. Guo and S.-Y. Tang (2023). "Recent advances in non-optical microfluidic platforms for bioparticle detection." Biosensors and Bioelectronics **222**: 114944.
6. Li, X., L. Cao, B. Xiao, F. Li, J. Yang, J. Hu, T. Cole, Y. Zhang, M. Zhang, **J. Zheng**, S. Zhang, W. Li, L. Sun, X. Chen and S.-Y. Tang (2022). "Superelongation of Liquid Metal." Advanced Science **9**(11): 2105289.
7. Y. Zhang, Y. Zhao, T. Cole, **J. Zheng**, Bayinqiaoge, J. Guo and S.-Y. Tang (2022). "Microfluidic flow cytometry for blood-based biomarker analysis." Analyst **147**(13): 2895-2917.
8. G. Yun, S.-Y. Tang, H. Lu, T. Cole, S. Sun, J. Shu, **J. Zheng**, Q. Zhang, S. Zhang, M. D Dickey and W. Li (2021). " Liquid metal hybrid composites with high-sensitivity and large dynamic range enabled by micro-and macrostructure engineering." ACS Applied Polymer Materials **3**(10): 5302-5315.
9. Y. Zhang., T. Cole, G. Yun, Y. Li, Q. Zhao, H. Lu, **J. Zheng**, W. Li and S.-Y. Tang (2021). "Modular and Self-Contained Microfluidic Analytical Platforms Enabled by Magnetorheological Elastomer Microactuators." Micromachines **12**(6): 604.

LIST OF FIGURES

LIST OF TABLES

LIST OF ABBREVIATIONS

AID-POCT – Artificial Intelligence-Driven Point-of-Care Testing (device)

AIMP – Automated and Intelligent Microfluidic Platform

APP – Application (smartphone or software "APP")

ASSURED – Affordable, Sensitive, Specific, User-friendly, Rapid & Robust, Equipment-free, and Deliverable (WHO criteria)

CNN / CNNs – Convolutional Neural Network(s)

COMSOL – COMSOL Multiphysics (simulation software)

CPU / CPUs – Central Processing Unit(s)

DHM – Digital Holographic Microscopy (if used as an acronym in text)

DNA – Deoxyribonucleic Acid

DNN / DNNs – Deep Neural Network(s)

DQN – Deep Q-Network (a reinforcement learning algorithm)

DRO – Deep Reaction Optimiser

ELISA – Enzyme-Linked Immunosorbent Assay

EM – Expectation Maximum

FOV – Field of View

FP – False Positive

FPGAs – Field-Programmable Gate Arrays

FPVA – Fully Programmable Valve Array

FN – False Negative

GBC – Gradient Boosting Classifier

GPU / **GPUs** – Graphics Processing Unit(s)

HABs – Harmful Algal Blooms

HDMR – High Dimensional Model Representation

HE4 – Human Epididymis Protein 4

HRP – Horseradish Peroxidase

HSV – Hue, Saturation, Value (colour space)

KNN – K-Nearest Neighbour (classifier)

LAMP – Loop-Mediated Isothermal Amplification

LDA – Linear Discriminant Analysis

LED – Light-Emitting Diode

LFA / **LFAs** – Lateral Flow Assay(s)

LR – Logistic Regression

LSTM – Long Short-Term Memory (recurrent neural network type)

MB / **MBs** – Magnetic Bead(s)

MDP – Markov Decision Process

ML – Machine Learning

MLP – Multilayer Perceptron

MSDN – Microalgae Species Detection Network

MUC4 – Mucin 4

NN – Neural Network

OCA – Optically Clear Adhesive

PCs – Personal Computers

PCA – Principal Component Analysis

PDAC – Pancreatic Ductal Adenocarcinoma

PDMS – Polydimethylsiloxane

PID – Proportional–Integral–Derivative (controller)

PLA – Polylactic Acid (3D printing filament)

POC – Point of Care

POCT / POCTs – Point-of-Care Testing (device)

PR – Precision–Recall

RF – Random Forest

RL – Reinforcement Learning

RNAi – RNA Interference

RNN – Recurrent Neural Network

SCD – Sickle Cell Disease

SEN – Sequential Encoder Network

SERS – Surface-Enhanced Raman Spectroscopy

SVM – Support Vector Machine

TN – True Negative

TNF – Tumour Necrosis Factor

TP – True Positive

TPUs – Tensor Processing Units

UFP / **UFPs** – Ultrafine Particle(s)

USB – Universal Serial Bus

VIFFI – Virtual-Freezing Fluorescence Imaging

VNC – Virtual Network Computing

VLSI – Very-Large-Scale Integration

YOLO – "You Only Look Once" models

XYZ – Denoting 3-axis (X, Y, Z)

1 CHAPTER 1: GENERAL INTRODUCTION

1.1 Background and Context

As early as the 17th century, Robert Hooke and Antoni van Leeuwenhoek, for the first time, observed microbes through a microscope, thereby opening the door to microbiology[1]. Until today, with the advancement of engineering technology in visual-based observation systems, we have been facilitated with more techniques to inspect, record and analyse the samples requiring detection. However, traditional detection and monitoring solutions frequently share the following challenges: 1) Centralisation, which necessitates the presence of laboratories or testing institutions with complex instruments to conduct the work; 2) High cost, which includes the high expenses associated with instrument manufacturing, sample transportation, and skilled personnel training; and 3) Time-consuming, which mainly caused by the extended time frame between sampling, inspection, and analysis of the results.

COVID-19, as a black swan event that happened a few years ago, illustrated the limitations of traditional testing pathways when facing the demand for large-scale diagnostic testing. The rapid spread of this virus posed critical challenges for public health worldwide[2]. As a result, the necessity of having a decentralised, rapid and precise diagnosis on a large scale has been highlighted[3, 4]. In addition to the threat of disease, we are facing a number of significant challenges arising from environmental factors. For example, the phenomenon of global warming is now an indisputable fact[5]. The year 2022 has been recorded as the hottest year in the UK since the commencement of temperature recording in 1884. Various climate changes

have increased the possibility of extreme conditions in surface water[6]. In this context, global monitoring of microalgae, especially harmful species, is essential to prevent harmful algal blooms (HABs) and to understand the connection between HABs and climate change[7]. It is therefore evident that there is a significant need for the utilisation of monitoring platforms that are capable of real-time environmental event monitoring with a high degree of accuracy.

Microfluidics is a multidisciplinary technology with the potential to transform numerous fields of research. It has already demonstrated its utility in several fields, including biotechnology[8-10], biomedical research[11-13], and environmental research[14-16]. Microfluidic chips, as a platform solution integrating basic testing operations such as sample preparation, pretreatment, and detection have the advantages of being low-cost, fast in test and small in size[17]. These advantages have shown its potential for advanced detection and monitoring technologies, such as point-of-care testing (POCT)[18]. POCT is expected to overcome the limitations of traditional detection and monitoring approaches (centralised testing, long waiting period, and high cost) as it has the potential to provide fast, simple and cost-effective diagnosis at or near the patient site, meeting the World Health Organisation's ‘ASSURED’ criteria (affordable, sensitive, specific, user-friendly, rapid and stable, device-independent and deliverable to the end user)[19].

Artificial intelligence (AI) was first proposed in 1956 at the Dartmouth Conference[20]. As a subset of AI, machine learning (ML), especially convolutional neural network (CNN)-based ML, has revolutionised data processing and analysing methods in vision-based applications[21].

A classic CNN network architecture for image-based tasks often includes a feature extractor with multiple convolutional layers and a fully connected classifier[22]. For example, the famous ResNet, which has been utilised in medical image processing[23], is built based on this classic architecture. ML has achieved remarkable success in interpreting and understanding visual data, especially complex data, as it can keep learning from the input dataset without explicit programming[24]. The analysis of complex images from massive datasets is a crucial aspect of various applications, including electroencephalogram (EEG) sensors[25-27], image-based flow cytometry[28, 29], and autonomous vehicles[30]. In these fields, extracting meaningful information from complex image data heavily relies on image-based ML.

As a cross between microfluidics and ML, intelligent microfluidics hopes to retain the advantages of microfluidic devices in data collection, such as fast and small size, and replace the originally heavy data analysis work with ML[31]. In this combination, microfluidics facilitates the miniaturisation and automation of laboratory processes, generating substantial amounts of data, including images, to data collection devices, such as cameras. Meanwhile, the use of the ML model in this data enhances the ability to optimise experimental conditions, improve detection and classification methods, and even assist in the design of new microfluidic devices. This synergy increases efficiency and unlocks new possibilities in cross-discipline applications[32-34]. In fact, intelligent microfluidics has already made promising developments in biology, analytical chemistry and instrument manufacturing, demonstrating the potential of this combination[35]. However, research on intelligent microfluidic testing and monitoring

platforms that can simultaneously satisfy the criteria of decentralisation, affordability and rapidity is still in its early stages.

Take microalgae detection and monitoring in environmental research as an example, traditional methods for doing this involve labour-intensive sample collection and transportation, laboratory-based microscopy, and manual morphological analysis, which are extremely time-consuming and rely on specialised facilities[36]. These factors combine to directly contribute to the lack of widespread distributed monitoring, despite the high ecological and commercial value of monitoring and analysing microalgae[37-39].

Similarly, in biosensors for disease monitoring, detecting and quantifying biomarkers like cytokines is essential for assessing immune responses and guiding therapeutic interventions in various diseases[40, 41]. However, conventional detection methods, such as enzyme-linked immunosorbent assays (ELISA)[42] and polymerase chain reaction (PCR)[43], are limited by lengthy processing times and the need for sophisticated laboratory equipment. Although the application of POCT based on microfluidic technology has greatly reduced the time required for testing, the complex microfabrication process and the need for corresponding specialised instruments to read the results remain challenges for most of these POCTs[44].

1.2 Fundamental concepts

It is essential to first introduce several key concepts that form the foundation of this thesis, including microfluidics, machine learning, and immunoassays. These concepts are central to understanding the methodologies and innovations presented in the subsequent chapters. A clear

understanding of each will provide important context for how they are integrated and applied throughout this work.

1.2.1 Microfluidics

Microfluidics is an engineered systems that manipulate, processes and analyses small volumes of fluids, typically in the microlitre to picolitre range, within networks of microchannels sized in tens or hundreds of micrometres[45]. By doing so, microfluidic devices can integrate multiple laboratory operations onto a single chip, which could also be named as lab-on-a-chip technology. As the channel dimensions shrink in microfluidic devices, interfaces between liquids or between a liquid and gas significantly influence fluid behaviour[46]. For example, capillary effects, which enable self-driven flow, could be considered as a mechanism for sample loading in microfluidics devices without the need for external injecting devices[47-49].

Microfluidics can provide the following advantages for on-site bioparticle detection and monitoring: 1) Running assays with microfluidics devices decreases sample volumes needed, saving cost in reagent and minimising waste; 2) Microfluidic systems can incorporate filtering and detection sections in a compact setup; and 3) Although microfabrication, such as soft lithography, can be considered as a complex process, the production of microfluidic chips based on laser cutting and 3D printing provide effective and simple methods of manufacturing microfluidic devices[50, 51].

1.2.2 Machine Learning

Machine learning is an area of artificial intelligence where the model learns from data based on certain learning methods, or in other words, algorithms, rather than following direct instructions. In many tasks, such as vision-based classification and detection, machine learning can surpass traditional direct-instructions-based methods by progressively refining itself using the large datasets[52]. Deep learning, as an example of machine learning, uses neural networks with multiple layers. This neural network-based machine learning can automatically extract meaningful features from raw images. In this case, developers are free from designing handcrafted algorithms.

Machine learning offers several benefits in on-site detection and monitoring system design: 1) It allows the rapid analysis of complex and heavy data, such as images and other signals from sensor outputs, directly on portable devices like microcomputers; 2) By continuously training on new datasets, the machine learning model can adapt to evolving conditions or novel sample types, increasing system robustness and extensibility; and 3) Edge computing developments now make it feasible to deploy machine learning models efficiently on resource-constrained hardware, such as Raspberry Pi and mobile phones, which makes real-time, on-site detection practical[53-55].

1.2.3 Immunoassays

Immunoassays use the high specificity and affinity between antibodies and antigens to detect the presence of target analytes. Antibodies conjugated to a detection probe, such as fluorescent tags, bind to the paired antigen, resulting in a measurable signal[56]. Common immunoassay

formats include enzyme-linked immunosorbent assays and lateral flow assays. In addition, agglutination assay, where microparticles such as latex beads or red blood cells are coated with antibodies, is also a method that can visually detect antigen presence by observing microparticles' cluster formation[57]. The performance of immunoassays is mainly measured by: 1) Specificity and sensitivity; 2) Assay time and simplicity; and 3) Detection limits. When coupled with machine learning, immunoassays gain an additional layer of versatility[58, 59]. Machine learning models can accurately interpret complex optical or electrochemical signals, even in resource-limited contexts. This additional functionality enables real-time detection of results with minimal user intervention.

1.3 Motivation and Objectives

The motivation for this thesis stems from the increasing need to overcome the limitations of traditional detection and monitoring pathways, which are often centralised, expensive and time-consuming. The COVID-19 pandemic has highlighted the inadequacy of existing detection methods of meeting the need for rapid, decentralised, and affordable diagnosis on a large scale. In addition, global climate change, such as extreme weather events and water pollution also called for on-site distributed portable environmental monitoring methods. While the microfluidics technology demonstrates the potential to reduce the time cost of testing and offers a certain degree of portability, it struggles to fully meet these needs due to the necessity of a complex microfabrication process, the need for supporting analytical equipment, and the presence of trained personnel. Additionally, with the development of hardware, trained ML

models have exploded their potential for real-time analysis when combined with microfluidic devices to become intelligent microfluidics, as they can be directly deployed to portable terminals to replace manual analysis.

To this end, this thesis aims to develop and enhance intelligent microfluidic platforms by integrating vision-based ML for improved on-site detection and monitoring capabilities. The specific objectives are:

(a) Investigate and identify knowledge and application gaps in intelligent microfluidics by reviewing recent advancements and applications (since 2017) in this field. Review how machine learning has been applied to biological microfluidics, chemical microfluidics, and microfluidic device fabrication, and what machine learning algorithms have been applied.

(b) Develop a compact (fits into 10 litre backpack) and low-cost (total cost of fabrication less than £200, which is about the price of commercial Raspberry Pi microscope kit) automated intelligent microfluidic platform equipped with automated positioning (XYZ motorised stage) and a portable digital imaging system capable of data acquisition for on-site detection and monitoring.

(c) Integrate machine learning models on source-constrained hardware (such as Raspberry Pi and mobile phone) to enable bright-field objective classification and detection in real time (response in less than 100 ms).

(d) Validate the feasibility of the automated and intelligent platform in environmental applications by microalgae detection and monitoring to quantify and track physiological

changes, capable of detecting more than 3 different species of microalgae with varying sizes and morphologies, with overall detection accuracy >90%.

(e) Adapt a similar intelligent microfluidic platform for developing a microbead-based immunoassay module that leverages visible pattern formation under magnetic fields, which is detectable by a machine learning model using a similar training pathway for rapid (less than 10 mins, competitive with lateral flow assay) biomarker detection.

1.4 Structure of the Thesis

This thesis is structured to offer an exploration of portable, decentralised bioparticle detection and monitoring using vision-based intelligent microfluidic platforms. It begins with an overview of the research background, establishing the context and motivation for the work. This is followed by detailed descriptions of the technologies developed and their applications, providing insight into how these innovative systems address current challenges in the field.

Chapter 1: General Introduction

This chapter provides an overview of the thesis's background, research context, and objectives. It introduces the essential concepts and challenges addressed in the study, setting the foundation for the chapters that follow.

Chapter 2: Literature Review

This chapter presents a review in the form of a published paper titled "Exploiting Machine Learning for Bestowing Intelligence to Microfluidics." This review consolidates current knowledge in the field, identifies key gaps, and underscores the need for improved detection

methods, particularly portable intelligent microfluidic solutions applicable to decentralised diagnosis, which this thesis aims to address.

Chapter 3: An Automated and Intelligent Microfluidic Platform for Microalgae Detection and Monitoring

This chapter introduces the development of an Automated and Intelligent Microfluidic Platform (AIMP) designed to overcome the time-consuming and labour-intensive drawbacks of conventional methods for microalgae detection and monitoring, as detailed in a published research paper. By integrating trained machine learning algorithms with a automated image capture and analysis system, the success of building this platform verifies the feasibility of using intelligent microfluidics for the straightforward detection and monitoring of microalgae. This work sets the stage for developing vision-based POCT devices for biomarker detection and analysis.

Chapter 4: Biomarker Conjugation Enabled Microbead Patterns for Intelligent Point-of-Care Biosensing

Leveraging the automated image capture and analysis platform developed in Chapter 4 for raw data collection, this chapter, structured as a manuscript for submission, presents the development of an image-based, Artificial Intelligence-Driven Point-of-Care Testing (AID-POCT) platform for cytokine detection, addressing the limitations of conventional methods that are time-consuming and require sophisticated laboratory equipment. By utilising magnetic microbeads coated with polyclonal antibodies to rapidly capture target cytokines and exploiting

the formation of concentration-dependent patterns under a magnetic field, the AID-POCT simplify the detection process and significantly reduces detection time to just a few minutes. Aiding by an ML model deployed on a mobile phone APP, this setup demonstrates a rapid and accurate solution for image-based interferon-gamma (IFN-γ) concentration level prediction. This innovative approach not only offers new potential for the development of biomarker assays but also contributes to advancing vision-based POCT devices for decentralised diagnosis and treatment monitoring.

Chapter 5: Conclusion and Future Work

The final chapter concludes the thesis by summarising the key findings of our research on developing portable, decentralised bioparticle detection and monitoring systems utilising vision-based intelligent microfluidic platforms. It discusses the implications of these findings for the fields of microfluidics and biomarker detection, emphasising how the integration of image-based ML with microfluidic technology can address current challenges in decentralised diagnostics. The chapter also suggests directions for future research, exploring opportunities to enhance the capabilities and applications of intelligent microfluidic platforms. By tying together the outcomes of the preceding chapters, this final chapter provides a coherent synthesis of the work presented in the thesis, highlighting its contributions to advancing the field.

1.5 References

[1] H. Gest, "The discovery of microorganisms by Robert Hooke and Antoni Van Leeuwenhoek, fellows of the Royal Society," *Notes and records of the Royal Society of London,* vol. 58, no. 2, pp. 187-201, 2004.

[2] M. Nicola *et al.*, "The socio-economic implications of the coronavirus pandemic (COVID-19): A review," *International journal of surgery,* vol. 78, pp. 185-193, 2020.

[3] R. W. Peeling, P. L. Olliaro, D. I. Boeras, and N. Fongwen, "Scaling up COVID-19 rapid antigen tests: promises and challenges," *The Lancet infectious diseases,* vol. 21, no. 9, pp. e290-e295, 2021.

[4] E. Valera *et al.*, "COVID-19 point-of-care diagnostics: present and future," *ACS nano,* vol. 15, no. 5, pp. 7899-7906, 2021.

[5] T. Stocker, G.-K. Plattner, and Q. Dahe, "IPCC climate change 2013: the physical science basis-findings and lessons learned," in *EGU general assembly conference abstracts*, 2014, p. 17003.

[6] P. G. Whitehead, R. L. Wilby, R. W. Battarbee, M. Kernan, and A. J. Wade, "A review of the potential impacts of climate change on surface water quality," *Hydrological sciences journal,* vol. 54, no. 1, pp. 101-123, 2009.

[7] M. L. Wells *et al.*, "Harmful algal blooms and climate change: Learning from the past and present to forecast the future," *Harmful algae,* vol. 49, pp. 68-93, 2015.

[8] R. Barry and D. Ivanov, "Microfluidics in biotechnology," *Journal of nanobiotechnology,* vol. 2, pp. 1-5, 2004.

[9] O. Scheler, W. Postek, and P. Garstecki, "Recent developments of microfluidics as a tool for biotechnology and microbiology," *Current opinion in biotechnology,* vol. 55, pp. 60-67, 2019.

[10] A. F. Oliveira, A. C. Pessoa, R. G. Bastos, and L. G. de la Torre, "Microfluidic tools toward industrial biotechnology," *Biotechnology progress,* vol. 32, no. 6, pp. 1372-1389, 2016.

[11] E. K. Sackmann, A. L. Fulton, and D. J. Beebe, "The present and future role of microfluidics in biomedical research," *Nature,* vol. 507, no. 7491, pp. 181-189, 2014.

[12] Q. Zhong, H. Ding, B. Gao, Z. He, and Z. Gu, "Advances of microfluidics in biomedical engineering," *Advanced materials technologies,* vol. 4, no. 6, p. 1800663, 2019.

[13] Y. Yang, Y. Chen, H. Tang, N. Zong, and X. Jiang, "Microfluidics for biomedical analysis," *Small methods,* vol. 4, no. 4, p. 1900451, 2020.

[14] T. Wang, C. Yu, and X. Xie, "Microfluidics for environmental applications," *Microfluidics in Biotechnology,* pp. 267-290, 2020.

[15] J. C. Jokerst, J. M. Emory, and C. S. Henry, "Advances in microfluidics for environmental analysis," *Analyst,* vol. 137, no. 1, pp. 24-34, 2012.

[16] M. Yew, Y. Ren, K. S. Koh, C. Sun, and C. Snape, "A review of state-of-the-art microfluidic technologies for environmental applications: Detection and remediation," *Global Challenges,* vol. 3, no. 1, p. 1800060, 2019.

[17] G. M. Whitesides, "The origins and the future of microfluidics," *nature,* vol. 442, no. 7101, pp. 368-373, 2006.

[18] S.-M. Yang, S. Lv, W. Zhang, and Y. Cui, "Microfluidic point-of-care (POC) devices in early diagnosis: A review of opportunities and challenges," *Sensors,* vol. 22, no. 4, p. 1620, 2022.

[19] G. Liu, C. Jiang, X. Lin, and Y. Yang, "Point-of-care detection of cytokines in cytokine storm management and beyond: Significance and challenges," *View*, vol. 2, no. 4, p. 20210003, 2021.

[20] M. Haenlein and A. Kaplan, "A brief history of artificial intelligence: On the past, present, and future of artificial intelligence," *California management review*, vol. 61, no. 4, pp. 5-14, 2019.

[21] M. L. Smith, L. N. Smith, and M. F. Hansen, "The quiet revolution in machine vision-a state-of-the-art survey paper, including historical review, perspectives, and future directions," *Computers in Industry*, vol. 130, p. 103472, 2021.

[22] M. Swapna, Y. K. Sharma, and B. Prasadh, "CNN Architectures: Alex Net, Le Net, VGG, Google Net, Res Net," *Int. J. Recent Technol. Eng*, vol. 8, no. 6, pp. 953-960, 2020.

[23] W. Xu, Y.-L. Fu, and D. Zhu, "ResNet and its application to medical image processing: Research progress and challenges," *Computer Methods and Programs in Biomedicine*, vol. 240, p. 107660, 2023.

[24] K. El Bouchefry and R. S. de Souza, "Learning in big data: Introduction to machine learning," in *Knowledge discovery in big data from astronomy and earth observation*: Elsevier, 2020, pp. 225-249.

[25] A. Craik, Y. He, and J. L. Contreras-Vidal, "Deep learning for electroencephalogram (EEG) classification tasks: a review," *Journal of neural engineering*, vol. 16, no. 3, p. 031001, 2019.

[26] A. Al-Saegh, S. A. Dawwd, and J. M. Abdul-Jabbar, "Deep learning for motor imagery EEG-based classification: A review," *Biomedical Signal Processing and Control*, vol. 63, p. 102172, 2021.

[27] H. Altaheri *et al.*, "Deep learning techniques for classification of electroencephalogram (EEG) motor imagery (MI) signals: A review," *Neural Computing and Applications,* vol. 35, no. 20, pp. 14681-14722, 2023.

[28] S. Luo *et al.*, "Machine-learning-assisted intelligent imaging flow cytometry: A review," *Advanced Intelligent Systems,* vol. 3, no. 11, p. 2100073, 2021.

[29] A. Gupta *et al.*, "Deep learning in image cytometry: a review," *Cytometry Part A,* vol. 95, no. 4, pp. 366-380, 2019.

[30] D. Parekh *et al.*, "A review on autonomous vehicles: Progress, methods and challenges," *Electronics,* vol. 11, no. 14, p. 2162, 2022.

[31] E. A. Galan, H. Zhao, X. Wang, Q. Dai, W. T. Huck, and S. Ma, "Intelligent microfluidics: The convergence of machine learning and microfluidics in materials science and biomedicine," *Matter,* vol. 3, no. 6, pp. 1893-1922, 2020.

[32] Y. Zhang, A. Zhou, S. Chen, G. Z. Lum, and X. Zhang, "A perspective on magnetic microfluidics: Towards an intelligent future," *Biomicrofluidics,* vol. 16, no. 1, 2022.

[33] H. Liu, L. Nan, F. Chen, Y. Zhao, and Y. Zhao, "Functions and applications of artificial intelligence in droplet microfluidics," *Lab on a Chip,* vol. 23, no. 11, pp. 2497-2513, 2023.

[34] X. Ma *et al.*, "Advances in integration, wearable applications, and artificial intelligence of biomedical microfluidics systems," *Micromachines,* vol. 14, no. 5, p. 972, 2023.

[35] J. Zheng, T. Cole, Y. Zhang, J. Kim, and S.-Y. Tang, "Exploiting machine learning for bestowing intelligence to microfluidics," *Biosensors and Bioelectronics,* vol. 194, p. 113666, 2021.

[36] F. Liu, C. Zhang, Y. Wang, and G. Chen, "A review of the current and emerging detection methods of marine harmful microalgae," *Science of the Total Environment*, vol. 815, p. 152913, 2022.

[37] S. Santhosh, R. Dhandapani, and N. Hemalatha, "Bioactive compounds from Microalgae and its different applications-a review," *Adv Appl Sci Res*, vol. 7, no. 4, pp. 153-158, 2016.

[38] N. Wu, X. Dong, Y. Liu, C. Wang, A. Baattrup-Pedersen, and T. Riis, "Using river microalgae as indicators for freshwater biomonitoring: Review of published research and future directions," *Ecological Indicators*, vol. 81, pp. 124-131, 2017.

[39] D. A. Lemley, J. B. Adams, and G. C. Bate, "A review of microalgae as indicators in South African estuaries," *South African Journal of Botany*, vol. 107, pp. 12-20, 2016.

[40] S. Kany, J. T. Vollrath, and B. Relja, "Cytokines in inflammatory disease," *International journal of molecular sciences*, vol. 20, no. 23, p. 6008, 2019.

[41] Z. Dembic, *The cytokines of the immune system: the role of cytokines in disease related to immune response*. Academic Press, 2015.

[42] P. Hornbeck, "Enzyme-linked immunosorbent assays," *Current protocols in immunology*, vol. 1, no. 1, pp. 2.1. 1-2.1. 22, 1992.

[43] G. Schochetman, C.-Y. Ou, and W. K. Jones, "Polymerase chain reaction," *The Journal of infectious diseases*, vol. 158, no. 6, pp. 1154-1157, 1988.

[44] C. M. Pandey *et al.*, "Microfluidics based point-of-care diagnostics," *Biotechnology journal*, vol. 13, no. 1, p. 1700047, 2018.

[45] G. M. Whitesides, "The origins and the future of microfluidics," *Nature*, vol. 442, no. 7101, pp. 368-373, 2006.

[46] J. Atencia and D. J. Beebe, "Controlled microfluidic interfaces," *Nature,* vol. 437, no. 7059, pp. 648-655, 2005.

[47] Y. Yu, L. Shang, J. Guo, J. Wang, and Y. Zhao, "Design of capillary microfluidics for spinning cell-laden microfibers," *Nature Protocols,* vol. 13, no. 11, pp. 2557-2579, 2018.

[48] M. Yafia *et al.*, "Microfluidic chain reaction of structurally programmed capillary flow events," *Nature,* vol. 605, no. 7910, pp. 464-469, 2022.

[49] A. Olanrewaju, M. Beaugrand, M. Yafia, and D. Juncker, "Capillary microfluidics in microchannels: from microfluidic networks to capillaric circuits," *Lab on a Chip,* vol. 18, no. 16, pp. 2323-2347, 2018.

[50] D. I. Walsh, D. S. Kong, S. K. Murthy, and P. A. Carr, "Enabling microfluidics: from clean rooms to makerspaces," *Trends in biotechnology,* vol. 35, no. 5, pp. 383-392, 2017.

[51] H. K. Balakrishnan *et al.*, "3D printing: an alternative microfabrication approach with unprecedented opportunities in design," *Analytical Chemistry,* vol. 93, no. 1, pp. 350-366, 2020.

[52] Y. LeCun, Y. Bengio, and G. Hinton, "Deep learning," *Nature,* vol. 521, no. 7553, pp. 436-444, 2015.

[53] M. S. Murshed, C. Murphy, D. Hou, N. Khan, G. Ananthanarayanan, and F. Hussain, "Machine learning at the network edge: A survey," *ACM Computing Surveys (CSUR),* vol. 54, no. 8, pp. 1-37, 2021.

[54] M. Merenda, C. Porcaro, and D. Iero, "Edge machine learning for ai-enabled iot devices: A review," *Sensors,* vol. 20, no. 9, p. 2533, 2020.

[55] G. Plastiras, M. Terzi, C. Kyrkou, and T. Theocharides, "Edge intelligence: Challenges and opportunities of near-sensor machine learning applications," in *2018 ieee 29th international conference on application-specific systems, architectures and processors (asap)*, 2018: IEEE, pp. 1-7.

[56] P. Hornbeck, "Enzyme-linked immunosorbent assays," *Current protocols in immunology,* vol. 1, no. 1, pp. 2.1. 1-2.1. 22, 1992.

[57] M. M. Galton, C. R. Sulzer, C. S. Rosa, and M. J. Fields, "Application of a microtechnique to the agglutination test for leptospiral antibodies," *Applied microbiology,* vol. 13, no. 1, pp. 81-85, 1965.

[58] G.-R. Han *et al.,* "Machine learning in point-of-care testing: innovations, challenges, and opportunities," *Nature Communications,* vol. 16, no. 1, p. 3165, 2025.

[59] Y. Song *et al.,* "Machine learning-based cytokine microarray digital immunoassay analysis," *Biosensors and Bioelectronics,* vol. 180, p. 113088, 2021.

2 CHAPTER 2: LITERATURE REVIEW

Exploiting Machine Learning for Bestowing Intelligence to Microfluidics

Results of this chapter are published in: **J. Zheng**, T. Cole, Y. Zhang, J. Kim and S.-Y. Tang (2021). "Exploiting machine learning for bestowing intelligence to microfluidics" Biosensors and Bioelectronics **194**: 113666.

Author Contributions: **J. Z.** and S.-Y. T. proposed the review idea. **J. Z.** conducted research on the idea, structured, and completed the first draft of the manuscript. S.-Y. T. supervised the student. All authors participated in participated in reviewing the manuscript.

2.1 Introduction

Intelligent microfluidics is an emerging field formed by the fusion of microfluidics and machine learning (ML). Microfluidics is a technique for processing or manipulating small amounts of fluid using channels less than a few hundred microns in size[1]. In fact, Microfluidic chips are now capable of providing capabilities comparable to a laboratory on a small scale[2, 3]. Microfluidics has been used in many different disciplines, such as cellular manipulation and analysis[4-6], Bio-macromolecules (DNA, RNA, proteins) analysis[7-11], material science[12, 13], environmental analysis[14, 15] and chemistry[16, 17]. However, in the intersection with

these fields, microfluidics is used more as a tool to reduce the experiment to a smaller scale and to generate data for analysis. Meanwhile, ML, a powerful data analysis method that can learn from the dataset without directly programming changes, has proven its abilities in many applications such as natural language processing[18], games[19], and finance[20] amongst others. As a discipline supported by the convergence of two technologies, intelligent microfluidics utilises the power of ML to unlock the vast potential of microfluidic systems. Before presenting the latest developments in intelligent microfluidics, we first give a brief overview of ML and microfluidics to explain how intelligent microfluidics came into being from a historical perspective.

ML is a branch of artificial intelligence (AI), first proposed as a research area by American computer scientist John McCarthy at the Dartmouth Conference in 1956[21]. However, enthusiasm for AI diminished and research was limited because computers at the time were incapable of storing enough information or processing it fast enough, which resulted in the first winter period of AI[21]. In the 1980s, the first AI winter was brought to its end by the concept of expert systems[22]. Data-driven ML, which improves at a task by learning from experience, was also adopted as a major direction for AI. At the turn of the 21st century, the computing power of computers improved, resulting in an increased ability of ML systems and a resurgence in research. The amount of available data also increased significantly, and the concept of deep learning was introduced. Deep learning, proposed in the 2010s[23], is a subset of ML which uses deep neural networks (DNNs). It has gained tremendous attention in a wide range of applications due to its superior learning capabilities (Figure 2.1).

Microfluidics has four parent fields that inspired its birth. These are molecular analysis, biodefense, molecular biology, and microelectronics[2]. The first lab-on-a-chip system (which can also be treated as the first microfluidics application) was made from silicon wafers by

photolithography and chemical etching in 1979[24]. In the 1990s, microfluidics saw rapid development due to the introduction of soft lithography technology and silicone elastomers such as polydimethylsiloxane (PDMS). This was during the second winter of AI, when ML was in desperate need of new applications in order to prove its potential. Intelligent microfluidics was therefore started in that era (Figure 2.1). At the beginning of the 21st century, when ML started to be widely used in various fields, a new and important element of microfluidics was developed – droplet-based microfluidic[25, 26]. The main advantage of droplet-based microfluidics is its high multiplexing capability, which means that it has the ability to allow thousands of reactions to react independently at the same time[27]. This also results in the need for a very high data processing ability. Therefore, intelligent microfluidics, which had been dormant for nearly 20 years, began to receive an increased amount of attention from researchers.

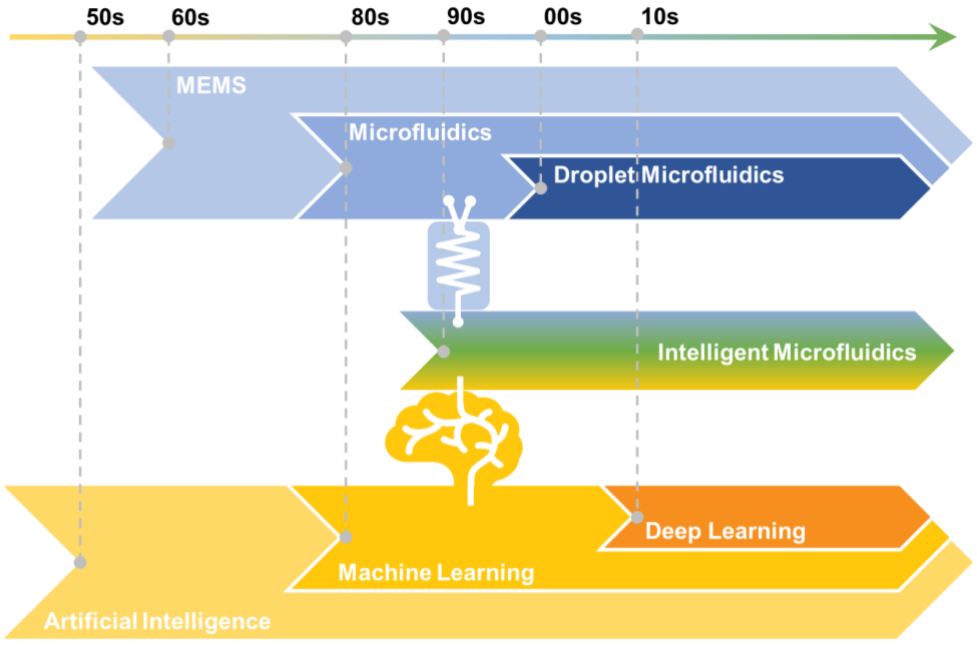

Figure 2.1 Timeline of the development of intelligent microfluidics.

50s− The birth of artificial intelligence (AI). 60s − The birth of microelectromechanical systems (MEMS). 80s − The development of expert systems established the dominance of data-driven

machine learning (ML) in its parent set, AI; meanwhile, the first lab-on-a-chip system signified the beginning of microfluidic research. 90s − The birth of interdisciplinary intelligent microfluidics. 00s − The introduction of droplet-based microfluidics with better parallelism. 10s − Deep learning, a subset of ML, has the ability to learn more complex tasks as big data started to be widely used.

Traditional statistic-based data analysis relies heavily upon human intervention. In contrast, ML involves the dynamic improvement of computer-aided prediction performance from large amounts of data with minimum human intervention. ML is a useful tool for feature extraction, classification, prediction, and optimisation using the massive amounts of data generated by microfluidic systems. Intelligent microfluidics has shown its ability to solve difficult or even unsolvable problems with traditional data analysis, such as finding optimised conditions for complex chemical reactions[28], label-free bio-detection followed by classification[29], and the reverse design of microfluidic devices[30]. In addition, the introduction of ML has greatly reduced the human workload that would have been required by using traditional data analysis when it comes to big data.

We collected applications that combine ML and microfluidic technologies since 2017 and classified them into categories (Figure 2.2). Biotechnology has accounted for more than half of the applications for intelligent microfluidics since 2017. Among the biotechnology applications of intelligent microfluidics, cell classification (including cell screening, cytopathologic analysis, and cellular chemical analysis) is the most popular development direction. Other applications, such as cell sorting and cell counting, are derived from cell classification. Intelligent microfluidics is also used in chemistry to optimise experiments or conduct assays, although its application in this field is less popular than in biotechnology. In contrast, the use of ML to upgrade microfluidic devices themselves accounts for a larger share (nearly one-third of all

applications) than the use of intelligent microfluidics in chemistry. One of the main application directions is using ML to analyse, design, and control continuous or discrete fluids in microchannels.

There are examples of using both deep learning and classical ML approaches in all three categories of applications. Here, we define deep learning as an ML method that contains multiple processing layers in the networks for explaining and extracting data with complex structures[31]. On the other hand, classical ML is referred to as all other algorithms not using DNN models, such as support vector machines (SVM), linear regression, logistic regression (LR), and decision trees. The ensemble of all deep learning and classical ML models is referred to as ML.

There are now established processes or supporting tools for both the fabrication of microfluidic devices and the construction and training of ML models. The manufacturing of microfluidic devices has been summarised in a number of previous review articles[32-35]. In a review paper written by Shrestha *et al.*, the algorithms and architectures related to deep learning are explained[36]. There are also many sophisticated tools to assist researchers in building ML models, such as the widely used TensorFlow[37], Caffe[38], and PyTorch[39]. Thanks to these "black box" technologies, which allow users from different backgrounds not to have to fully understand the detailed principles of operation, intelligent microfluidics is much easier to implement in device manufacturing and ML model building.

There are a few previous reviews on intelligent microfluidics[40-45]. Most of them mainly focus on the use of ML in biosensors and diagnostics; therefore, a review covering different aspects of microfluidic applications enabled by ML is necessary for facilitating the adoption of intelligent microfluidics by wider society. This review seeks to summarise recent exciting advances in intelligent microfluidics for enabling various applications. We will outline the key

technologies, recent advances, challenges, and emerging opportunities of intelligent microfluidics.

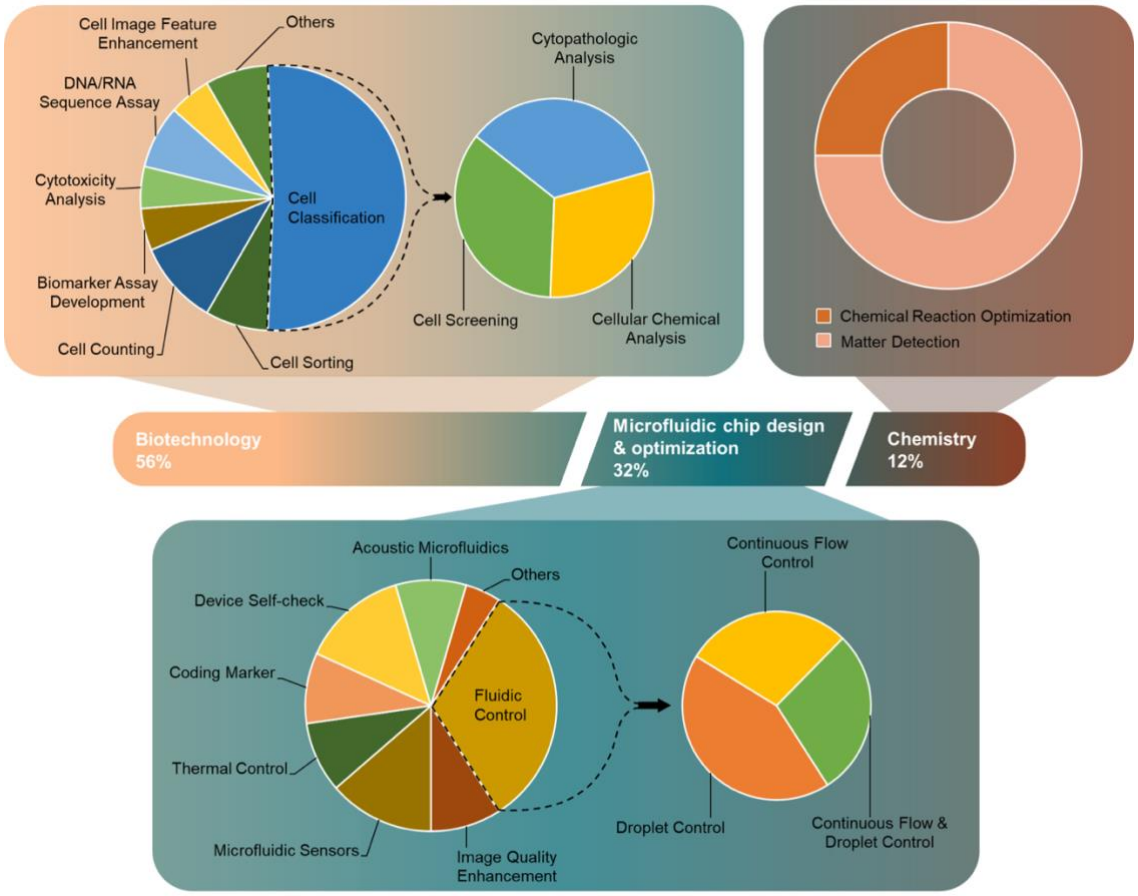

Figure 2.2 Summary of recent advances in intelligent microfluidics.

By indexing the keywords “machine learning”, “deep learning”, and “microfluidics” and searching the related articles, we collected applications of intelligent microfluidics since 2017. About 56% of works in intelligent microfluidics are related to biotechnology, 32% of works are about using ML for the development of chip design & optimisation, and 12% of applications are in chemistry. These three broad categories and their percentages are shown by three pie charts. Each direction category is further classified in detail and represented by pie charts with their corresponding proportions.

2.2 Intelligent Microfluidics in Biotechnology

The inherent advantages of intelligent microfluidics are particularly apparent when analysing and processing biological samples. Application areas of microfluidics in biotechnology include cell classification, cell counting, cell sorting, biomarker assay development, cytotoxicity analysis, cell feature enhancement, immunoassay, particle trajectory prediction, and bio-interface, as summarised in Table 2.1.

Research combining ML with microfluidic devices for biological applications (e.g., cell classification, cytotoxicity assays, biomarker detection) has shown remarkable progress. For instance, Guo *et al.*[46] and Jiang *et al.*[48] demonstrate label-free, high-throughput cell screening using optofluidic time-stretch microscopy combined with SVM or logistic regression, achieving >95% specificity and sensitivity for platelets or microalgae. However, while these advanced platforms boast impressive throughput (for example, 10,000 cells/s in [48]), the capital expense of high-speed optical imaging systems questions scalability for everyday labs and on-site detection. Meanwhile, efforts at imaging flow cytometry (Heo *et al.*[47] and Zhou *et al.*[51]) achieve similarly strong performance but again rely on stable flow focusing and powerful computing for real-time detection. Multiple works that use CNN-based deep learning, like McCallum *et al.*[50], Kobayashi *et al.*[64], and Ghafari *et al.*[52], report results on tightly controlled, single-species datasets, leading to concerns over generalisability to more complex or unbalanced scenarios (e.g., multi-strain or patient-derived samples).

A further challenge arises in cell sorting and counting applications. While iIACS (intelligent Image-Activated Cell Sorting) reported by Nitta *et al.*[66] and Isozaki *et al.*[68] achieves notable speed (thousands of events/s) via sophisticated acoustic focusing, the integration of microfluidic control, machine vision, and real-time computing remains cost-intensive and technologically intricate. Similarly, “classical” ML algorithms, such as SVM for T-cell/B-cell

identification[69,70], handle only bi-class problems. Although these studies deliver >90% accuracy, limited class scope and fluorescence-based approaches may restrict clinical or field translations. Approaches like autoencoder-based single-cell analysis[49,75] or immunoassay-enabled biomarker assays[73,81] can reduce certain reagent or labour costs, yet often lack robust comparisons against well-established laboratory workflows. Moreover, random forest or decision tree classifiers sometimes appear in biomarker quantification tasks[74,76] without standardised performance metrics, making cross-lab reproducibility unclear. Lastly, cytotoxicity and viability tests employing deep CNNs[80] or impedance-based identification[63] underscore the promise of ML-aided microfluidics for drug screening, but they frequently omit real-world factors like sample complexity, limited reagent stability, or cost breakdowns.

In summary, while current works[46–83] illustrate that machine learning can boost the automation, speed, and sensitivity of microfluidic assays in biotechnology, they also reveal common weaknesses: 1) Lack of cost reporting where reliance on high-end imaging or focusing hardware raises cost barriers; and 2) Narrowly scoped datasets often lacking morphological diversity. Consequently, although these successes lay the foundational work for future intelligent microfluidic systems, they highlight the need for cost-effective setups with cost reporting and diverse data across multiple experimental conditions and species.

Table 2.1 Summary of applications of intelligent microfluidics in biotechnology.

Category	Application	ML algorithm	Experimental setup	Comments	Reference
Cell classification (cell screening)	High-throughput label-free single cell screening of lipid-accumulated *E. gracilis* cells by optofluidic time stretch quantitative phase microscopy	SVM	Microfluidics: optofluidic time-stretch quantitative phase microscopy. Machine learning: N/A	–	[46]
	High-throughput label-free real-time moving object detector-based cell classification using imaging flow cytometry	Convolutional neural network (CNN)	Microfluidics: continuous flow microfluidic chip Machine learning: off-line classifiers training using *MatConvNet*. Caffe is used to accelerate computing by providing a graphics processing unit (GPU, NVIDIA GTX 1080) computation	–	[47]

	High-throughput label-free single blood cell morphology-based classification using optofluidic time stretch microfluidic chip	Logistic regression (LR)-based linear classifier	Microfluidics: optofluidic time-stretch microscopy embedded hydrodynamic-focusing microfluidic chip Machine learning: MATLAB and Cell Profiler	–	[48]
	Microfluidics-based single-cell classification (heterogeneous mixtures of yeast species)	Variational autoencoder (VAE)	Microfluidics: Y-shape flow focusing microfluidic channels Machine learning: *PyTorch* with *torchsupport* library	–	[49]
	Label-free prediction and of DNA quality and classification of sperm cells in bright field images only	CNN	Microfluidics: continuous flow image-based microfluidic cytometry	–	[50]

		Machine learning: *Keras* with *TensorFlow* backbone on a PC with NVIDIA GeForce GTX1060 GPU		
Classification of platelets and platelet aggregates labelled by anti-CD61-APC and anti-CD45-FITC antibodies	CNN	Microfluidics: continuous flow microfluidic chip Machine learning: *Keras* with *TensorFlow* backbone	–	[51]
Microfluidics-based analysis of replicative senescence in budding yeast cells	CNN, Capsule Network	Microfluidics: continuous flow microfluidic channels Machine learning: NVIDIA Tesla P100 GPU	The accuracy, precision and recall of the CNN are found to be superior to that of a capsule network with strong performance in detecting a specific class of cell images	[52]

Cell classification (cytopathologic analysis)	High-throughput label-free classification of *leukemia* cell lines using microfluidic imaging flow cytometry	Deep believe network (DBN)	Microfluidics: microfluidic imaging flow cytometry Machine learning: MATLAB on a PC	Picture-based cell classification with limited labelling using DBN	[53]
	High-throughput label-free tumour cells in blood classification using inline digital holographic microscope	Decision tree	Microfluidics: continuous flow microfluidic channels Machine learning: MATLAB on Windows PC	–	[54]
	Pancreatic cancer cells identification using the exosome track-etched magnetic nanopore chip	Linear discriminant analysis (LDA)	Microfluidics: exosome track-etched magnetic nanopore membranes fabricated by thermally evaporating Machine learning: MATLAB on a PC	MATLAB 2015b′ s built-in LDA function is used for classification and cross validation	[55]
	Detection and classification of cancer-associated fibroblasts	LR-based linear classifier	Microfluidics: continuous flow microfluidic chip	–	[56]

and two types of non-small cell lung cancer cells, A549 and H322, using microfluidic polarimetric imaging and analysis		Machine learning: N/A		
Flexible inkjet-nanoparticle-printed-impedance micro-cytometry biochip for differentiation and classification of different types of label-free cancer cells	Quadratic discriminant analysis	Microfluidics: a continuous flow microfluidic chip Machine learning: MATLAB on a PC	–	[57]
Stain-free primary and metastatic colon cancer cells and 4 types of blood cells (granulocytes, lymphocytes, monocytes and erythrocytes) classification	Principal component analysis (PCA), SVM	Microfluidics: continuous flow microfluidic chip Machine learning: MATLAB on a standard central processing unit (CPU)	The unsupervised PCA is used to extract the main features of the cells, and then the supervised SVM classifier is trained based on the labeled data	[58]

				according to the extracted features	
	Image segmentation and classification of sickle red blood cells (sRBC) using deep learning and microfluidics	U-net-like CNN, ResNet-50	Microfluidics: biochips fabricated using PMMA sheets, custom laser-cut double-sided adhesive films, and ultra stick adhesion glass slides Machine learning: *Keras* with *TensorFlow* backbone on a PC	The unsupervised U-net-like CNN is used to locate cells and segment the input image, and then using transfer learning, the segmented images with their labels are feed to fine-turn the ResNet-50 for cell classification	[59]
	Classification of different types of rare hereditary *hemolytic anemia* (RHHA) using microfluidics-simulated spleen and machine learning.	AlexNet, SVM	Microfluidics: The device consists of 8 parallel microchannels containing micro-constrictions in the shape of filter funnels to simulate the internal endothelial slits (IES) of the spleen.	An initial unsupervised automatic feature filtering of the acquired images is performed using AlexNet and important features are extracted. An SVM	[60]

			Machine Learning: N/A	classification model with a linear kernel is then constructed based on the selected features.	
Cell classification (cellular chemical analysis)	High throughput, label-free bright-field-imaging classification of drug treated and untreated cells using optofluidic time-stretch microscopy	SVM	Microfluidics: continuous flow microfluidic channels Machine learning: MATLAB and CellProfiler (version 2.2.0)	–	[29]
	Antimicrobial susceptibility of Escherichia coli cells to five different commonly used antibiotics (polymyxin B, streptomycin ciprofloxacin, aztreonam and ampicillin)	CNN	Microfluidics: microfluidic chips with six parallel detection channels fabricated by multilayer soft lithography Machine learning: TensorFlow on a PC with Intel Core i7-4790 CPU	–	[61]

	Microscopic image-based antibiotic susceptibility testing of bacteria in microfluidic culture device	CNN	Microfluidics: a straight-through channel device for liquid suspension culture and a multi-channel device for bacterial culture on agar gels flanked by liquid broth Machine learning: N/A	–	[62]
	Label-free drug sensitive and insensitive tumour cells classification	SVM	Microfluidics: continuous flow PDMS microfluidic channels Machine learning: N/A	–	[63]
	Image-based, label-free evaluation of drug sensitivity of white blood cells	Autoencoder	Microfluidics: continuous flow PDMS microfluidics channels Machine learning: image preprocessing using MATLAB on a PC and network built	–	[64]

			by *Keras* with *TensorFlow* backbone on a PC		
	Label-free tumour cells viability for large-scale drug bright-field screening	CNN	Microfluidics: PDMS microfluidic chip with 320 spherical culture chambers divided by gap rings supported by a micro-column structure Machine learning: MATLAB on a PC	–	[65]
Cell sorting	Real-time sorting of microalgae and blood cells based on intracellular protein localisation and cell-cell interactions using a combined hardware and software platform (iIACS)	CNN	Microfluidics: combined hydrodynamic and acoustic focusing, microfluidic channels with on-chip dual-membrane push-pull cell sorter Machine learning: a real-time intelligent image processor consisting of a field-programmable gate array	–	[66]

		(FPGA - Xilinx KC705), a multi-core CPU (Intel Core i7-990X), a multi-core CPU (Core i7-8700K), a GPU (NVIDIA GTX-1050Ti) and a network switch all located on a 10-Gbps all-IP network. *TensorFlow* is used to build the network		
Microfluidic droplet and image based single cell sorting (Red blood cells and K562 cells stained with Hoechst fluorescent dye)	SVM	Microfluidics: PDMS microfluidic channels were photolithographically patterned on the silicon wafer. Indium gallium arsenide (InGaAs) was introduced into the electrode channel Machine learning: MATLAB on a PC	–	[67]
An improved version of Intelligent Image Activated Cell Sorting (iIACS) offering	CNN	Microfluidics: combined hydrodynamic and acoustic focusing,	–	[68]

	high throughput of 2000 events per second and high sensitivity of 50 molecular equivalents of soluble fluorochromes (MESFs)	microfluidics channels with on-chip dual-membrane push-pull cell sorter Machine learning: camera control node with a multi-core CPU (Intel Core i7-7700K), a counter board (CONTEC CNT-3204MT-LPE), a 10-Gbps Ethernet port, and a pair of camera link ports (10 taps, 85 MHz). Image analysis cluster consists of two parts (Master: a multi-core Intel Core i7-8700K CPU, solid state drive storages, and a 10-Gbps Ethernet port. Slave: 8 multi-core Intel Core i7-8700K CPUs and 8 NVIDIA GeForce GTX 1080 Ti GPUs). Time management node with an FPGA board (Xilinx KC705)

Cell counting	Detection, classification and count of T-cells and B-cells stained with two colours (CD3-FITC/CD19-PE) of immunofluorescent dye using pillar-based microfluidic chips	SVM	Microfluidics: pillar-based microfluidics chips Machine learning: N/A	–	[69]
	Identification and enumeration of human T lymphocyte subclasses (CD4+ and CD8+ cells) by cell size, refractive index of the nucleus, refractive index of the cytosol and the ratio of nucleus to cytosol characteristics	SVM	Microfluidics: microfluidic channel patterns engraved on the underside of a PMMA sheet using a micro-milling machine Machine learning: MATLAB on a PC	–	[70]

	Microscopic image, microfluidics channel and deep learning-based fully automated white blood cell counting.	Faster Region-based CNN	Microfluidics: continuous flow microfluidic channels Machine learning: N/A	Fine-tuning the pre-trained model for the region proposal task to complete the training of the object detection model with a small dataset	[71]
	Cell counting by training a generative model on both natural and synthetic data, requiring small amount of labelled data	VAE-based generative model	Microfluidics: microfluidic single-cell cultivation (MSCC) PDMS-glass-chips Machine learning: *PyTorch* in Python on a PC	–	[72]
Biomarker assay development	Microfluidics-based high content biomarker assay with single cell resolution for the analysis of cell cultures from	Random forest (RF)	Microfluidics: a microfluidic device which can automatically load cells and exchange fluid with luer-lock inlet and outlet	A RF with a collection of trained decision trees is used to classify the labelled cells, averaging the results by random	[73]

solid prostate-tumour tissue or breast-tumour tissue		Machine learning: MATLAB on a PC	selection, thus ensuring sensitivity and specificity	
Improving a specific disease among diseases identification where changes in protein biomarkers (CA19-9, HE4, MUC4, MMP7 and mesothelin) overlap	Classification tree, K-nearest neighbour (K-NN), Decision tree	Microfluidics: PDMS microfluidic chips fabricated using 3D printed molds Machine learning: N/A	A classification tree classifier is used to provide information about biomarkers from Raman spectral peaks. The full spectrum is then analysed with a K-NN classifier to reduce the effect of noise and extract key biomarkers. A decision tree model is created to make prediction	[74]
Distinguish between cell-containing droplets and empty droplets when droplet-based	Autoencoder	Microfluidics: a droplet-based microfluidic chip	–	[75]

scRNA-seq assays generate large numbers of background RNA counts and retrieve background-free gene expression profiles		Machine learning: NVIDIA Tesla K80 GPU on a PC		
Label-free detection of amplified DNA in post-loop-mediated isothermal amplification (LAMP) sub-nanocrystalline droplets by identifying LAMP by-products that form fractal structures observable in bright-field microscopy	Bag of visual word model, RF	Microfluidics: a 3D microfluidic droplet generator Machine learning: N/A	Although this paper images static droplets, by combining with multi-channel high throughput imaging of droplets in a stream, it is possible to image droplets in continuous flow if the disturbing circular flow in the droplets can be reduced	[76]
Removal of debris-contaminated droplets from	K-means, semi-supervised	Microfluidics: a droplet-based microfluidic chip	K-means is used for initial grouping and to determine	[77]

	single-cell-based single-nucleus RNA sequencing (snRNA-seq) data	expectation maximum (EM)	Machine learning: R language programming on a PC	the initial parameters of the EM model. The parameters are then estimated using semi-supervised EM to calculate the probabilities of the latent group variables given the data to classify group debris and cell type droplets	
Cell feature enhancement	Enhancement of images acquired by lens-free cell imaging systems to better reflect cell morphology	Feature Fusion Network	Microfluidics: a continuous flow microfluidic chip Machine learning: N/A	An encoder is used to extract features and generate a feature map, and then a decoder is used to reconstruct the input image from the feature map	[78]

	Label-free particle characterisation of beads, red blood cells and yeast in microfluidic impedance cytometry in terms of size, velocity and cross-sectional position	Long short-term memory (LSTM)	Microfluidics: a microfluidic impedance glass chip with built-in Ti/ Au electrodes Machine learning: MATLAB on a PC with Intel Xeon CPU E5-2660 v3, 2.60 GHz processor, 128 GB RAM	–	[79]
Cytotoxicity analysis	Microfluidic droplet and deep learning-based cytotoxicity assay for quantitative comparison of immunotherapeutic NK (Natural Killer)-92 cell interactions with various types of fluorescent-labelled target cells	CNN	Microfluidics: a droplet-based microfluidic device Machine learning: Pytorch in python on a PC	–	[80]

Immunoassay	Digital powerful biomarker profiling immunoassay of 12 serum cytokines in human patients treated with chimeric antigen receptor-T (CAR-T) cells.	CNN	Microfluidics: microarrays with hexagonal microfluidic channels Machine learning: a PC with Intel Core i7-8700 CPU and NVIDIA Quadro P1000 GPU	–	[81]
Particle trajectories prediction	Optimisation of microfluidic devices for the analysis of blood samples by predicting the movement of red blood cells.	Self-organising map	Microfluidics: software (ESPREesSo) simulated microfluidic channels Machine learning: N/A	–	[82]
Bio-interface	Combination of ML techniques nanoelectronics and microfluidics to build and test low-power, adaptable bio-interfaces	Multilayer perceptron (MLP)	Microfluidics: a PDMS microfluidic chip which is designed based on a sequence of 3 or 4 triangular segments and consists of two chambers for cell culture and 8 microchannels to provide	–	[83]

	unidirectional axon growth from the source chamber to the target chamber
	Machine learning: FPGA-based control subsystem

2.2.1 Cell classification using intelligent microfluidics enabled by classical ML

Classical ML can be used for classifying large numbers of measurements into more useful and intuitive low-dimensional outputs. Cell classification using classical ML (*e.g.*, LR and SVM) can be helpful in reducing the repetitive work of researchers, and is able to classify cells with high speed and accuracy[48, 54, 67].

In 2017, Jiang *et al.* introduced a high-throughput, label-free single blood cell morphology-based classification method using an optofluidic time-stretch microfluidic chip (Figure 2.3A)[48]. They fabricated a hydrodynamically focused microfluidic channel with dimensions of 100 μm width, 40 μm height and 30 mm length. Combining optical time-stretch microscopy and a simple linear classifier based on a standard LR model, the method achieves a high throughput of 10,000 blood cells per second, giving morphological differentiation between aggregated platelets, single platelets, and white blood cells. With its ability to obtain blur-free images at ultra-high shutter speeds (7.4 ns) and one-dimensional frame rates of 75 MHz, the optofluidic time-stretch microscope provides trained machines with images, from which more than 100 morphological features can be extracted. Therefore, by implementing supervised ML, the platform realised image-based cell classification. It achieved a differentiation of aggregated platelets from single platelets and leukocytes with a high specificity of 96.6% and a high sensitivity of 96.6%. The results achieved in this work show that it is potentially promising for predictive diagnosis and therapeutic monitoring of thrombophilia in the clinical setting. Using similar equipment, Guo *et al.* described heterogeneous populations of *Ciliophora* cells under nitrogen-sufficient and nitrogen-deficient culture conditions[46]. This work achieved a high-throughput, label-free SVM-based cell classification with an error rate of 2.15%. Kobayashi *et*

al. also applied this set of intelligent microfluidic systems based on optofluidic time-stretching microscopy and SVM mechanics for the label-free detection of cellular drug responses[29].

The SVM mentioned above is a typical classical ML algorithm, which is used in many applications of intelligent microfluidics[29, 46, 58, 63, 67, 69, 70]. SVM attempts to achieve linear or nonlinear separation of data by finding the decision boundary that produces the maximum separation or margin between classes. Ahuja *et al.* used SVM and multi-frequency impendence cytometry to characterise and evaluate cells (Figure 2.3B)[63]. As the cells pass through the electrode pair, this results in a modulation of the ionic resistance. After detrending and denoising the raw data, the two significant features (amplitude change and phase change) are extracted as the processed data. For the SVM to produce the best hyperplane for the classification of the test data and thus improve the classification accuracy, they used an SVM with a Gaussian kernel. The overfitting problem, which commonly occurs when the dataset is unbalanced, was solved by creating an even and relatively large dataset with a size of more than 1000 events for both live cells and dead cells (features of live cells were marked as 1 and features of dead cells were marked as 0). The accuracy of the final classifier obtained for T47D cancer cells, target-drug-treated T47D cancer cells, and T47D dead cancer cells was 95.9%, with a true positive (TP) rate of 95% and a true negative (TN) rate of 97%.

Other classical ML systems combined with microfluidic cellular data acquisition include ones based on inline digital holographic microscopy (inline-DHM) with a decision tree model[54], polarisation microscopy imaging with LR[56], interferometric phase microscopy imaging with principal component analysis (PCA) and SVM[58] and a dual-imaging microscope system with SVM[67]. Instead of using optical systems, Joshi *et al.* utilised an impedance-based microfluidic device exploiting quadratic discriminant analysis to achieve the classification of cancer[57].

As well as classifying cells by their own characteristics, cells can also be classified by the detection of cellular products. Ko *et al.* developed an exosome track-etched magnetic nanopore (ExoTENPO) chip to isolate exosomes from healthy and diseased mice and clinical cohorts. The platform can profile the RNA cargo within exosomes and complete the classification of cancer-related states (precancerous, cancerous, and healthy) by linear discriminator ML algorithms utilising training data sets from a panel of RNA biomarkers[55]. ExoTENPO can be used to capture target exosomes (by immunomagnetic labelling of exosome protein surface markers) directly from untreated serum or plasma. Captured exosomes are then disassembled on the chip and their mRNA cargo is extracted and analysed by quantitative PCR (qPCR) and classified to determine the status of the testers.

Intelligent microfluidics using classical ML can also study cells of the immune system for cell classification. Turan *et al.* proposed an SVM supervised ML classifier based on a histogram of oriented gradients and colour distribution features to quickly and robustly distinguish T-cells and B-cells[69]. However, the need for fluorescent antibody staining may be a limit of this technique. Alternatively, Rossi *et al.* developed an intelligent microfluidic chip that identifies T-cells based only on their biophysical characteristics[70], which offers the possibility of stain-free recognition of immune cells by using SVM.

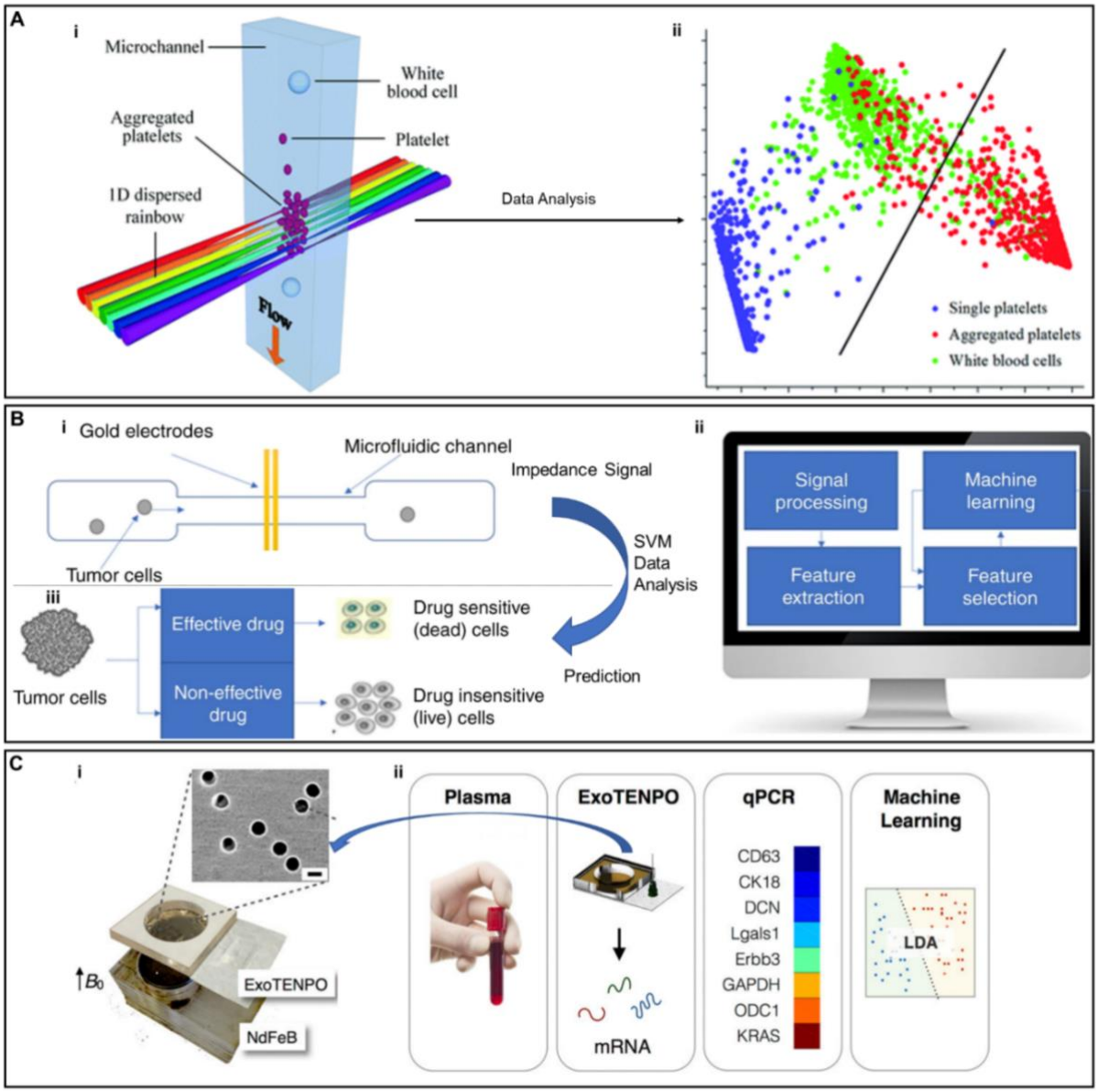

Figure 2.3 Classical ML-enabled cell classification in microfluidics.

(A) Detection of aggregated platelets in blood using SVM ML-assisted optofluidic time-stretch microscopy. i: Schematic diagram of the cells in the optical interrogation area of the microfluidic channel. ii: 2D scatter diagram obtained by projecting the initial 3D spatial scatter maps of single platelets, aggregated platelets, and white blood cells using SVM, which allows maximum separation between cell groups. Reproduced with permission[48]. Copyright 2017, Royal Society of Chemistry. (B) Schematic representation of the multi-frequency impedance

cytometry-embedded microfluidic device combined with ML for classifying live and dead cells. i: Schematic of the microfluidic channel. ii: SVM-based ML algorithm. iii: Classification of drug-treated cancer cells. Reproduced under the terms and conditions of CC-BY 4.0 license[63]. Copyright 2019, The Author(s). Copyright 2019, The Author(s). Published by Springer Nature. (C) Flow chart of pancreatic cancer diagnosis using ML-aided exosome track-etched magnetic nanopore (ExoTENPO) chip. i: Device diagram of the combination of ExoTENPO and neodymium external magnets and a scanning electron microscope (SEM) image of magnetic nanopores, scale bar is 600 nm. ii: Diagrams of the principle of the chip-based pancreatic cancer diagnosis, where qPCR stands for a quantitative polymerase chain reaction. Reproduced with permission[55]. Copyright 2017, American Chemical Society.

2.2.2 Cell classification using intelligent microfluidics enabled by deep learning

Deep learning models offer the opportunity to uncover cell features that are not easily detected by humans in cell classification, which is also relatively hard to achieve by using classical ML[60]. Deep learning architectures, such as DNNs are being used for an increasing number of biotechnology applications because it provides the advantage of being able to perform more accurate analysis and to process complex and large data sets, such as a raw image dataset.

For example, Ghafari *et al.* compared the performance of three ML methods with different network architectures (CNN-2 – a convolutional neural network with two convolutional layers, CNN-13 – a convolutional neural network with thirteen convolutional layers, and CapsNet − capsule network) in classifying images of yeast cells immobilised in microfluidic traps at different stages of replicative senescence (Figure 2.4A)[52]. The data set used to train the neural network was provided by a high-throughput yeast aging analysis (HYAA) chip containing approximately 104 traps. The first examined network has a two-layer architecture with two

convolutional layers (labelled as CNN-2) and represents one of the most simplified CNN models, which is also known as the baseline CNN architecture[84]. Using such a simple network, the final overall accuracy achievable is 90.2%. Compared with CNN-2, CNN-13 adds 11 convolutional layers, and the final model achieved an overall accuracy of 97%. Moreover, CapsNet is a novel architecture for deep learning that replaces the typical pooling layer of CNNs with a more complex weight routing mechanism, and its basic version has been shown to outperform extremely complex CNN architectures[85]. In this task, CapsNet achieved an overall accuracy of 90%, but it was more sensitive to data augmentation compared to the other two CNN models and performed well on recognising single mother cell classes (mC). Their experiments also show that newer and more complex networks do not necessarily perform better on all tasks and therefore, the choice of network needs to be determined by different needs. In a recent study reported by Rizzuto *et al.*, the authors used intelligent microfluidics to classify different types of rare hereditary *hemolytic anemia* (RHHA) (*hemoglobinopathies*, *membranopathies*, and *enzymopathies*)[60]. This work used a microfluidic device to simulate inter endothelial slits (IES) in the spleen to examine the ability of red blood cells to regain their original shape after passing through micro-contractions. The CNN-based AlexNet was used for feature extraction. The extracted features were finally classified using SVM, achieving an efficiency of 91% for discriminating RHHA patients from healthy persons and an efficiency of 82% for discriminating different types of RHHA.

Once a suitable network architecture has been selected for cell classification, if it is combined with a sorting system, it will become an integrated intelligent cell sorter. Using such a combination, an image-based smart cell sorter was first proposed by Nitta *et al.*[66], and was later upgraded from the original version by Isozaki *et al.[*68] (Figure 2.4B). In this intelligent cell sorter, the sample cells were focused through a two-step three-dimensional (3D) on-chip

hydrodynamic cell focuser, thus achieving the goal of keeping the sample cells in the centre of the microfluidic channel. Virtual-freezing fluorescence imaging (VIFFI)-based photomechanical microscopy was used to obtain sensitive, blur-free images of flowing cells[86]. Velocity meters were used to measure cell flow rates at the VIFFI microscope to predict the time for cells to reach the sorting system. The decision-making part of the sorter used a six-layer CNN for cell classification. The final sorting was done by a dual-membrane push-pull unit sorter. The upgraded sorter has significantly improved throughput and sensitivity compared to the previous initial version using the frequency-division-multiplex-based microscope[87]. To learn more about the distinct types of imaging methods integrated with ML, Isozaki *et al.* have written a detailed review paper on this topic[40].

In the above-mentioned CNN-based intelligent microfluidics for cell classification, the data used to train the network is generated entirely by the device itself. However, in addition to training the network using only self-collected data, enhanced training through a pre-trained network based on the concept of transfer learning is also a feasible approach when self-collected data is limited[88]. To show this, Praljak *et al.* used transfer learning in designing a sickle cell disease (SCD) biochip-based classification scheme to classify sickle red blood cells (sRBC) based on morphological differences produced by progressive sickle hemoglobin (an abnormal form of hemoglobin) polymerisation and sickling features[59]. The SCD biochip is the microfluidic platform for acquiring raw image data[89, 90]. The acquired image data is first segmented by a segmentation network, inspired by SegNet[91] and U-net[92], which is heavily used in the biomedical image segmentation community for image segmentation. To overcome the class data imbalance resulting from the use of a semantic segmentation model[93], a deep residual network called ResNet-50[94] pre-trained on ImageNet[95] was used in the second phase to accomplish the final classification and achieved a final classifying accuracy of 95%.

Similarly, Xia *et al.* applied the image region segmentation technique using faster region-based CNN (Faster-RCNN[96]) and used the generated dataset for fine-tuning a pre-trained DNN to enable the classification of blood cells[71].

CNN has been widely used in cell classification due to its superior performance in deep learning using images. This enables many applications of intelligent microfluidic systems based on CNN, such as deep CNN-aided high-throughput label-free image-based flow cytometry[47, 51, 53, 64], autoencoder CNN-aided single-cell classification[49, 72], CNN-aided label-free sperm quality prediction[50], deep CNN-aided fast antimicrobial susceptibility test[61], CNN-aided image-based estimation of bacterial growth[62], and CNN-aided label-free evaluation of tumour spheres[65].

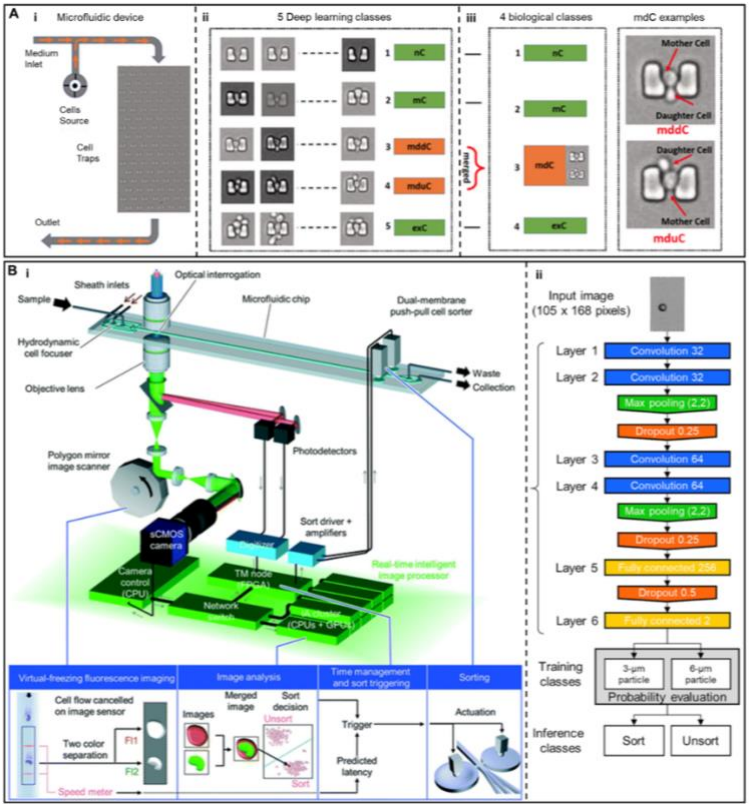

Figure 2.4 Deep learning-based cell classification in microfluidics.

(A) Image-based classification of cells captured in a microfluidic device with traps using deep learning. i: Schematic diagram of the microfluidic device. ii: Deep learning classifies the captured individual trap images into five categories: non-cell trap image (nC), trap image with single mother cell (mC), trap image with single budding cell whose daughter cell is under the mother cell (mddC), trap image with single budding cell whose daughter cell is above the mother cell (mduC), and trap image with multiple cells (exC). iii: mddC and mduC are biologically equivalent, so they are classified as a single budding cell (mdC) in the biological classification. Reproduced under the terms and conditions of CC-BY 4.0 license[52]. Copyright 2021, The Author(s). Published by PLoS. (B) Deep learning-assisted image-based cell sorter. i: Schematic and function of the cell sorter. Sample cells are injected into the microfluidic channel and focused by a hydrodynamic focuser. Images taken by virtual-freezing fluorescence imaging (VIFFI) microscopy are analysed by a deep learning-aided real-time intelligent image processor, resulting in sorting using a dual membrane push-pull cell sorter. Reproduced with permission[68]. Copyright 2020, Royal Society of Chemistry. ii. The adopted deep convolutional neural network (CNN) architecture framework for the cell sorter. Reproduced with permission[66]. Copyright 2018, Cell.

2.2.3 Other applications of intelligent microfluidics in biotechnology

Intelligent microfluidics is used in areas of biotechnology other than cell classification. Some examples of which are shown in Figure 2.5. One such area is cancer screening using biomarker detection.

Recent studies show that disease diagnosis has entered the era of single-cell, multi-omics analysis, meaning that data analysis and bioinformatics are required to work in tandem[97, 98]. For example, in the diagnosis of pancreatic ductal adenocarcinoma (PDAC, i.e., pancreatic

cancers), researchers have made progress in using various protein biomarkers[99], miRNA and mRNA markers[100], as well as the combination of circulating tumour DNA (ctDNA) and protein markers[101] to improve sensitivity and specificity by eliminating the measurement bias from single marker analysis. In addition to providing a sample collection tool for biomarker detection, intelligent microfluidics offers an ML-driven approach to its complex data analysis. The application of ML models (such as classification tree, K-nearest neighbour, and random forest) shortens the time for biomarker detection while ensuring high accuracy.

Banaei *et al.* created a microfluidic multiplex protein biomarker detection platform based on surface-enhanced Raman spectroscopy (SERS) and used ML algorithms to find key biomarkers for predicting and differentiating diseases with similar biomarkers (*e.g.*, pancreatic cancer, ovarian cancer, and pancreatitis) (Figure 2.5A)[74]. For the acquired Raman spectral information, a combination of classification tree and K-nearest neighbour (K-NN) algorithm was used to find the key biomarkers among various biomarkers (carbohydrate antigen 19–9, human epididymis protein 4, mesothelin, matrix metalloproteinase-7 and mucin 4). By assessing the sensitivity (true positive over positive), specificity (true negative over negative), and accuracy (true positive + true negative over whole samples) of the corresponding results, the proteins HE4, CA19-9 and MUC4 were finally identified as important biomarkers to distinguish between healthy individuals, individuals with pancreatic cancer, individuals with ovarian cancer, and individuals with pancreatitis. Based on this, a decision tree model was built to perform cancer prediction. Similarly, Manak *et al.* used ML-assisted microfluidic devices using random forest (RF)[102] to make risk stratification predictions for cancer patients using in vivo live cell phenotype biomarker assays with single-cell resolution[73].

Intelligent microfluidics can also be utilised to assist in the detection of DNA/RNA. Munoz *et al.* innovated the use of intelligent microfluidics to predict the DNA concentration of unknown

samples (Figure 2.5B)[76]. They took advantage of the fact that in the loop-mediated isothermal amplification (LAMP) reaction, pyrophosphate is formed as a by-product that can precipitate with magnesium ions in solution to form magnesium pyrophosphate[103, 104], which allows for the replication of DNA. The target DNA samples and LAMP reaction solution mixture are encapsulated in thousands of sub-nanolitre scale droplets by incorporating them in a microfluidic 3D droplet generator. Encapsulated droplets were incubated in microcentrifuge tubes at 67 °C for 2 h and then incubated at 80 °C for 2 min. Raw image datasets were obtained by bright-field and fluorescence imaging of the incubated droplets. This image dataset was first extracted from the image patches of interest by a speeded up robust features (SURF)-based bag of visual text creation model[105], and then a RF classifier was built for the final prediction of DNA concentration. Also, using microdroplet technology, Fleming *et al.* introduced a semi-supervised deep generation model for background removal in RNA sequencing, thus ensuring the accuracy of counting[75]. This model can determine empty and non-empty droplets, learn background RNA profiles, and perform RNA counting from non-empty droplets. Similarly, Alvarez *et al.* used a semi-supervised expectation maximisation (EM) model for noise filtering of single-cell RNA sequence counts[77].

Another area that employs intelligent microfluidics in biotechnology is the enhancement of the acquired cell information. In order to extract information from the low-resolution images collected by a lens-free microfluidic cell detection system, Li *et al.* proposed a deep learning-based feature fusion algorithm for lens-free cell imaging (Figure 2.5C)[78]. The lens-free microfluidic imaging system used a light-emitting diode (LED) to illuminate the complementary metal oxide semiconductor (COMS) image sensor for the purpose of capturing and outputting cell shadow images (low resolution) as the cell sample flows through the microfluidic channel. This low-resolution set of cell-shaded images was passed through a self-

encoding fusion network to obtain the final fused reconstructed images. Compared to conventional algorithms, this work improved the average ratio of information entropy and standard deviation of images by 7.69% and 22.2%, respectively, resulting in more efficient integration of cellular features. In addition, Honrado *et al.* designed a recurrent neural network (RNN) to enhance the expression of cell features from the electric current signal collected by a microfluidic electrical impedance flow cytometer, resulting in a theoretical cell description rate of 2500 cells per second[79].

Moreover, intelligent microfluidics has also enabled many other applications in biotechnology, such as cytotoxicity analysis for identifying cell killing events caused by specific chemicals or cells with the aid of CNN[80], cellular immunoassays for fast, accurate and highly paralleled immune status monitoring with the aid of CNN[81], cell trajectory predictions to determine the movement of blood cells in microfluidic channels using a self-organising map model[82], and the construction of bi-directional interfaces between biological tissue and human-made devices with the aid of multilayer perceptron (MLP)[83].

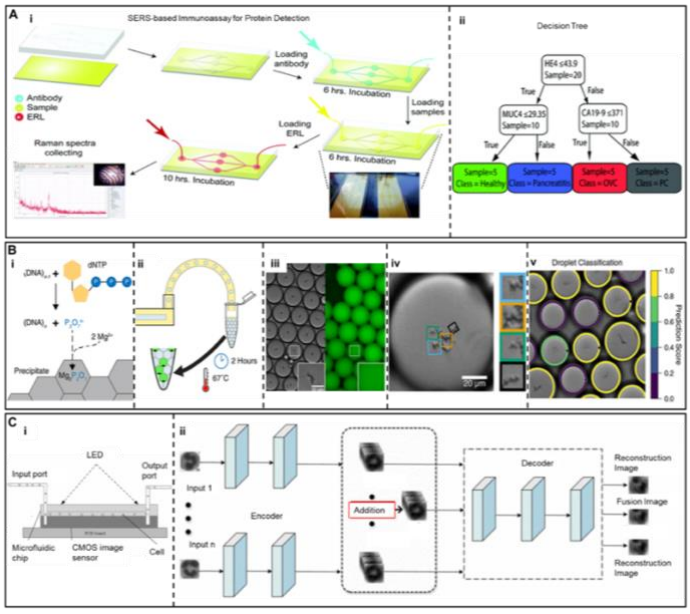

Figure 2.5 Other applications of intelligent microfluidics in biotechnology.

(A) Prediction of diseases with overlapping biomarkers by analysing protein biomarkers using intelligent microfluidics. i: Device fabrication and dataset acquisition flow chart. ii: Classification using decision tree ML model. Reproduced with permission[74]. Copyright 2019, Royal Society of Chemistry. (B) Analysis of loop-mediated isothermal amplification (LAMP) of DNA by intelligent microfluidics. i: Schematic diagram of LAMP reaction. ii: Microdroplet generation and incubation. iii: Bright field and fluorescence imaging of microdroplets. iv: Key features extraction. v: DNA concentration prediction. Reproduced with permission[76]. Copyright 2020, American Chemical Society. (C) Feature enhancement of cellular images by deep learning. i: Schematic diagram of lens-free microfluidic imaging system. ii: Architecture diagram of the converged network. Reproduced with permission[78]. Copyright 2020, IEEE.

2.3 Intelligent Microfluidics in Chemistry

The field of chemistry has also embraced intelligent microfluidics. The application of intelligent microfluidics in chemistry can be divided into two categories: one for the optimisation of chemical reactions and the other for detecting matter. Table 2.2 summarises intelligent microfluidic platforms for applications in chemistry.

Efforts to merge microfluidics with machine learning (ML) in chemistry include reaction optimisation, matter detection, and novel sensing methods[28, 106–112]. Zhou *et al.*[28] pioneered using reinforcement learning (RL) to find optimal reaction conditions in droplet-based microreactors, reporting faster discovery of synthetic routes. Yet, their demonstration focuses on a narrow set of reactions, raising questions about general applicability to more complex syntheses or multi-step processes. Likewise, Rizkin *et al.*[106] paired machine learning with an automated microreactor platform for polymerisation studies, significantly trimming experimental cycles. Despite indicating improved yield predictions, they provided

limited insights into potential throughput bottlenecks or the reproducibility of results across different catalysts.

In matter detection, some studies[107, 111] examined glucose assays and ultrafine particle dosimeters, respectively, emphasising real-time measurement. While they achieved rapid detection with minimal reagents on paper-based or PCB-based microfluidic chips, the reliance on stable droplet generation and controlled environmental conditions leaves open the question of robustness in variable field conditions. Similarly, Hadikhani *et al.*[108] used deep learning to analyse water–isopropanol droplets optically, but their approach presupposed consistent droplet size and flow rates, which is a scenario not guaranteed outside well-tuned laboratory setups. Additional works (*e.g.*, Mercan *et al.*[110]) implement colourimetric microfluidic assays integrated with smartphone capture and ML classifiers, underscoring the potential for point-of-care testing but again stopping short of validation under various environments. Finally, while Roy *et al.*[112] showcased droplet-based microfluidic freeze detection for ice nucleation experiments, highlighting a novel environmental application, the scope was narrowly focused on a single phenomenon without clarifying broader use cases.

A recurring limitation in the works in this field is the lack of standardised evaluation criteria, with few authors comparing their new ML-based microfluidic systems directly against conventional bench-scale instruments or industry protocols. Moreover, cost-effectiveness often goes underreported, leaving it unclear whether these prototypes could feasibly replace or complement established chemical analysis workflows. In summary, the studies[28, 106–112] confirm that intelligent microfluidic strategies can accelerate chemical experiments and expand detection capabilities, but scalability, repeatability, and direct comparisons with established analytical methods remain significant issues for future research.

Table 2.2 Summary of applications of intelligent microfluidics in chemistry.

Category	Application	ML algorithm	Experimental setup	Comments	Reference
Chemical reaction optimisation	Optimisation of chemical reactions in microdroplets (Pomeranz–Fritsch synthesis of iso-quinolines, Friedlander synthesis of substituted quinolines, synthesis of ribose phosphate, and reactions between 2,6-dichlorophenolindophenol and ascorbic acid) by using reinforcement learning (RL)	Markov decision process (MDP)	Microfluidics: microdroplet reactant solutions from two different syringes mixed up through a T-junction Machine learning: TensorFlow on a PC	–	[28]
	Using ML-assisted automated microchemical reactors and in situ infrared thermal imaging to	MLP	Microfluidics: continuous flow microfluidic reactor platform	–	[106]

	optimise polymerisation reactions (mapping the reaction space of zirconium metallocene polymerisation catalysts and obtaining basic kinetic parameters)		containing two syringes for different reactant solutions Machine learning: combined MATLAB and LabVIEW for real-time environment control on an Arduino module. Network built by Python scientific stack on a PC		
Matter detection	Prediction of glucose concentration by bringing a flowing solution of glucose oxidase (GOx), horseradish peroxidase (HRP) and potassium iodide (KI) into contact with glucose in a paper-based microfluid	MLP	Microfluidics: thread/paper based analytical device (μTPAD) has a top layer of single-sided tape with a centre perforation covered with a blank chromatography paper circle, a sandwich layer of double-sided tape with a centre perforation surrounded by nine circular holes, and a bottom layer	–	[107]

		with nine circular perforations with threads Machine learning: Neural Network Toolbox in MATLAB on a PC		
Image-based non-invasive method of measuring the concentration of each component of a water/alcohol mixture in a microfluidic chip by optically monitoring the flow of droplets and measuring the flow rate of the same mixture	CNN	Microfluidics: microfluidic chip fabricated from PDMS containing a flow-focusing geometry to generate water- isopropanol droplets in silicone oil Machine learning: OpenCV and scikit-image in Python used to do image preparation and TensorFlow used to build the network on a PC	–	[108]

	Quantification of ion concentrations using oxidised multi-walled carbon nanotubes as a microfluidic circuit defined by a single bulk probe	Unsupervised: hierarchical clustering analysis (HCA), PCA Supervised: LDA	Microfluidics: a PDMS microfluidic chip manufactured by polymerisation and scaffold removal (PSR) Machine learning: MATLAB used for PCA and HCA. scikit-learn Python library used for LDA	Evaluation and extraction of dataset features using unsupervised HCA and PCA. The data is then used for classification and quantitative prediction through supervised LDA	[109]
	Detection of glucose in artificial saliva (modified by a mixture of potassium iodide, potassium iodide + chitosan and 3,3,5,5-tetramethylbenzidine detection) by smartphone photography of a paper-based microfluidic platform	LDA, gradient boosting classifier (GBC), RF	Microfluidics: the PAD is made by wax printing on Whatman filter paper Machine learning: photos taken by two Android (Reeder P10 and Samsung J7) and two iOS (iPhone 6S and iPhone 7) smartphones and then transferred to a PC for processing by MATLAB	This work compared the prediction performance of LDA, GBC and RF under different colourimetric methods. These techniques exhibit dissimilar performance in detecting different biomarkers	[110]

	Microfluidic ultra-fine particle dosimeter based on an electrical detection method and ML assisted algorithms detects air quality by measuring size distribution (number concentration, mean moving diameter, geometric standard deviation) and particle density	MLP	Microfluidics: printed circuit board (PCB)-based ultra-fine particle analysis microfluidic chip consisting of a hybrid diffusion discharger, two PCB substrates and a Faraday cup Machine learning: Raspberry Pi (+3B) used to pass signals to the signal processing module to retrieve ultrafine particles (UFP) information from the current dataset using Python scripts	–	[111]
	Temperature-controlled microfluidic platform with multiple individually processable temperature zones and on-chip temperature sensors for high-throughput ice	AlexNet	Microfluidics: a PDMS-made straight microfluidic channel with flow-focusing droplet-generator	The network is built by fine-tuning AlexNet using the concept of transfer learning	[112]

	nucleation detection in liquid droplets	Machine learning: AlexNet contained in MATLAB deep learning toolbox on a PC

2.3.1 Intelligent microfluidics for chemical reaction optimisation

A lot of research goes into optimising chemical reactions to find the best combination of reaction conditions to improve the results (increased yield, faster reaction, etc.). One challenge in applying ML to chemical reaction optimisation is determining which correct data types should be selected for training. Many factors affect chemical reactions, but not every one of them is worthy of being taken as the input training data. It is important to find the optimum conditions for industrial chemical processes, as an increase in yield by 1% (for example) could result in considerable savings to the company, and greater profit. One traditional optimisation method is the controlled variable method (changing one experimental condition at a time while fixing all other conditions)[113]. However, due to the correlation between the individual conditions, it is also likely that the optimal reaction condition will be missed using this method[28]. Thus, despite the challenge, it is generally worthwhile to use ML for optimising chemical reactions that make commercial sense or generate harmful wastes.

Zhou *et al.* took advantage of the fast reaction property of microdroplet reactions (reactions can be accelerated by 103 to 106 times[114], and integrated it with reinforcement learning (RL) to develop a deep reaction optimiser (DRO) model capable of optimising microdroplet reactions within 30 min (Figure 2.6A)[28]. The DRO model is a long short-term memory (LSTM) architecture built on the classical Markov decision process (MDP) in RL[115]. This work used a T-junction to mix the reactant solution from two syringes and sprayed it in a high pressure and high voltage desorption electrospray ionisation source with a mass spectrometer to monitor the microdroplet reaction. After setting up the experiment, they validated the model's performance through four microdroplet chemical reactions: the Pomeranz–Fritsch synthesis of

iso-quinoline, the Friedlander synthesis of substituted quinolines, the synthesis of ribose phosphate, and the reaction between 2,6-dichlorophenol (DCIP) and ascorbic acid.

A chemical reaction can also be optimised to reduce the amount of the produced waste. To show this, Rizkin *et al.* designed an automated, high-throughput, intelligent microfluidic reactor integrated with in situ infrared thermography to study metallocene-catalysed polymerisation reactions (Figure 2.6B)[106]. Aided by a Bayesian regularised back-propagation neural network with nine hidden-layer neurons and kinetic modelling[116], the authors reduced the chemical waste of the reaction by two orders of magnitude and minimised the catalytic discovery time from weeks to hours.

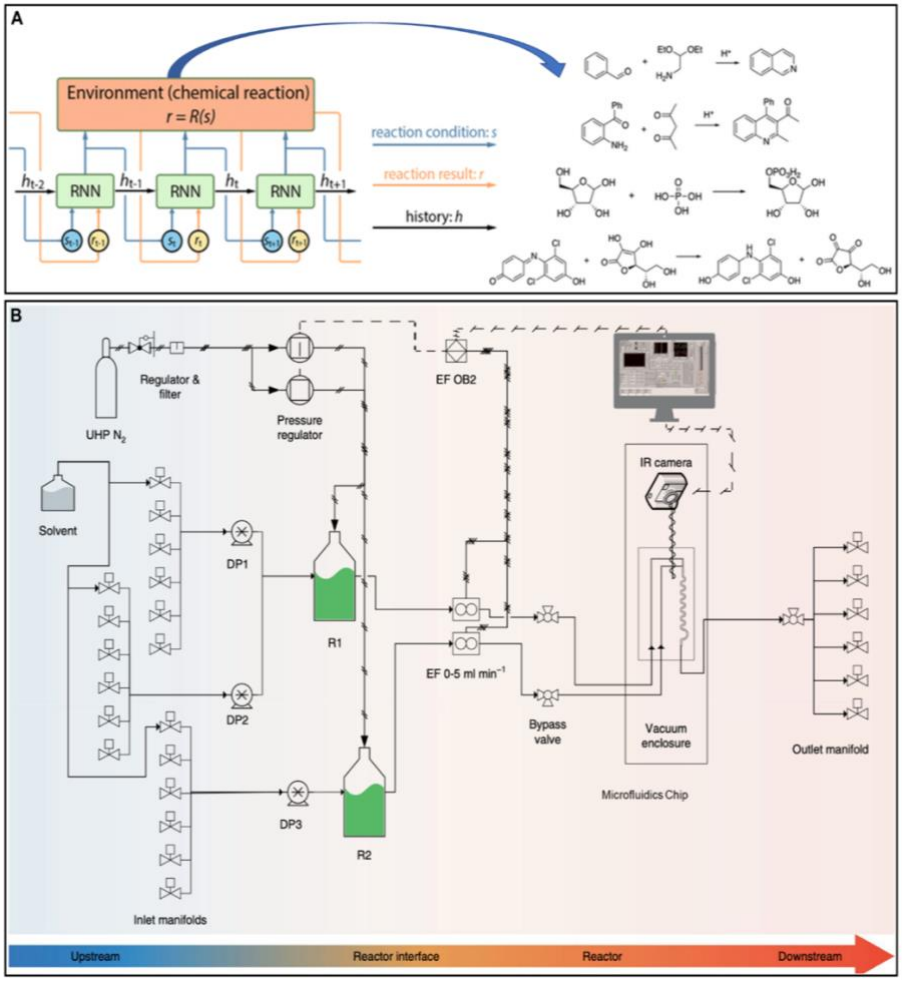

Figure 2.6 Intelligent microfluidics for chemical reaction optimisation.

(A) Schematic diagram of optimisation of chemical reactions using reinforcement learning (RL). Reproduced with permission[28]. Copyright 2017, American Chemical Society. (B) Process flow diagram of an automated thermal imaging microreactor based on intelligent microfluidics, where UHP stands for ultra-high purity, DP stands for electromagnetic dosing pumps, R1/2 stands for reagent reservoirs, EF OB2 is a pressure controller, EF 0–5 ml/min stands for mass flow meters and their flow rates, and IR stands for infrared. Reproduced with permission[106]. Copyright 2020, Springer Nature.

2.3.2 Intelligent microfluidics for matter detection

Intelligent microfluidics can be used for the detection of certain matter. Matter is detected either by using chemically treated substances or by the characteristics of the matter itself (particle size, shape and so on). ML assists in matter detection by discovering potential features of substances and processing data quickly and robustly.

For detecting chemicals, Lee *et al.* described two paper-based microfluidic devices for detecting glucose concentration[107]. Analysis of colour intensity (caused by the oxidation of iodine by iodine-based enzymes in glucose detection, which in turn produces a yellow-brown colour) by MLP networks achieved 94.4% accuracy for glucose concentration detection using a thread/paper-based analytical device (μTPAD), and 91.2% accuracy for glucose concentration detection using a 3D microfluidic paper-based analytical device (3D-μPAD). Also, Mercan *et al.* used a microfluidic paper-based analysis device as a reaction vehicle for detecting glucose concentration and performing colourimetric analysis[110]. The method achieved a classification accuracy of up to 98.24% using a mobile device for picture analysis by implementing LDA, gradient boosting classifier (GBC) and RF (Figure 2.7A). Instead of using colour comparison to determine the chemical concentration, Hadikhani *et al.* used a DNN to

analyse patterns of water-isopropanol (IPA) microdroplet streams generated in the oil phase for predicting the concentration of IPA[108].

The physical characteristics of the matter itself can also be used for identification by intelligent microfluidic devices. Recently, Lee *et al.* designed a microfluidic ultrafine particle dosimeter that can measure both size distribution (numerical concentration, mean moving diameter, and geometric standard deviation) and particle density with the aid of a fully connected network (Figure 2.7B)[111]. As another example, Silva *et al.* developed an ML-assisted capacitive microfluidic sensor that implements hierarchical clustering analysis (HCA), PCA and LDA to classify and monitor the concentration of metal ions in liquids based on the differential electrostatic adsorption characteristics of ions[109]. Furthermore, phase transitions of matter can also be studied with intelligent microfluidics. For instance, Roy *et al.* developed an automated droplet freeze detection method using a DNN-aided temperature-controlled microfluidic device[112].

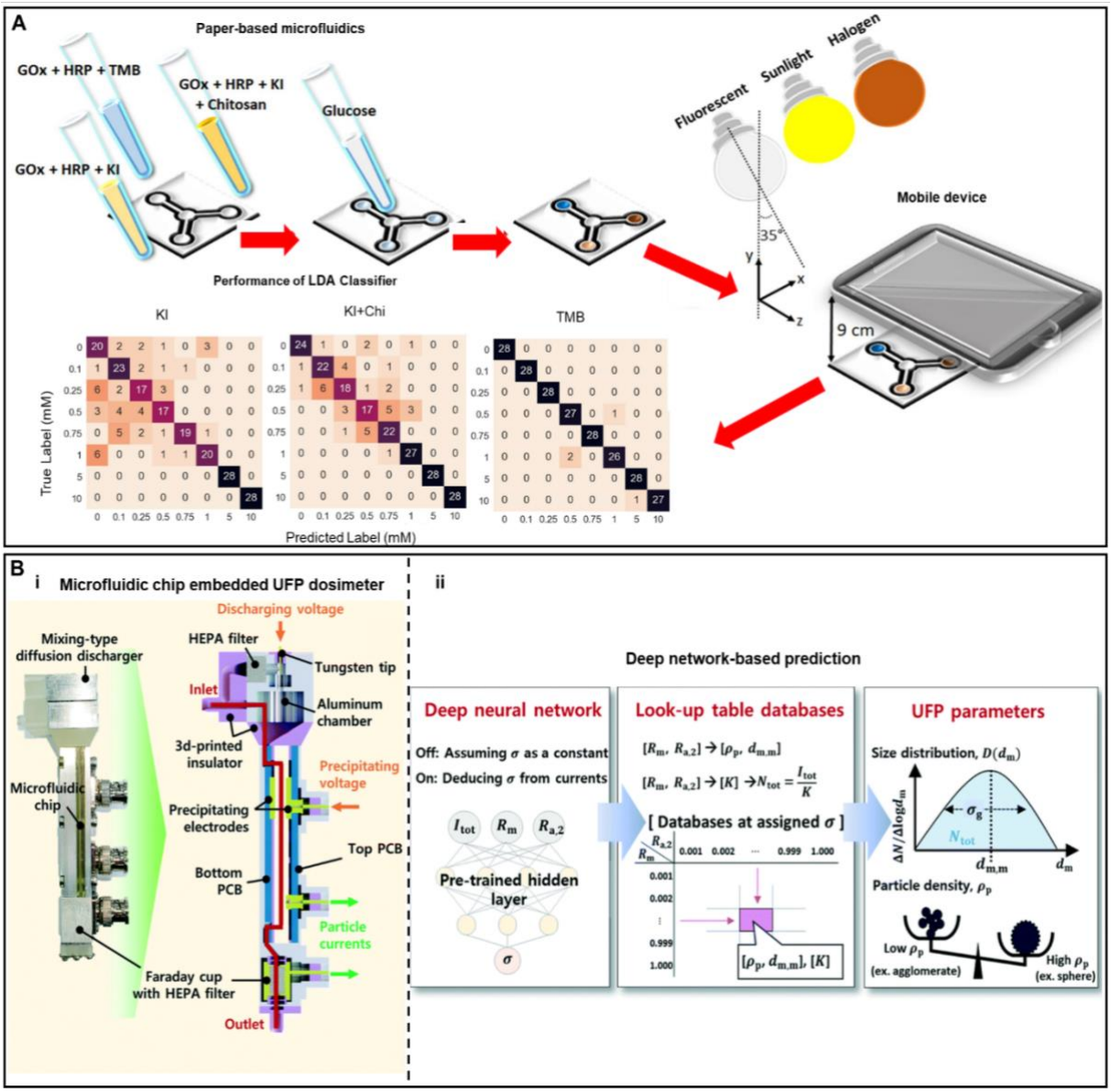

Figure 2.7 Intelligent microfluidics for matter detection.

(A) Schematic diagram showing the paper-based microfluidic movable glucose measurement. The sample reacts with a chemical solution on a paper-based microfluidic device, where GOx stands for glucose oxidase, HRP stands for peroxidase from horseradish, TMB stands for 3, 3′ , 5, 5′ -tetramethylbenzidine, KI stands for potassium iodide and Chi stands for chitosan. Image acquisition and data analysis are performed with mobile devices for glucose concentration prediction. Reproduced with permission[110]. Copyright 2021, Elsevier. (B) Schematic

diagram of the ML-assisted microfluidic ultrafine particle (UFP) dosimeter. i: Schematic diagram of the microfluidic UFP dosimeter. ii: ML models for retrieving the size distribution and density of UFPs based on the database table. Reproduced with permission[111]. Copyright 2021, Royal Society of Chemistry.

2.4 Microfluidic Device Development using ML

In addition to using existing microfluidic device designs as vehicles for collecting relevant data and using ML to analyse the collected data, ML can also be used to explore, analyse, and develop microfluidic devices. This includes microfluidic fluid control, image quality enhancement, microfluidic sensors, thermal control microfluidics, coding markers, microfluidic device self-check, acoustic microfluidics, and microfluidic device manufacturing calibration, as summarised in Table 2.3.

Many research efforts on using ML to design, control, or enhance microfluidic devices, focusing on droplet generation, fluid flow patterns, sensor calibration, and device manufacturing[30, 117–119, 121–123, 125–129, 131–133, 135, 137]. For instance, Mahdi and Daoud[117] use an MLP to predict droplet sizes in water–oil emulsions, demonstrating 95% accuracy under controlled conditions but providing minimal information on real-world fluid variability or operational costs. Stoecklein *et al.*[30] show that a CNN can reverse-engineer pillar sequences for flow sculpting, yet their proof-of-concept remains validated only in simulation or ideal flow regimes, leaving physical reproducibility largely untested. Meanwhile, Khor *et al.*[118] emphasise droplet break-up prediction with shape descriptors, but the technique's generalisability to complex multiphase flows (blood, reagents with particulates) remains unclear.

Another trend is RL-based device control, exemplified by Dressler *et al.*[121], who demonstrate dynamic microfluidic flow adjustment. Despite promising results in laminar flow control, they do not systematically benchmark their approach against simpler controllers (*e.g.*, PID) or detail computational overhead. Additionally, Zhu *et al.*[127] describe distributed colourimetric pressure sensors for microfluidic networks, calibrating them via K-NN regression, which simplifies local pressure readings but raises questions about how sensor drift or temperature fluctuations might degrade performance over extended usage. For fabrication innovations, Wang *et al.*[137] propose an automated calibration approach for 3D-printed microfluidic devices, yet cost, repeatability of prints, and material constraints require further scrutiny to confirm large-scale viability.

Though these works underscore ML's potential to reduce trial-and-error in chip design and fluid management, two common shortcomings emerge: 1) Lack of robust cost or throughput metrics to prove practical advantages over existing industrial processes; and 2) Lack of standardisation, where one group might define success purely by correct flow rate prediction; another may emphasise device lifetime or calibration ease. Without consistent baseline references or widely used benchmarks, direct cross-study comparisons remain speculative. Overall, while works in this field[30, 117–137] highlight how ML can accelerate microfluidic development cycles, they also confirm that extensive real-world testing, consistent performance metrics, and thorough cost analysis are vital to push such ML-augmented platforms from laboratory demonstrations to common engineering practice.

Table 2.3 Summary of microfluidic chip design and optimisation using ML.

Category	Application	ML algorithm	Experimental setup	Comment	Reference
Microfluidic fluid control (droplet)	Analysis of factors influencing microdroplet size for water-in-oil emulsions in microfluids by neural networks	MLP	Microfluidics: droplet generation through T-shaped structured microfluidic channels Machine learning: N/A	–	[117]
	Combination of an autoencoder with a droplet classifier to discover features representing droplet characterisations in microfluids. Identification and prediction of droplet	Autoencoder, MLP	Microfluidics: droplet generation through flow-focusing nozzles. The generated droplets are injected through a syringe into hydrophobic microchannels Machine learning: PyTorch library in Python on a PC	An autoencoder is used to extract features and descript the droplet, and the generated labelled data are feed to an MLP Network for break-up prediction	[118]

	break-up droplet in concentrated emulsions				
	Combination of artificial intelligence to predict and manufacture poly (D, L-lactide-co-glycans) (PLGA) microparticles in different size produced by microfluidic systems in single or multi-particle form.	MLP	Microfluidics: microfluidic chip comprising Mitos P-Pumps injection port, an in-line Mitos flow sensor for detecting fringe, and a T-connector. Machine learning: Statistica software (version 13.3) on a PC	–	[119]
Microfluidic fluid control (continuous flow)	Reverse design flow sculpture using deep learning in pillar-based microfluidic channel	CNN	Microfluidics: moveable pillar based microfluidic channels Machine learning: Theano platform on a PC with NVIDIA K20 T GPU and postprocessing and analysis using NVIDIA Geforce GTX Titan Black	–	[30]

	Image-based prediction of the fluid behaviour in stochastic microfluidic mixers	CNN	Microfluidics: simulation of a stochastic microfluidic mixer network. Machine learning: PyTorch library in Python on a PC	–	[120]
Microfluidic fluid control (continuous flow & droplet)	Determination of the effective positioning interface between two mixed flows in a microchannel under laminar flow conditions, and dynamic control of droplet size in segmented flows using RL	Deep Q-networks (DQN), model-free Episodic controllers (MFEC)	Microfluidics: a Y-shaped hydrophobic microfluidic channel for generating laminar flows; a hydrophobic microfluidic channel with a T-junction for generating microdroplets Machine learning: Keras and Theano in Python on PC with NVIDIA Quadro K2000 GPU for DQN. sklearn in Python on the same PC for MFEC	The DQN and MFEC algorithms can perform above human level for laminar flow and droplet control on a variety of time scales	[121]

	Flow visualisation experiments using laser-induced fluorescence in capillary microchannels for four biphasic systems (ethyl acetate/ water, 2-pentyl alcohol/water, methyl isobutyl ketone/water and heptane/water) revealed two-phase liquid flow patterns (slug flow, droplet flow, slug-droplet flow, parallel flow, annular flow, dispersed flow and irregular flow). The experiment creates a map of the different flow patterns to	Unsupervised: PCA Supervised: decision tree	Microfluidics: T-shaped structured microfluidic channels fabricated by polyether-ether-ketone (PEEK). Machine learning: scikit-learn package in Python on a PC	Evaluation and extraction of dataset features using unsupervised PCA. These data are then used for classification and quantitative prediction through supervised decision tree	[122]

	delineate their root causes of formation using ML				
Image quality enhancement	A microfluidic chip and deep learning based portable imaging flow cytometer that removes motion blur	U-net-like CNN	Microfluidics: microfluidic channels fixed using a 3D printed holder and connected to a peristaltic pump Machine learning: combination of Arduino and a PC with NIVIDA GTX 1080 GPU	–	[123]
	Automatic compensation of phase aberration in digital holographic microscopy assisted by ML. The effectiveness of the method was demonstrated by monitoring the morphology	CNN	Microfluidics: continuous flow microfluidic flow chamber Machine learning: N/A	–	[124]

	of bone cells under a high microfluidic shear stress				
Microfluidics sensor	Calibrating soft microfluidic sensor using deep learning to address the drawbacks of non-linearity and response lag of soft sensors to simultaneously estimate the magnitude and location of contact pressure	Hierarchical recurrent sensing network	Microfluidics: a 3D printer was used to create the mold for the embossing pattern and the polymer layer embedded in the microfluidic channels was made by pouring a liquid silicone elastomer into the mold Machine learning: MATLAB on a PC	The first work to use recurrent neural network (RNN) for estimating contact pressure and position of soft sensors which have highly nonlinear and hysteresis characteristics	[125]
	Evaluation of a gait motion generation method using only two microfluidic sensors by means of a class-supervised deep learning model	Sequential encoder network (SEN), alignment network (AliN), motion	Microfluidics: A layer of silicone was cast using a 3D printed mold, bonded to a spin-coated bottom silicone layer and liquid metal compounds (eutectic indium gallium; EGaIn) were injected into the microchannels and signal wires were inserted directly into the	The device can complete gait motion generation with the help of semi-supervised deep learning using only two soft microfluidic sensors	[126]

		representation network (MRN)	microchannels to fabricate the microfluidic soft sensors Machine learning: *PyTorch* in Python on a PC		
	Application of ML-assisted sensor calibration methods for real-time detection of local pressures in microfluidic networks	K-NN regression	Microfluidics: microfluidic chips manufactured by a combination of standard silicon-based microfabrication and PDMS-based heterogeneous integration processes Machine learning: scikit-image in Python used for image processing and scikit-learn in Python used for network-building on a PC	–	[127]
	Thermal control of continuous flow microfluidic chemical reactors using non-	MLP	Microfluidics: microfluidic chip containing a high-speed PWM-controlled water-cooled thermoelectric	The used of ML lowers the total cumulative computation time by two orders of magnitude	[128]

Thermal control of microfluidics	contact infrared thermography combined with computer vision (CV) and predictive artificial neural networks		module constructed from bondable PTFE Machine learning: MATLAB on a PC with Intel i7-8550U CPU, 16 GB RAM and NVIDIA GeForce 980 M	compared to the case using a proportional integral derivative (PID) controller	
	Using ML to analyse a combination of normalised spectral and time-resolved photoluminescence data of CdTe quantum dot emission to accurately sense the temperature of microfluidic (and potentially nanofluidic) devices	CNN, MLP	Microfluidics: CdTe quantum dots immobilised by a microfluidic device printed on an Asiga 3D printer using PR48 resin Machine learning: Keras API with TensorFlow backbone on a PC	This work compared the performance of CNN and fully connected MLP Network. The fully connected MLP Network outperforms the CNN	[129]
Coding marker	Decoding and content quantification of bio-sample	RF	Microfluidics: the FEMTOPRINT technology is used to produce negative	–	[130]

	co-encapsulated coloured polystyrene bead-triggered images of individual droplets in droplet inflow by using a bright-field microscope		dies to be copied into PDMS microfluidic chips Machine learning: OpenCV and scikit-image in Python on a SUSE Linux Enterprise Server 11 machine with 60 cores		
	Electronic barcoding of particles by depositing a thin oxide film on the upper part of the particle and classification of particle barcodes by supervised learning	SVM	Microfluidics: continuous flow microfluidics Machine learning: MATLAB on PC	–	[131]
	Using ML to detect and classify attack types on the fully programmable valve	LR, LDA, K-NN, classification	Microfluidics: microfluidic biochip consisting of a two-dimensional array of fluidic chambers (each of which is	This work compared the performance of LR, LDA, K-NN, CART and NB at the nodes and	[132]

Microfluidic device self-check	array (FPVA) microfluidic platform	and regression trees (CART), Gaussian Naive Bayes (NB)	surrounded by up to four independently addressable valves for programmable interconnection of the chambers), which allows the designer to configure the valves to create an arbitrary network of channels to connect the desired chambers Machine learning: scikit-learn in Python on a PC	valves. CART outperforms other ML algorithms with a 97% prediction accuracy	
	Checking the health of electrodes by applying deep RL of droplet transport on digital microfluidic biochips (DMFBs) and providing reliable fluid manipulation	MDP	Microfluidics: PCB-based digital microfluidic biochip which contains a 6 × 6 electrode array (each side of the array has a reservoir module to dispense different droplets of reagent, and each electrode can be controlled individually)	–	[133]

	to obtain an RL-based droplet routing process		Machine learning: Raspberry Pi (3B+) with RL agent installed used to generate control signals to the control board		
	Adjustment of various process parameters of microfluidics to reduce sample heterogeneity and internal/ external perturbations through feedback control combined with deep learning	CNN	Microfluidics: microfluidic sensor platform designed by CODES sensor network technology (Liu *et al.*, 2016) on the Coulter principle Machine learning: N/A	–	[134]
Acoustic microfluidics	Design of microfluidic channel architecture using surface acoustic wave with support of deep learning,	MLP	Microfluidics: the microfluidic device consists of a piezoelectric substrate to generate surface acoustic waves and microfluidic channels. A 50 μm wall	–	[135]

	which completes the design of the microparticle pattern		separates the air pocket used along the SAW propagation path to reduce acoustic attenuation from the fluidic structure domain Machine learning: MATLAB on a PC with NVIDIA Titan RTX GPU		
	Acoustic manipulation of particles using RL and particle-based machine vision position determination	Multi-armed Bandit algorithms	Microfluidics: microfluidic chips made by wet etching from fused silica glass Machine learning: N/A	–	[136]
Microfluidic device manufacturing calibration	Calibration of 3D printers using a fast and accurate 3D printing calibration method based on CV to ensure high	CNN	Microfluidics: N/A. Machine learning: PyTorch in Python on a PC	–	[137]

	quality microfluidic 3D printing

2.4.1 Fluid control using intelligent microfluidics

Fluidic control in microfluidic devices is a popular direction of study, with both deep learning and classical ML used to achieve this. ML algorithms (such as PCA and autoencoder) provide a powerful means of analysing the major influences in fluid control. Other ML algorithms (such as decision trees and CNNs) reduce the workload in fluid control research. They even offer the possibility of reverse fluid pattern design[30], which is not available using traditional statistical analysis.

Figure 2.8A shows a recent work of feature extraction and prediction of various fluid flow patterns in microfluidics using classical ML architectures (PCA and decision trees)[122]. This work explored the flow characteristics of four solvents (ethyl acetate/water, 2-pentyl alcohol/water, methyl isobutyl ketone/water, and heptane/water) in seven different flow patterns (slug, droplet, slug-droplet, parallel, annular, dispersed, and irregular) by laser-induced fluorescence flow visualisation experiments. They developed a decision tree model capable of predicting flow patterns with 93% accuracy using six key characteristics obtained from PCA (i.e., total flow rate, flow ratio between two phases, capillary number and One Sorge number of the aqueous phase, as well as Weber number and velocity of the organic phase).

In terms of the control of microdroplets, Mahdi *et al.* used an MLP network to understand how different parameters affect the size of microdroplets produced using a T-junction[117]. Khor *et al.* used a convolutional autoencoder model to achieve 91.7% accuracy in predicting microdroplet break-up in a tapered microfluidic channel[118]. Also, Damiati *et al.* developed a size prediction method for poly (D, L-lactide-co-glycans) (PLGA) microparticles produced in single or multi-particle form using intelligent microfluidics[119].

In addition to microdroplets, ML can also analyse the behaviour of continuous flows. As an example, Wang *et al.* used a CNN for fluid behaviour prediction of stochastic microfluidic mixers[120]. Although most of the works use supervised learning, Dressler *et al.*, for the first time, used RL based on deep Q-networks (DQN) and model-free episodic controllers to establish models that are capable of accomplishing control over laminar flow and droplet size[121].

Unlike most of the work where the analysis of the generated flow patterns is performed in a fixed microfluidic device, Stoecklein *et al.* showed that a sequence of columns that can move their position within the microfluidic channel can be used to achieve the desired flow shapes[30]. This work explored a sampling method for selecting training data called high dimensional model representation (HDMR)[138], and combined it with PCA to validate the applicability of deep learning in the field of flow sculpting by building a CNN model capable of taking a known flow shape as the input and a sequence of columns in a microfluidic device as the output for sculpting the flow inside the microchannel (Figure 2.8B).

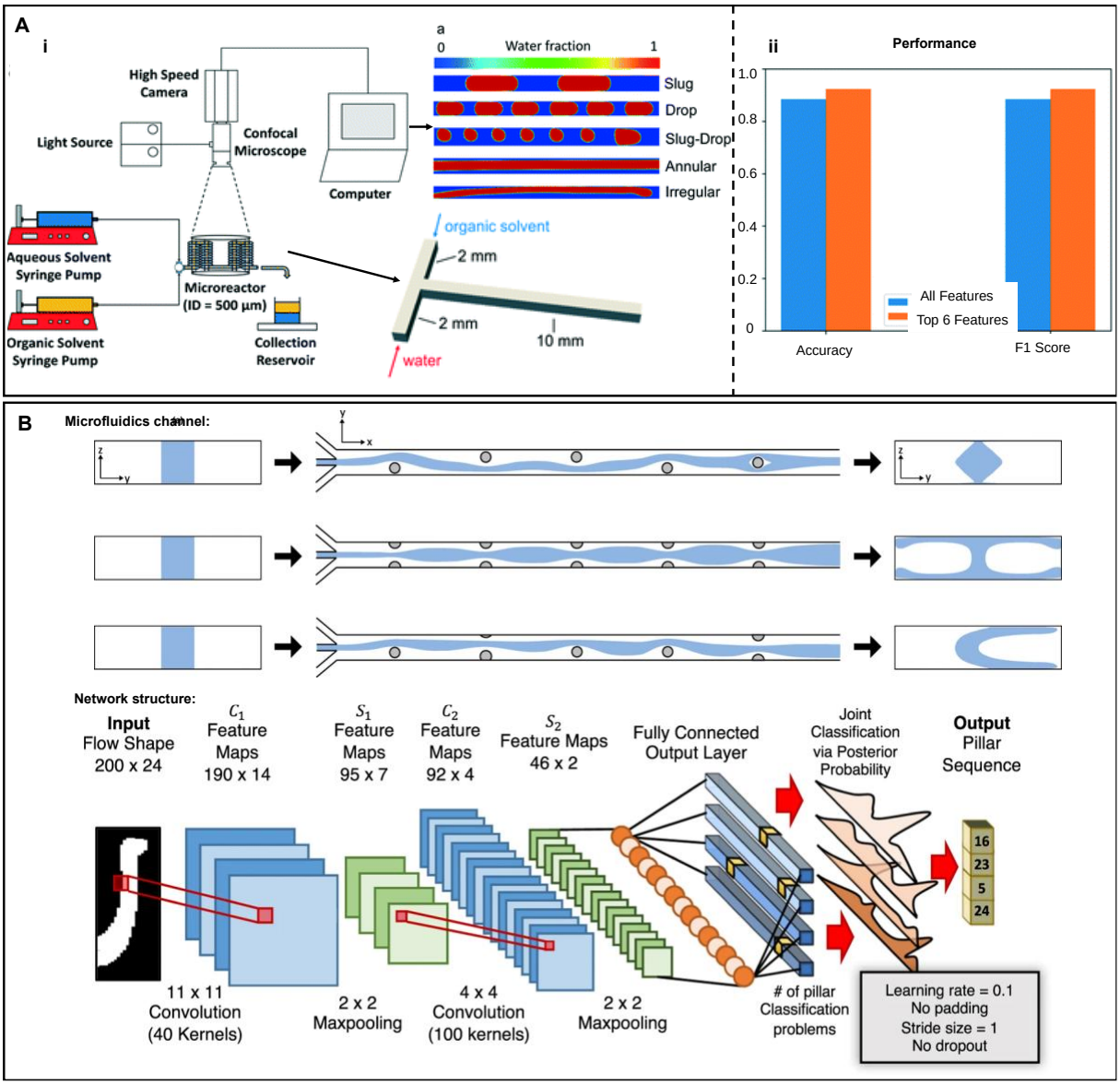

Figure 2.8 Fluid control using intelligent microfluidics.

(A) Analysis of microfluidic fluid liquid-liquid flow patterns using ML. i: Schematic diagram of the experimental setup for flow visualisation of two-phase flow patterns. ii: Evaluation of the decision tree ML model for flow pattern prediction. The table indicates the prediction performance of decision tree ML models, where the top 6 features are predefined using PCA and F1 score is the harmonic mean of precision and recall. Reproduced with permission[122]. Copyright 2020, Royal Society of Chemistry. (B) Reverse design of various flow shapes

through image-based deep learning. A sequence of columns in the microfluidic channel is used to perform flow sculpting. A deep CNN is used to translate the input images into the corresponding column sequences. Reproduced under the terms and conditions of CC-BY 4.0 license[30]. Copyright 2017, The Author(s). Published by Springer Nature.

2.4.2 Additional examples of using intelligent microfluidics for device development

The development of intelligent microfluidic devices is not limited to the control of fluids. Researchers have also applied ML to various other branches of microfluidic devices. Among them, ML serves as an analytical and predictive tool, providing researchers with the means to deal with complex data. Inside this complex data, some features are challenging to interpret (*e.g.*, analysing behavioural actions with fewer sensors installed). Thus, when this happens, feature extraction cannot be done quickly and effectively, even by specialists in the field, without ML.

The identification of different markers by ML to encode microparticles is one example (Figure 2.9A)[131]. This method enables each microparticle to have a unique coding under an electrical impedance sensor by depositing a thin layer of oxide on the upper part of the particle (the frequency-dependent impedance characteristics of the particle can be tuned by adjusting the thickness and dielectric properties of this oxide) and then using an SVM to detect the coding that corresponds to the particle. In addition to this, with the help of an image-based RF classifier, Svensson *et al.* developed a method for coding microdroplets using coloured beads[130].

The development of microfluidic soft sensor devices is also an area that can be well integrated with ML. Soft sensors have become an important development direction in the research of wearable devices because of their easy wearability and high ductility[139, 140]. However, when trying to use soft microfluidic sensors to obtain information about nodes that can perform

complex motions (*e.g.*, human joints), many sensors are needed to connect to these nodes to generate sensor data. In this regard, Kim *et al.* used semi-supervised learning to generate natural gait motion in 3D space using only two soft strain sensors with the goal of gait reconstruction (Figure 2.9B)[126]. They proposed a three-part network model consisting of a deep full-body motion-Net[141] based sequential encoder network (SEN), a fully connected neural network-based alignment network (AliN), and a deep autoencoder based motion representation network (MRN). Among them, SEN is used to extract the sequential feature vectors of the data collected by the sensors, MRN is used to map the low-dimensional potential motion vector to the high-dimensional human gait motion, and AliN is used to map the sequential feature vector to the potential motion vector. This work eliminates much of the interference noise by reducing the number of microfluidic soft sensors to two and uses a semi-supervised learning model to enable more accurate generation of gait motion even with smaller calibration data sets. In addition to strain sensors, intelligent microfluidics can be used for making soft pressure sensors. Han *et al.* used an RNN-based hierarchical recurrent sensing network model to characterise the pressure response of microfluidic soft sensors[125]. In addition, Zhu *et al.* used K-NN regression to accomplish the dynamic prediction of pressure distribution in a microfluidic channel by monitoring the reflected colour generated by optical cavities on colourimetric interferometers embedded in a silicon substrate[127].

Self-checking of microfluidic devices is another area where ML can be utilised. Liang *et al.* used RL to enable droplets to avoid contact with damaged electrodes during transport in digital microfluidic chips, so that the partially damaged digital microfluidic chip could still function (Figure 2.9C)[133]. In addition to this, Wang *et al.* recently developed an adaptive microfluidic system that can take sample heterogeneity and internal/external perturbations into account[134]. This system used CNN to control a programmable pressure pump based on real-time conditions,

thus ensuring that the sample can maintain the same flow rate regardless of perturbations. Also, Shayan *et al.* used ML (LR, LDA, K-NN, classification and regression trees and Gaussian Naïve Bayes) to inspect a fully programmable valve array flow microfluidic platform (FPVA) for enhancing the safety of FPVA biochips[132].

ML also plays a supporting role in thermal microfluidics and acoustofluidics. For example, Rizkin *et al.* used a DNN to achieve the temperature control of a microfluidic reactor by analysing infrared thermographic images. This method lowers the total cumulative computation time by two orders of magnitude compared to the case of using a conventional PID controller. In contrast to using infrared thermographic images, Lewis *et al.* used cadmium telluride (CdTe) quantum dot fluorescent data as the learning object to achieve temperature prediction by using CNN and MLP in microfluidic devices[129]. As for acoustofluidics, Yiannacou *et al.* achieved the manipulation and active ordering of particles inside a microfluidic chip by applying RL to control bulk acoustic waves[136]. Whereas surface acoustic waves (SAW) have shown the advantage of being able to manipulate microparticles more quickly and accurately than bulk acoustic waves. Raymond *et al.* developed a method that uses a DNN trained by images of pre-solved acoustic fields to design microchannel architectures that can result in desired acoustic fields for patterning microparticles[135].

In addition to assisting in the design of devices, intelligent microfluidics can be used for the quality enhancement of captured images. Görögcs *et al.* used a deep CNN-based model to enhance the quality of acquired images from a portable imaging flow cytometer, thereby improving throughput without losing image quality[123]. Recently, Xiao *et al.* utilised the ResNet-50 structure[94] to realise the automatic phase aberration compensation of images taken by digital holographic microscopy[124]. This work validated the model by monitoring the morphology of living bone cells under high shear stress in a microfluidic channel.

ML can also be used for device calibration. As an example, Wang *et al.* provided a CNN-aided calibration method for 3D printing using microfluidic devices[137]. Using this method, designers only need to print the calibration ruler model once using the microfluidic printer, and then a camera will take a picture of the printed calibration ruler and a standard-sized coin in the same frame. The CNN can use this picture to compensate the theoretical design size based on the actual printed size, thus completing the printer calibration in one go to minimise error.

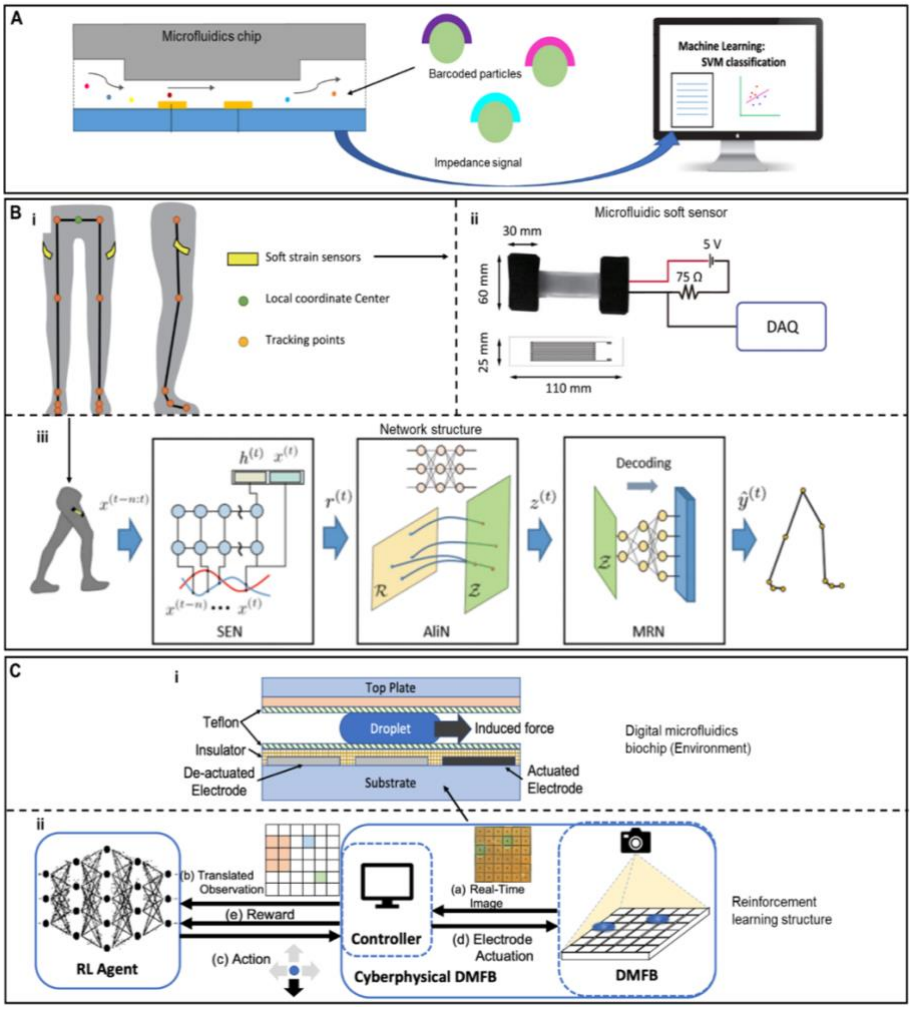

Figure 2.9 Other applications of intelligent microfluidics for device development.

(A) Schematic of the classification of barcode particles using multi-frequency impedance microfluidic cytometry with SVM ML. Reproduced with permission[131]. Copyright 2020,

Elsevier. (B) Schematic diagram of semi-supervised gait generation using two microfluidic soft sensors. i: Locations of the microfluidic soft strain sensors on human legs, and the local coordinate centres and tracking points of motion generation. ii: Schematic diagram of the soft strain sensor, where DAQ stands for data acquisition device. iii: Schematic diagram of the architecture of the semi-supervised gait-motion generation model consists of three DNNs, where SEN stands for sequential encoder network, AliN stands for alignment network, and MRN stands for motion representation network. Reproduced with permission[126]. Copyright 2019, IEEE. (C) Using deep RL to do path planning for microdroplets on a digital microfluidic biochip (DMFB). i: Side-view of the DMFB, where the microdroplet is driven by the electrowetting-on-dielectric (EWOD). ii: The deep network RL framework for microdroplets routing on DMFB. Reproduced under the terms and conditions of CC-BY 4.0 license[133]. Copyright 2020, The Author(s). Published by ICML.

2.5 Conclusion and Outlook

Microfluidics possesses the ability to intersect with different research fields, offering the opportunity to generate a wide variety of datasets for ML. In addition to this, ML can process the generated data to yield innovative and optimised solutions for microfluidics. Despite a wide range of promising applications of intelligent microfluidics, several under-developed and unsolved issues remain to be explored. A guide to the future development of intelligent microfluidics is given below:

How to ensure accuracy in a complex environment? ML techniques require representative data to build an effective ML model for specific applications; therefore, acquired images need to have quality and quantity for building training datasets. Current research is still highly dependent on high-precision and high-resolution image acquisition instruments (*e.g.*,

automated microscopes equipped with optical systems) in a laboratory environment. Although it is possible to construct a more extensive dataset by making as many changes as possible to the environmental conditions under which the images were collected, this is not addressed in most studies. This can result in a model that performs well in the lab but may not be able to demonstrate its capabilities in more complex environments. This challenge will be magnified in more integrated and portable intelligent microfluidic devices.

How to deal with uneven data volume? When training an ML algorithm using an uneven data volume, the ML algorithm will mainly be trained with the majority class of the dataset, thereby compromising its ability to classify minority samples. To solve this problem, techniques such as resampling the training set by human intervention, data augmentation, or cross-validation can be used to generate simulated data for minority samples.

How to provide automation for the platform and experimental design? The potential for using intelligent microfluidics for platform design and experimental control should be explored further. In these cases, intelligent microfluidics is used to enhance system automation and minimise human intervention. Although there are a few good examples of using intelligent microfluidics in this way, such as in the optimisation of chemical synthesis and flow sculpting[28, 30], this area still needs to be further explored.

How to make intelligent microfluidics more widely accepted? At present, intelligent microfluidics is still in the early stages of development, and the devices are used by researchers in a laboratory environment. Making integrated devices and developing corresponding user software will simplify the requirements of users and reduce the complexity of the equipment, resulting in intelligent microfluidics being more widely adopted.

What benefits can cloud-based computing bring to intelligent microfluidics? Currently, most intelligent microfluidic platforms rely on bulky and sophisticated optical instruments and PCs

for data acquisition and training, significantly limiting the portability of intelligent microfluidic platforms. Fortunately, the high availability of cheap microfluidic devices (*e.g.*, paper-based microfluidics), coupled with the constantly improving cameras in smartphones provides the necessary environment for intelligent microfluidics to become available through cloud-based services. The benefit of this combination is that by connecting through the cloud, we can provide richer data for the backend ML models of intelligent microfluidics without using bulky devices, while miniaturising the platform to provide more development possibilities, particularly in point-of-care applications

How to improve the computing capability of intelligent microfluidics in mobile devices? The high-performance capabilities of deep learning often require high-quality ML models trained on massive data, often on the order of terabytes. As such, deploying DNNs in high-performance and miniaturised hardware is challenging but possesses additional benefits. To achieve this, models can be built using central CPUs, graphics processing units (GPUs), and tensor processing units (TPUs) and deployed to mobile devices for inference, which often uses GPUs, field-programmable gate arrays (FPGAs), and application-specific integrated circuits (ASICs). Deep learning using a mobile device itself results in savings in communication bandwidth and a faster response time, because more data is processed on the device and less data needs to be sent to the cloud. Localisation can also improve privacy by keeping sensitive information on mobile devices.

Specifically for this thesis, while sections 2.2 to 2.4 illustrate that intelligent microfluidics has achieved remarkable progress in biotechnology, chemical applications and device fabrication, environmental monitoring remains distinctly underrepresented. Also, most of the current approaches focus on confined laboratory setups, validated on specialised or short-term

experiments. Many authors stress high performance or novel technology demonstrations but do not provide the breadth of data necessary to ascertain real-world reliability.

Several lessons have emerged from the studies:

- Cost and Complexity: Advanced imaging hardware or complex microfluidic designs often prove too expensive or intricate for adoption outside well-funded research facilities.
- Data Heterogeneity: ML accuracy frequently relies on carefully curated datasets with minor morphological variations (*e.g.*, mixed algal species).
- Lack of Standard Benchmarks: Without universally accepted baselines for detection limits, throughput, cost analysis, or even ML metrics, direct comparisons between studies, and thus a coherent "golden rule", are difficult to establish.

These observations not only underscore the gap in on-site, cost-effective vision-based bioparticle detection and monitoring solutions but also shape the forthcoming chapters in this thesis. Building on the above lessons, chapters 4 and 5 target specific shortcomings identified in earlier studies:

Chapter 4: Automated and Intelligent Microfluidic Platform (AIMP)

- Design to handle on-site microalgae detection with emphasis on the ability to detect morphology varying microalgae at the same time.
- Provide cost reporting for components (<£170 total), size reporting, ML training procedures, and a 30-day experiment for microalgae monitoring accuracy check to give a workflow of standard benchmark.
- The system is validated over an extended 30-day experiment (monitoring *Haematococcus pluvialis*), bridging the frequent gap of short-duration lab tests.
- ML inference on a Raspberry Pi ensures a practical route for field deployment.

- The similar development workflow transitions smoothly from environmental applications (microalgae detection) to medical diagnostics, showcasing the adaptability of the vision-based detection and monitoring platform.
- The same hardware–software synergy to a magnetic microbead-based immunoassay, demonstrating rapid detection (<10 minutes) of cytokines such as interferon-gamma (IFN-γ) with ~87% accuracy.

By tackling these issues, cost transparency, durable real-time monitoring, and cross-application adaptability, the subsequent chapters aim to establish a blueprint for backpack-fit or even pocket-fit, intelligent microfluidic platforms in both environmental and clinical contexts. Rather than adhering to narrowly confined laboratory scenarios, they demonstrate an end-to-end approach.

2.6 References

[1] D. Qin, Y. Xia, J. A. Rogers, R. J. Jackman, X.-M. Zhao, and G. M. Whitesides, "Microfabrication, Microstructures and Microsystems," in *Microsystem Technology in Chemistry and Life Science*, A. Manz and H. Becker Eds. Berlin, Heidelberg: Springer Berlin Heidelberg, 1998, pp. 1-20.

[2] G. M. Whitesides, "The origins and the future of microfluidics," *Nature*, vol. 442, no. 7101, pp. 368-373, 2006.

[3] C.-T. Kung *et al.*, "Microfluidic synthesis control technology and its application in drug delivery, bioimaging, biosensing, environmental analysis and cell analysis," *Chem. Eng. J.*, vol. 399, p. 125748, 2020.

[4] D. Holmes and S. Gawad, "The Application of Microfluidics in Biology," *Methods Mol. Biol.*, vol. 583, pp. 55-80, 2010, doi: 10.1007/978-1-60327-106-6_2.

[5] M. G. Roper, "Cellular analysis using microfluidics," *Anal. Chem.*, vol. 88, no. 1, pp. 381-394, 2016.

[6] J. Sibbitts, K. A. Sellens, S. Jia, S. A. Klasner, and C. T. Culbertson, "Cellular analysis using microfluidics," *Anal. Chem.*, vol. 90, no. 1, pp. 65-85, 2018, doi: 10.1021/acs.analchem.7b04519.

[7] D. J. Beebe, G. A. Mensing, and G. M. Walker, "Physics and applications of microfluidics in biology," *Annu. Rev. Biomed. Eng.*, vol. 4, no. 1, pp. 261-286, 2002.

[8] I. Oita, H. Halewyck, B. Thys, B. Rombaut, Y. Vander Heyden, and D. Mangelings, "Microfluidics in macro-biomolecules analysis: macro inside in a nano world," *Anal. Bioanal. Chem.*, vol. 398, no. 1, pp. 239-264, 2010.

[9] B. Bruijns, A. Van Asten, R. Tiggelaar, and H. Gardeniers, "Microfluidic devices for forensic DNA analysis: A review," *Biosensors*, vol. 6, no. 3, p. 41, 2016.

[10] J. C. Contreras-Naranjo, H.-J. Wu, and V. M. Ugaz, "Microfluidics for exosome isolation and analysis: enabling liquid biopsy for personalised medicine," *Lab Chip*, vol. 17, no. 21, pp. 3558-3577, 2017.

[11] P. Chen, D. Chen, S. Li, X. Ou, and B.-F. Liu, "Microfluidics towards single cell resolution protein analysis," *TrAC, Trends Anal. Chem.*, vol. 117, pp. 2-12, 2019.

[12] X. Hou *et al.*, "Interplay between materials and microfluidics," *Nat. Rev. Mater.*, vol. 2, no. 5, p. 17016, 2017.

[13] K. Ren, Y. Chen, and H. Wu, "New materials for microfluidics in biology," *Curr. Opin. Biotechnol.*, vol. 25, pp. 78-85, 2014.

[14] J. C. Jokerst, J. M. Emory, and C. S. Henry, "Advances in microfluidics for environmental analysis," *Analyst*, vol. 137, no. 1, pp. 24-34, 2012.

[15] C.-T. Kung, C.-Y. Hou, Y.-N. Wang, and L.-M. Fu, "Microfluidic paper-based analytical devices for environmental analysis of soil, air, ecology and river water," *Sens. Actuators, B*, vol. 301, p. 126855, 2019.

[16] K. i. Ohno, K. Tachikawa, and A. Manz, "Microfluidics: applications for analytical purposes in chemistry and biochemistry," *Electrophoresis,* vol. 29, no. 22, pp. 4443-4453, 2008.

[17] A. Abou-Hassan, O. Sandre, and V. Cabuil, "Microfluidics in inorganic chemistry," *Angew. Chem., Int. Ed.,* vol. 49, no. 36, pp. 6268-6286, 2010.

[18] S. R. Bowman, G. Angeli, C. Potts, and C. D. Manning, "A large annotated corpus for learning natural language inference," *arXiv preprint arXiv:1508.05326,* 2015.

[19] F.-Y. Wang *et al.*, "Where does AlphaGo go: From church-turing thesis to AlphaGo thesis and beyond," *Zidonghua Xuebao,* vol. 3, no. 2, pp. 113-120, 2016.

[20] J. Heaton, N. G. Polson, and J. H. Witte, "Deep learning in finance," *arXiv preprint arXiv:1602.06561,* 2016.

[21] M. Haenlein and A. Kaplan, "A brief history of artificial intelligence: On the past, present, and future of artificial intelligence," *Calif. Manage Rev.,* vol. 61, no. 4, pp. 5-14, 2019.

[22] R. Davis, "Expert Systems: Where are we? And where do we go from here?," *AI Mag.,* vol. 3, no. 2, p. 3, 1982.

[23] H. Wang and B. Raj, "On the origin of deep learning," *arXiv preprint arXiv:1702.07800,* 2017.

[24] S. C. Terry, J. H. Jerman, and J. B. Angell, "A gas chromatographic air analyser fabricated on a silicon wafer," *IEEE Trans. Electron Devices,* vol. 26, no. 12, pp. 1880-1886, 1979.

[25] D. S. Tawfik and A. D. Griffiths, "Man-made cell-like compartments for molecular evolution," *Nat. Biotechnol.,* vol. 16, no. 7, pp. 652-656, 1998.

[26] L. Shang, Y. Cheng, and Y. Zhao, "Emerging droplet microfluidics," *Chem. Rev.,* vol. 117, no. 12, pp. 7964-8040, 2017.

[27] N. Convery and N. Gadegaard, "30 years of microfluidics," *Micro Nano Eng.,* vol. 2, pp. 76-91, 2019.

[28] Z. Zhou, X. Li, and R. N. Zare, "Optimising chemical reactions with deep reinforcement learning," *ACS Cent. Sci.,* vol. 3, no. 12, pp. 1337-1344, 2017.

[29] H. Kobayashi *et al.*, "Label-free detection of cellular drug responses by high-throughput bright-field imaging and machine learning," *Sci. Rep.,* vol. 7, no. 1, p. 12454, 2017.

[30] D. Stoecklein, K. G. Lore, M. Davies, S. Sarkar, and B. Ganapathysubramanian, "Deep learning for flow sculpting: Insights into efficient learning using scientific simulation data," *Sci. Rep.,* vol. 7, p. 46368, 2017.

[31] Y. LeCun, Y. Bengio, and G. Hinton, "Deep learning," *Nature,* vol. 521, no. 7553, pp. 436-444, 2015.

[32] J. De Jong, R. G. Lammertink, and M. Wessling, "Membranes and microfluidics: a review," *Lab Chip,* vol. 6, no. 9, pp. 1125-1139, 2006.

[33] Y. He, Y. Wu, J.-Z. Fu, and W.-B. Wu, "Fabrication of paper-based microfluidic analysis devices: a review," *RSC Adv.,* vol. 5, no. 95, pp. 78109-78127, 2015.

[34] P. Kim, K. W. Kwon, M. C. Park, S. H. Lee, S. M. Kim, and K. Y. Suh, "Soft lithography for microfluidics: a review," *Biochip J.,* vol. 2, no. 1, pp. 1-11, 2008.

[35] B. K. Gale *et al.*, "A review of current methods in microfluidic device fabrication and future commercialisation prospects," *Inventions,* vol. 3, no. 3, p. 60, 2018.

[36] A. Shrestha and A. Mahmood, "Review of deep learning algorithms and architectures," *IEEE Access,* vol. 7, pp. 53040-53065, 2019.

[37] M. Abadi *et al.*, "Tensorflow: A System for Large-Scale Machine Learning," in *12th USENIX Symposium on Operating Systems Design and Implementation*, 2016, pp. 265-283.

[38] Y. Jia *et al.*, "Caffe: Convolutional Architecture for Fast Feature Embedding," in *Proceedings of the 22nd ACM International Conference on Multimedia*, 2014, pp. 675-678.

[39] A. Paszke *et al.*, "Pytorch: An imperative style, high-performance deep learning library," *arXiv preprint arXiv:1912.01703,* 2019.

[40] A. Isozaki *et al.*, "AI on a chip," *Lab Chip,* vol. 20, no. 17, pp. 3074-3090, 2020.

[41] E. A. Galan, H. Zhao, X. Wang, Q. Dai, W. T. Huck, and S. Ma, "Intelligent Microfluidics: The Convergence of Machine Learning and Microfluidics in Materials Science and Biomedicine," *Matter,* vol. 3, no. 6, pp. 1893-1922, 2020.

[42] S. R. Dabbagh, F. Rabbi, Z. Doğan, A. K. Yetisen, and S. Tasoglu, "Machine learning-enabled multiplexed microfluidic sensors," *Biomicrofluidics,* vol. 14, no. 6, p. 061506, 2020.

[43] J. Molinski, A. Tadimety, A. Burklund, and J. X. Zhang, "Scalable Signature-Based Molecular Diagnostics Through On-chip Biomarker Profiling Coupled with Machine Learning," *Ann. Biomed. Eng.*, vol. 48, no. 10, pp. 2377-2399, 2020.

[44] M. P. McRae, G. Simmons, J. Wong, and J. T. McDevitt, "Programmable bio-nanochip platform: a point-of-care biosensor system with the capacity to learn," *Acc. Chem. Res.,* vol. 49, no. 7, pp. 1359-1368, 2016.

[45] J. Riordon, D. Sovilj, S. Sanner, D. Sinton, and E. W. Young, "Deep learning with microfluidics for biotechnology," *Trends Biotechnol.,* vol. 37, no. 3, pp. 310-324, 2019.

[46] B. Guo *et al.*, "High-throughput, label-free, single-cell, microalgal lipid screening by machine-learning-equipped optofluidic time-stretch quantitative phase microscopy," *Cytometry, A,* vol. 91, no. 5, pp. 494-502, 2017.

[47] Y. J. Heo, D. Lee, J. Kang, K. Lee, and W. K. Chung, "Real-time image processing for microscopy-based label-free imaging flow cytometry in a microfluidic chip," *Sci. Rep.,* vol. 7, no. 1, p. 11651, 2017.

[48] Y. Jiang *et al.*, "Label-free detection of aggregated platelets in blood by machine-learning-aided optofluidic time-stretch microscopy," *Lab Chip,* vol. 17, no. 14, pp. 2426-2434, 2017.

[49] I. Constantinou *et al.*, "Self-learning microfluidic platform for single-cell imaging and classification in flow," *Micromachines,* vol. 10, no. 5, p. 311, 2019.

[50] C. McCallum *et al.*, "Deep learning-based selection of human sperm with high DNA integrity," *Commun. Biol.*, vol. 2, no. 1, p. 250, 2019.

[51] Y. Zhou *et al.*, "Intelligent classification of platelet aggregates by agonist type," *Elife,* vol. 9, p. e52938, 2020.

[52] M. Ghafari *et al.*, "Complementary performances of convolutional and capsule neural networks on classifying microfluidic images of dividing yeast cells," *PLoS One,* vol. 16, no. 3, p. e0246988, 2021.

[53] G. Gopakumar, K. H. Babu, D. Mishra, S. S. Gorthi, and G. R. S. Subrahmanyam, "Cytopathological image analysis using deep-learning networks in microfluidic microscopy," *J. Opt. Soc. Am. A,* vol. 34, no. 1, pp. 111-121, 2017.

[54] D. K. Singh, C. C. Ahrens, W. Li, and S. A. Vanapalli, "Label-free, high-throughput holographic screening and enumeration of tumor cells in blood," *Lab Chip,* vol. 17, no. 17, pp. 2920-2932, 2017.

[55] J. Ko *et al.*, "Combining machine learning and nanofluidic technology to diagnose pancreatic cancer using exosomes," *ACS Nano,* vol. 11, no. 11, pp. 11182-11193, 2017.

[56] Y. Wang *et al.*, "Detection of non-small cell lung cancer cells based on microfluidic polarisation microscopic image analysis," *Electrophoresis,* vol. 40, no. 8, pp. 1202-1211, 2019.

[57] K. Joshi *et al.*, "A Machine Learning-Assisted Nanoparticle-Printed Biochip for Real-Time Single Cancer Cell Analysis," *Adv. Biosyst.,* vol. 4, no. 11, p. 2000160, 2020.

[58] N. Nissim, M. Dudaie, I. Barnea, and N. T. Shaked, "Real-time stain-free classification of cancer cells and blood cells using interferometric phase microscopy and machine learning," *Cytometry, A,* vol. 99, no. 5, pp. 511-523, 2020.

[59] N. Praljak *et al.*, "Integrating deep learning with microfluidics for biophysical classification of sickle red blood cells," *bioRxiv*, p. doi.org/10.1101/2020.07.01.181545, 2020, doi: 10.1101/2020.07.01.181545.

[60] V. Rizzuto *et al.*, "Combining microfluidics with machine learning algorithms for RBC classification in rare hereditary hemolytic anemia," *Sci. Rep.,* vol. 11, no. 1, p. 13553, 2021.

[61] H. Yu *et al.*, "Phenotypic antimicrobial susceptibility testing with deep learning video microscopy," *Anal. Chem.,* vol. 90, no. 10, pp. 6314-6322, 2018.

[62] K. Kim, S. Kim, and J. S. Jeon, "Visual estimation of bacterial growth level in microfluidic culture systems," *Sensors,* vol. 18, no. 2, p. 447, 2018.

[63] K. Ahuja *et al.*, "Toward point-of-care assessment of patient response: a portable tool for rapidly assessing cancer drug efficacy using multifrequency impedance cytometry and supervised machine learning," *Microsyst. Nanoeng.,* vol. 5, no. 1, p. 34 2019.

[64] H. Kobayashi *et al.*, "Intelligent whole-blood imaging flow cytometry for simple, rapid, and cost-effective drug-susceptibility testing of leukemia," *Lab Chip,* vol. 19, no. 16, pp. 2688-2698, 2019.

[65] Z. Zhang, L. Chen, Y. Wang, T. Zhang, Y.-C. Chen, and E. Yoon, "Label-Free Estimation of Therapeutic Efficacy on 3D Cancer Spheres Using Convolutional Neural Network Image Analysis," *Anal. Chem.,* vol. 91, no. 21, pp. 14093-14100, 2019.

[66] N. Nitta *et al.*, "Intelligent image-activated cell sorting," *Cell,* vol. 175, no. 1, pp. 266-276. e13, 2018.

[67] M. Sesen and G. Whyte, "Image-based single cell sorting automation in droplet microfluidics," *Sci. Rep.,* vol. 10, no. 1, p. 8736, 2020.

[68] A. Isozaki *et al.*, "Intelligent image-activated cell sorting 2.0," *Lab Chip,* vol. 20, no. 13, pp. 2263-2273, 2020.

[69] B. Turan *et al.*, "A pillar-based microfluidic chip for T-cells and B-cells isolation and detection with machine learning algorithm," *ROBOMECH J.,* vol. 5, no. 1, p. 27, 2018.

[70] D. Rossi, D. Dannhauser, M. Telesco, P. A. Netti, and F. Causa, "CD4+ versus CD8+ T-lymphocyte identification in an integrated microfluidic chip using light scattering and machine learning," *Lab Chip,* vol. 19, no. 22, pp. 3888-3898, 2019.

[71] T. Xia, R. Jiang, Y. Q. Fu, and N. Jin, "Automated Blood Cell Detection and Counting via Deep Learning for Microfluidic Point-of-Care Medical Devices," *IOP Conf. Ser.: Mater. Sci. Eng. ,* vol. 646, p. 012048, 2019, doi: 10.1088/1757-899X/646/1/012048.

[72] D. Stallmann, J. P. Göpfert, J. Schmitz, A. Grünberger, and B. Hammer, "Towards an Automatic Analysis of CHO-K1 Suspension Growth in Microfluidic Single-cell Cultivation," *arXiv preprint arXiv:2010.10124,* 2020.

[73] M. S. Manak *et al.*, "Live-cell phenotypic-biomarker microfluidic assay for the risk stratification of cancer patients via machine learning," *Nat. Biomed. Eng.*, vol. 2, no. 10, pp. 761-772, 2018.

[74] N. Banaei, J. Moshfegh, A. Mohseni-Kabir, J. M. Houghton, Y. Sun, and B. Kim, "Machine learning algorithms enhance the specificity of cancer biomarker detection using SERS-based immunoassays in microfluidic chips," *RSC Adv.*, vol. 9, no. 4, pp. 1859-1868, 2019.

[75] S. J. Fleming, J. C. Marioni, and M. Babadi, "CellBender remove-background: a deep generative model for unsupervised removal of background noise from scRNA-seq datasets," *BioRxiv*, p. doi.org/10.1101/791699, 2019.

[76] H. E. Munoz *et al.*, "Fractal LAMP: Label-free analysis of fractal precipitate for digital loop-mediated isothermal nucleic acid amplification," *ACS Sens.*, vol. 5, no. 2, pp. 385-394, 2020.

[77] M. Alvarez *et al.*, "Enhancing droplet-based single-nucleus RNA-seq resolution using the semi-supervised machine learning classifier DIEM," *Sci. Rep.*, vol. 10, no. 1, p. 11019 2020.

[78] S. Li, L. Dai, J. Li, C. Wang, and N. Yu, "A Deep Learning Feature Fusion Algorithm Based on Lensless Cell Detection System," in *2020 IEEE 15th International Conference on Solid-State & Integrated Circuit Technology (ICSICT)*, 3-6 Nov. 2020 2020, pp. 1-3, doi: 10.1109/ICSICT49897.2020.9278322.

[79] C. Honrado, J. S. McGrath, R. Reale, P. Bisegna, N. S. Swami, and F. Caselli, "A neural network approach for real-time particle/cell characterisation in microfluidic impedance cytometry," *Anal. Bioanal. Chem.*, pp. 3835–3845, 2020.

[80] S. Sarkar *et al.*, "Machine learning-aided quantification of antibody-based cancer immunotherapy by natural killer cells in microfluidic droplets," *Lab Chip*, vol. 20, no. 13, pp. 2317-2327, 2020.

[81] Y. Song *et al.*, "Machine learning-based cytokine microarray digital immunoassay analysis," *Biosens. Bioelectron.*, vol. 180, p. 113088, 2021.

[82] H. Bachratý, K. Bachratá, M. Chovanec, I. Jančigová, M. Smiešková, and K. Kovalčíková, "Applications of machine learning for simulations of red blood cells in microfluidic devices," *BMC Bioinf.*, vol. 21, no. 2, p. 90, 2020.

[83] S. Shchanikov *et al.*, "Designing a bidirectional, adaptive neural interface incorporating machine learning capabilities and memristor-enhanced hardware," *Chaos, Solitons Fractals,* vol. 142, p. 110504, 2021.

[84] D. P. Kingma and J. Ba, "Adam: A method for stochastic optimisation," *arXiv preprint arXiv:1412.6980,* 2014.

[85] S. Sabour, N. Frosst, and G. E. Hinton, "Dynamic routing between capsules," *arXiv preprint arXiv:1710.09829,* 2017.

[86] H. Mikami *et al.*, "Virtual-freezing fluorescence imaging flow cytometry," *Nat. Commun.,* vol. 11, no. 1, p. 1162, 2020.

[87] H. Mikami *et al.*, "Ultrafast confocal fluorescence microscopy beyond the fluorescence lifetime limit," *Optica,* vol. 5, no. 2, pp. 117-126, 2018.

[88] L. Y. Pratt, J. Mostow, C. A. Kamm, and A. A. Kamm, "Direct Transfer of Learned Information Among Neural Networks," presented at the Proceedings of the ninth National conference on Artificial intelligence Anaheim, California, 1991.

[89] Y. Alapan *et al.*, "Sickle cell disease biochip: a functional red blood cell adhesion assay for monitoring sickle cell disease," *Transl. Res.,* vol. 173, pp. 74-91. e8, 2016.

[90] J. A. Little, Y. Alapan, K. E. Gray, and U. A. Gurkan, "SCD-biochip: a functional assay for red cell adhesion in sickle cell disease," *Transl. Res.,* vol. 173, pp. 74-91.e8, 2014.

[91] V. Badrinarayanan, A. Kendall, and R. Cipolla, "Segnet: A deep convolutional encoder-decoder architecture for image segmentation," *IEEE PAMI,* vol. 39, no. 12, pp. 2481-2495, 2017.

[92] O. Ronneberger, P. Fischer, and T. Brox, "U-net: Convolutional Networks for Biomedical Image Segmentation," in *International Conference on Medical Image Computing and Computer-Assisted Intervention*, 2015: Springer, pp. 234-241.

[93] G. Haixiang, L. Yijing, J. Shang, G. Mingyun, H. Yuanyue, and G. Bing, "Learning from class-imbalanced data: Review of methods and applications," *Expert Syst. Appl.,* vol. 73, pp. 220-239, 2017.

[94] K. He, X. Zhang, S. Ren, and J. Sun, "Deep Residual Learning for Image Recognition," in *2016 IEEE Conference on Computer Vision and Pattern Recognition (CVPR)*, 27-30 June 2016 2016, pp. 770-778, doi: 10.1109/CVPR.2016.90.

[95] J. Deng, W. Dong, R. Socher, L.-J. Li, K. Li, and L. Fei-Fei, "ImageNet: A Large-Scale Hierarchical Image Database," in *2009 IEEE Conference on Computer Vision and Pattern Recognition*, 20-25 June 2009 2009, pp. 248-255.

[96] S. Ren, K. He, R. Girshick, and J. Sun, "Faster r-cnn: Towards real-time object detection with region proposal networks," *arXiv preprint arXiv:1506.01497,* 2015.

[97] S.-C. Precision, "Single-Cell Analyses in the Multi-omics Era," *Cancer Cell,* vol. 38, no. 1, pp. 9-10, 2020.

[98] J. M. Perkel, "Single-cell analysis enters the multiomics age," *Nature,* vol. 595, no. 7868, pp. 614-616, 2021.

[99] K. S. Yang *et al.*, "Multiparametric plasma EV profiling facilitates diagnosis of pancreatic malignancy," *Sci. Transl. Med.*, vol. 9, no. 391, p. doi.org/10.1126/scitranslmed.aal3226, 2017.

[100] Z. Yang *et al.*, "A multianalyte panel consisting of extracellular vesicle miRNAs and mRNAs, cfDNA, and CA19-9 shows utility for diagnosis and staging of pancreatic ductal adenocarcinoma," *Clin. Cancer Res.*, vol. 26, no. 13, pp. 3248-3258, 2020.

[101] J. D. Cohen *et al.*, "Combined circulating tumor DNA and protein biomarker-based liquid biopsy for the earlier detection of pancreatic cancers," *Proc. Natl. Acad. Sci. U. S. A.*, vol. 114, no. 38, pp. 10202-10207, 2017.

[102] L. Breiman, "Random forests," *Mach. Learn.*, vol. 45, no. 1, pp. 5-32, 2001.

[103] K. E. Shopsowitz, Y. H. Roh, Z. J. Deng, S. W. Morton, and P. T. Hammond, "RNAi-microsponges form through self-assembly of the organic and inorganic products of transcription," *Small*, vol. 10, no. 8, pp. 1623-1633, 2014.

[104] S. Takagi, Y. Takahashi, K. Sugimura, M. Nishikawa, and Y. Takakura, "Application of Magnesium Pyrophosphate–Based Sponge-Like Microparticles to Enhance the Delivery Efficiency and Adjuvant Effects of Polyriboinosinic-Polyribocytidylic Acid in Immune Cells," *J. Pharm. Sci. (Philadelphia, PA, U. S.)*, vol. 105, no. 2, pp. 766-772, 2016.

[105] H. Bay, A. Ess, T. Tuytelaars, and L. Van Gool, "Speeded-up robust features (SURF)," *Comput. Vis. Image Underst.,* vol. 110, no. 3, pp. 346-359, 2008.

[106] B. A. Rizkin, A. S. Shkolnik, N. J. Ferraro, and R. L. Hartman, "Combining automated microfluidic experimentation with machine learning for efficient polymerisation design," *Nat. Mach. Intell.,* vol. 2, no. 4, pp. 200-209, 2020.

[107] W. Lee, A. Gonzalez, P. Arguelles, R. Guevara, M. J. Gonzalez-Guerrero, and F. A. Gomez, "Thread/paper-and paper-based microfluidic devices for glucose assays employing artificial neural networks," *Electrophoresis,* vol. 39, no. 12, pp. 1443-1451, 2018.

[108] P. Hadikhani, N. Borhani, S. M. H. Hashemi, and D. Psaltis, "Learning from droplet flows in microfluidic channels using deep neural networks," *Sci. Rep.,* vol. 9, no. 1, p. 8114, 2019.

[109] G. S. da Silva *et al.,* "Ordinary microfluidic electrodes combined with bulk nanoprobe produce multidimensional electric double-layer capacitances towards metal ion recognition," *Sens. Actuators, B,* vol. 305, p. 127482, 2020.

[110] Ö. B. Mercan, V. Kılıç, and M. Şen, "Machine learning-based colorimetric determination of glucose in artificial saliva with different reagents using a smartphone coupled μPAD," *Sens. Actuators, B,* vol. 329, p. 129037, 2021.

[111] T.-H. Lee, H.-B. Kwon, W.-Y. Song, S.-S. Lee, and Y.-J. Kim, "Microfluidic ultrafine particle dosimeter using an electrical detection method with a machine-learning-aided algorithm for real-time monitoring of particle density and size distribution," *Lab Chip,* vol. 21, no. 8, pp. 1503-1516, 2021.

[112] P. Roy, M. L. House, and C. S. Dutcher, "A Microfluidic Device for Automated High Throughput Detection of Ice Nucleation of Snomax®," *Micromachines,* vol. 12, no. 3, p. 296, 2021.

[113] J. P. McMullen and K. F. Jensen, "Integrated microreactors for reaction automation: new approaches to reaction development," *Annu. Rev. Anal. Chem.,* vol. 3, pp. 19-42, 2010.

[114] S. Banerjee, E. Gnanamani, X. Yan, and R. N. Zare, "Can all bulk-phase reactions be accelerated in microdroplets?," *Analyst,* vol. 142, no. 9, pp. 1399-1402, 2017.

[115] J. Schmidhuber and S. Hochreiter, "Long short-term memory," *Neural Comput.*, vol. 9, no. 8, pp. 1735-1780, 1997.

[116] D. J. MacKay, "A practical Bayesian framework for backpropagation networks," *Neural Comput.*, vol. 4, no. 3, pp. 448-472, 1992.

[117] Y. Mahdi and K. Daoud, "Microdroplet size prediction in microfluidic systems via artificial neural network modeling for water-in-oil emulsion formulation," *J. Dispersion Sci. Technol.*, vol. 38, no. 10, pp. 1501-1508, 2017.

[118] J. W. Khor, N. Jean, E. S. Luxenberg, S. Ermon, and S. K. Tang, "Using machine learning to discover shape descriptors for predicting emulsion stability in a microfluidic channel," *Soft Matter*, vol. 15, no. 6, pp. 1361-1372, 2019.

[119] S. A. Damiati, D. Rossi, H. N. Joensson, and S. Damiati, "Artificial intelligence application for rapid fabrication of size-tunable PLGA microparticles in microfluidics," *Sci. Rep.*, vol. 10, no. 1, p. 19517 2020.

[120] J. Wang *et al.*, "Predicting the fluid behavior of random microfluidic mixers using convolutional neural networks," *Lab Chip*, vol. 21, no. 2, pp. 296-309, 2021.

[121] O. J. Dressler, P. D. Howes, J. Choo, and A. J. deMello, "Reinforcement learning for dynamic microfluidic control," *ACS Omega*, vol. 3, no. 8, pp. 10084-10091, 2018.

[122] P. Desir, T.-Y. Chen, M. Bracconi, B. Saha, M. Maestri, and D. G. Vlachos, "Experiments and computations of microfluidic liquid–liquid flow patterns," *React. Chem. Eng.*, vol. 5, no. 1, pp. 39-50, 2020.

[123] Z. Göröcs *et al.*, "A deep learning-enabled portable imaging flow cytometer for cost-effective, high-throughput, and label-free analysis of natural water samples," *Light: Sci. Appl.*, vol. 7, no. 1, p. 66, 2018.

[124] W. Xiao *et al.*, "Sensing morphogenesis of bone cells under microfluidic shear stress by holographic microscopy and automatic aberration compensation with deep learning," *Lab Chip*, vol. 21, no. 7, pp. 1385-1394, 2021.

[125] S. Han, T. Kim, D. Kim, Y.-L. Park, and S. Jo, "Use of deep learning for characterisation of microfluidic soft sensors," *IEEE Robot. Autom. Lett.*, vol. 3, no. 2, pp. 873-880, 2018.

[126] D. Kim, M. Kim, J. Kwon, Y.-L. Park, and S. Jo, "Semi-supervised gait generation with two microfluidic soft sensors," *IEEE Robot. Autom. Lett.,* vol. 4, no. 3, pp. 2501-2507, 2019.

[127] X. Zhu, T. Man, X. H. M. Tan, P.-S. Chung, M. A. Teitell, and P.-Y. Chiou, "Distributed colorimetric interferometer for mapping the pressure distribution in a complex microfluidics network," *Lab Chip,* vol. 21, no. 5, pp. 942-950, 2021.

[128] B. A. Rizkin, K. Popovich, and R. L. Hartman, "Artificial Neural Network control of thermoelectrically-cooled microfluidics using computer vision based on IR thermography," *Comput. Chem. Eng.,* vol. 121, pp. 584-593, 2019.

[129] C. Lewis *et al.*, "Use of Machine Learning with Temporal Photoluminescence Signals from CdTe Quantum Dots for Temperature Measurement in Microfluidic Devices," *ACS Appl. Nano Mater.,* vol. 3, no. 5, pp. 4045-4053, 2020.

[130] C. M. Svensson *et al.*, "Coding of experimental conditions in microfluidic droplet assays using colored beads and machine learning supported image analysis," *Small,* vol. 15, no. 4, p. 1802384, 2019.

[131] J. Sui, P. Xie, Z. Lin, and M. Javanmard, "Electronic classification of barcoded particles for multiplexed detection using supervised machine learning analysis," *Talanta,* vol. 215, p. 120791, 2020.

[132] M. Shayan, S. Bhattacharjee, Y.-A. Song, K. Chakrabarty, and R. Karri, "Toward secure microfluidic fully programmable valve array biochips," *IEEE Trans. Very Large Scale Integr. (VLSI) Syst.,* vol. 27, no. 12, pp. 2755-2766, 2019.

[133] T.-C. Liang, Z. Zhong, Y. Bigdeli, T.-Y. Ho, K. Chakrabarty, and R. Fair, "Adaptive Droplet Routing in Digital Microfluidic Biochips Using Deep Reinforcement Learning," presented at the Proceedings of the 37th International Conference on Machine Learning, Proceedings of Machine Learning Research, 2020.

[134] N. Wang, R. Liu, N. Asmare, C.-H. Chu, O. Civelekoglu, and A. F. Sarioglu, "Closed-loop Feedback Control of Microfluidic Cell Manipulation via Deep-learning Integrated Sensor Networks," *Lab Chip,* vol. 21, no. 10, pp. 1916-1928, 2021, doi: 10.1039/D1LC00076D.

[135] S. J. Raymond, D. J. Collins, R. O'Rorke, M. Tayebi, Y. Ai, and J. Williams, "A deep learning approach for designed diffraction-based acoustic patterning in microchannels," *Sci. Rep.,* vol. 10, no. 1, p. 8745, 2020.

[136] K. Yiannacou and V. Sariola, "Controlled Manipulation and Active Sorting of Particles Inside Microfluidic Chips Using Bulk Acoustic Waves and Machine Learning," *Langmuir*, vol. 37, no. 14, pp. 4192-4199, 2021.

[137] J. Wang, K. Liang, N. Zhang, H. Yao, T.-Y. Ho, and L. Sun, "Automated calibration of 3D-printed microfluidic devices based on computer vision," *Biomicrofluidics*, vol. 15, no. 2, p. 024102, 2021.

[138] H. Rabitz and Ö. F. Aliş, "General foundations of high-dimensional model representations," *J. Math. Chem.*, vol. 25, no. 2, pp. 197-233, 1999.

[139] Y.-L. Park, D. Tepayotl-Ramirez, R. J. Wood, and C. Majidi, "Influence of cross-sectional geometry on the sensitivity and hysteresis of liquid-phase electronic pressure sensors," *Appl. Phys. Lett.*, vol. 101, no. 19, p. 191904, 2012.

[140] Y.-L. Park, C. Majidi, R. Kramer, P. Bérard, and R. J. Wood, "Hyperelastic pressure sensing with a liquid-embedded elastomer," *J. Micromech. Microeng.*, vol. 20, no. 12, p. 125029, 2010.

[141] D. Kim, J. Kwon, S. Han, Y.-L. Park, and S. Jo, "Deep full-body motion network for a soft wearable motion sensing suit," *IEEE ASME Trans. Mechatron.*, vol. 24, no. 1, pp. 56-66, 2018

3 CHAPTER 3: AN AUTOMATED AND INTELLIGENT MICROFLUIDIC PLATFORM FOR MICROALGAE DETECTION AND MONITORING

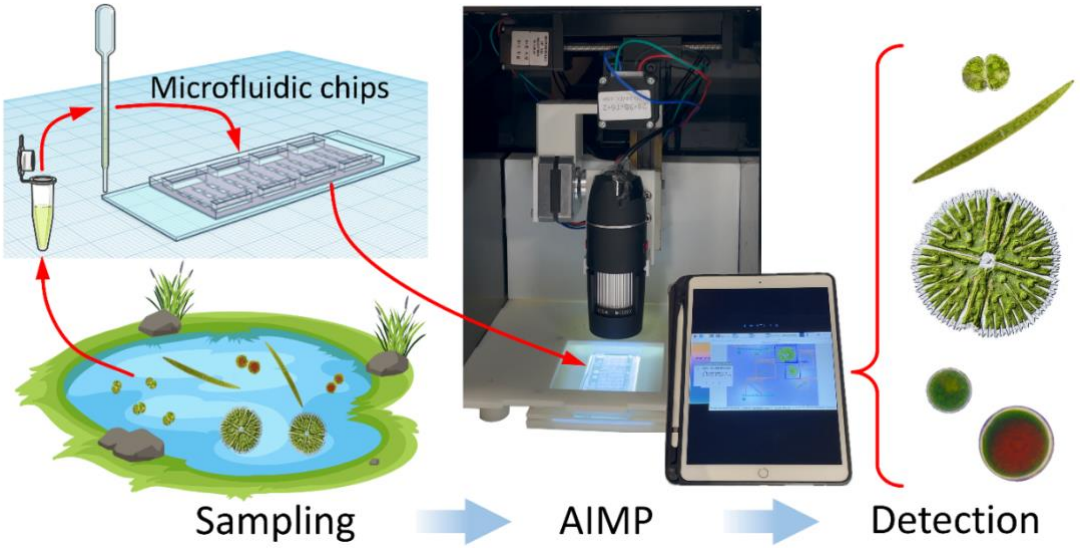

Graphic Table of Contents

Results of this chapter are published in: **J. Zheng**, T. Cole, Y. Zhang, Bayinqiaoge, D. Yuan and S.-Y. Tang (2024). "An automated and intelligent microfluidic platform for microalgae detection and monitoring." Lab on a Chip **24**(2): 244-253.

Author Contributions: Conceptualisation: S.-Y. T. and **J. Z.** Data curation: **J. Z.**, T. C., Y. Z., Bayinqiaoge, and D. Y. Formal analysis: **J. Z.** Funding acquisition: S.-Y. T. Investigation: **J. Z.**, T. C., Y. Z., Bayinqiaoge, D. Y., and S.-Y. T. Methodology: **J. Z.** and S.-Y. T. Supervision: S.-Y. T. Writing (original draft): **J. Z.** and S.-Y. T. Writing (review and editing): T. C., Y. Z., Bayinqiaoge, D. Y., and S.-Y. T.

3.1 Introduction

Microalgae, as single-celled species that obtain nutrients from their aquatic habitat, absorb sunlight, capture carbon dioxide from the air and produce about 50% of atmospheric oxygen, can range in size from a few microns to several hundred microns, depending on the species[1]. Current research on microalgae has been conducted from two main perspectives. One aspect is based on the position of microalgae in the ecological chain to study their impact on the ecosystem as well as on human health. For example, exploring the factors that trigger harmful algal blooms (HABs) due to microalgal overgrowth[2-4], monitoring and predicting HABs events[5, 6], the toxic threat to human health from HABs events[6-8], and wastewater treatment by microalgae[9-11]. Another direction of research on microalgae is to explore their commercial applications, such as biofuels, biopharmaceuticals, nutritional supplements, and cosmetics production[12-16]. Both research directions require the detection and monitoring of microalgae.

As microalgae are not visible to the naked eye, the traditional method of detecting microalgae requires researchers to collect samples from various environmental sites, bring them to the laboratory, image them with a microscope and then analyse them manually based on morphology[17]. Although this method is reliable, there is a significant lag in the analysis of microalgae at the environmental sites sampled as it is both time-consuming and laborious. Therefore, in order to reduce human effort, a few recent studies introduced machine learning (ML) for microalgae detection[18, 19]. For example, Abdullah *et al.*[20] explore the potential of YOLO algorithms in microalgae detection, spanning four distinct algae species. However, it is important to note that solely relying on ML detection algorithms, without additional considerations, does not fully achieve the goal of enabling “sampling and testing” in the field. This limitation persists because ML-based approaches still necessitate a separate and relatively

large laboratory setup (*e.g.*, microscope, computer, *etc.*) for implementation. Consequently, there remains a pressing need to substantially reduce both the time and economic costs associated with microalgae detection.

Microfluidics, a technique for manipulating fluids in microchannels at the micron level, has set the trend for engineering improvements in areas such as flow cytometry[21], microscale chemical synthesis[22] , bioparticle detection[23], and cell culture[24]. Particularly due to the rapid development of ML in recent decades, which has greatly enhanced the ability of microfluidic platforms to process data, the construction of intelligent microfluidic platforms resulting from the combination of these two disciplines has received increasing attention[25, 26]. The integration of microfluidics and microalgae research has been steadily developing in the last decade[27-32]. As an illustration, Zheng *et al.*[31] present an integrated microfluidic device designed for marine microalgae culture and chemical toxicity screening. While their research yielded commendable results, the relatively intricate fabrication process of the microfluidic chip, the chemical treatment steps required for microalgae detection, the overall system construction costs, and the expenses associated with consuming the microfluidic chip during system operation collectively render the system challenging for adoption by microalgae researchers. In addition, Wang *et al.*[32] present a microfluidic system for analysing ballast water using a concentration gradient chip. This platform incorporates a photodetection system to assess the chlorophyll properties of the microalgae. While this research marks a valuable contribution to the exploration of the potential of microfluidic systems in microalgae research, it is important to note that the system, designed with considerations for the properties of detection reagents and chlorophyll, does not facilitate direct microalgae-specific classification analysis. Similar to the previously mentioned work, this system also exhibits relatively high complexity and operational costs. Thus, the development of microfluidic platforms dedicated

to microalgae detection remains at an early stage of development. Image-based intelligent microfluidic platforms have the potential to offer a more intuitive observation of microalgae morphology, significantly easing the challenges associated with experiment preparation. Furthermore, the development of an integrated intelligent platform has the potential to lower the barriers for microalgae researchers, making the field of microfluidics more accessible and acceptable within the microalgae research community.

In this work, we develop an automated and intelligent microfluidic platform (AIMP) that can overcome the time-consuming and labour-intensive drawbacks of conventional methods for microalgae detection and monitoring. The platform utilises a USB microscope and a mini *XYZ* motorised platform to reduce an otherwise expensive laboratory microscope to a size and weight that can be carried in a backpack without compromising critical functionality. The AIMP also uses laser-cut microfluidic chips to replace microfabricated microfluidic channels that require complex fabrication processes. Microalgae with four different sizes and morphologies (*Cosmarium*, *Closterium*, *Micrasterias*, and *Haematococcus Pluvialis*) are selected to demonstrate the feasibility of image-based detection on this platform. Datasets are collected for these microalgae and a YOLOv5 detection model is trained based on the datasets. Different image processing methods are chosen for different species for precise classification. Furthermore, we examine the versatility of the AIMP by using it for monitoring the production of astaxanthin from *Haematococcus Pluvialis* microalgae over a long period of 30 days. The platform meets the need for portability by having all mechanical control and data analysing processes performed by a single microcomputer (Raspberry Pi 4B). Finally, an APP is developed to call all the functions to make the platform easy to use.

3.2 Experimental

3.2.1 Materials

Four species of microalgae were obtained, including 1) *Cosmarium*, which is deeply separated in the middle of the cell by a short isthmus containing the nucleus (Carolina Biological Supply Company); 2) *Closterium*, which has a crescent or elongated shape (Carolina Biological); 3) *Micrasterias*, whose size can go up to hundred-microns-level (Carolina Biological); and 4) *Haematococcus Pluvialis*, spherical to ovoid in shape, which can get remarkable colour changes due to the accumulation of astaxanthin (Darwin Biological Company). The USB microscope was purchased from Jiusion Digital Microscope (focusing range: 10–250 mm, we used a 10 mm focusing distance to get the maximum magnification; streaming speed: 30 fps). The *XYZ* motorised stage was made by assembling three miniature electric linear actuators (Nema 17 Stepper Motor with 1.8° step angle). The double-sided adhesive tape was purchased from 3M™ (GPT-020F, thickness of 200 μm), which was cut using a CO_2 laser cutter (OMTech K40 40 W) to make microfluidic channels. The top of the channel was sealed using a 3 mm thick polymethyl methacrylate (PMMA) plate. The AIMP was powered by a rechargeable Li-polymer battery (11.1 V, 3300 mAh, Youme Power). A Raspberry Pi (4, Model B, 4GB RAM) was used as the microcomputer. Table 3.1 lists the names, quantities and costs of the main components used to build the AIMP. Ignoring the price of consumables such as glue, PMMA shells, etc., the total cost of building the AIMP was less than £170.

Table 3.1 Cost for the main components of AIMP

Component	Quantity	Cost in Total (in British Pound)
USB microscope	1	£21.38
Miniature Electric Linear Actuator	3	£64.98
Stepper Motor Driver (DRV8825)	3	£9.99
Raspberry Pi	1	£45.83
Backlight LED Board	1	£2.48
Battery	1	£23.00

3.2.2 Preparation of *Haematococcus Pluvialis* samples

The 30 ml *Haematococcus Pluvialis* sample was shaken with a laboratory shaker (Microspin 12, Grant Instruments) at 150 RPM for 5 minutes to ensure that the cells were evenly distributed without causing overt damage to them. After shaking the sample solution, 5 ml of the sample was taken with a pipettor into a clear culture tube, diluted to 50 ml with Jaworski's medium[33] culturing liquid (Culture Collection of Algae and Protozoa, SAMS Ltd.) and placed in a benchtop shaking incubator (SQ-4020, SciQuip Ltd.) at a constant temperature of 25 °C and a constant shaking speed of 100 RPM. Cultures were exposed to a 12 h/12 h light/dark cycle provided by a fluorescent lamp powered with a digital timer switch (178-5368, RS PRO). The incubation lasted for 6 weeks, with the start of week 2 being *Day 0*, and samples from *Day 0*, *Day 15* and *Day 30* were taken for validation experiments.

3.3 Results and Discussion

3.3.1 Construction of the AIMP

Figure 3.1 shows the internal structural design of the AIMP. An XYZ motorised stage is designed and built based on three miniaturised linear actuators to drive the USB microscope, as shown in Figure 3.1a. The linear actuator contains a stepper motor (with a 1.8° step angle) connected with a 95 mm long thread rod (2 mm per turn). The actuator converts the rotation of the rod into a linear movement. Our design allows the USB microscope to observe all the chambers of the microfluidic chip to capture colour images for subsequent image-based analysis. Each microfluidic chip has four sets of sample detection channels, and each set of channels consists of an inlet, an outlet and an observation grid consisting of nine observation chambers of the same size, as shown in Figure 3.1b. The microfluidic chamber is fabricated by laser cutting a double-sided adhesive tape. One side of the tape adheres to a glass side and the other side bonds to a transparent PMMA board. The PMMA board is also laser cut into the designed structure (with an inlet and outlet).

Details of the microfluidic chip fabrication process and the AIMP operation procedures are given in Figure 3.2. For the fabrication, glass slide (75 mm × 25mm × 3mm) and transparent PMMA board with 3mm thickness are used as upper and bottom layers of the chip to ensure optical clarity, while the double-sided sticky tape with 200 μm thickness, as the middle layer of the chip, is chosen to set up the height of the microfluidic channels. The parameter of microchannel height is determined through experimental trials. Initially, two thinner 3M™ tape (300LSE, thickness of 50 μm; and 93010LE, thickness of 100 μm) were experimented; however, they encountered frequent channel clogging, especially with larger microalgae such as *Micrasterias*. Increasing height to 200 μm balanced reduced clogging and minimal reagent

consumption. The inlet chamber was enlarged to 9.4 × 4 mm to accommodate pipetting with minimal risk of spillage or backflow, given variations in pipette tip diameters. Meanwhile, the outlet chamber was slightly narrower, at 9.4 × 2 mm, to focus the exiting fluid and limit overall reagent use. This arrangement establishes a unidirectional flow path from a spacious inlet to a more compact outlet, effectively guiding the sample through the observation chambers. During early development, a design of a single large observation chamber in the centre of the chip was tested. However, this design caused excessive sample overlap, uneven fluid distribution, and required a larger reagent volume to achieve uniform coverage. It also limited the ability to run comparative tests side-by-side with the same sample. To overcome these issues, a three parallel channel design was adopted, each containing three smaller observation chambers (1.8 × 2.7 mm), interconnected by 400 μm-wide linking channels. Multiple smaller chambers reduce clogging and overlapping events. Additionally, replicating chambers within each side-by-side channel improves experimental robustness, allowing convenient side-by-side comparisons under similar flow conditions.

To prevent the effect of external ambient light sources on the imaging process, the platform's housing, except for the bottom base plate, is made of opaque black PMMA boards. The bottom base plate, which includes a light-transmitting cavity, is 3D printed using polycarbonate filaments. This cavity has a socket for easy and repeated insertion and removal of the microfluidic chip and a socket for placing the backlight LED board.

The dimension of the completed AIMP is 14 × 16 × 28 cm. Such a size allows the platform to be easily fit into an ordinary backpack, making it easy for outdoor microalgae sampling and monitoring. Figure 3.1c illustrates the workflow diagram of the AIMP. After sampling is completed, the collected microalgae are transferred to the microfluidic chip and the chip is inserted into the AIMP. Afterwards, the platform can be controlled *via* an APP for real-time

microscope image acquisition, display, and analysis based on pre-set image processing and ML. All data processing (including the control of the *XYZ* motorised stage) is conducted by a Raspberry Pi 4B microcomputer integrated into the AIMP. The interactive graphical user interface of the APP is displayed by casting the Raspberry Pi desktop to the phone screen *via* VNC (virtual network computing) software (RealVNC, Version 7.0.0).

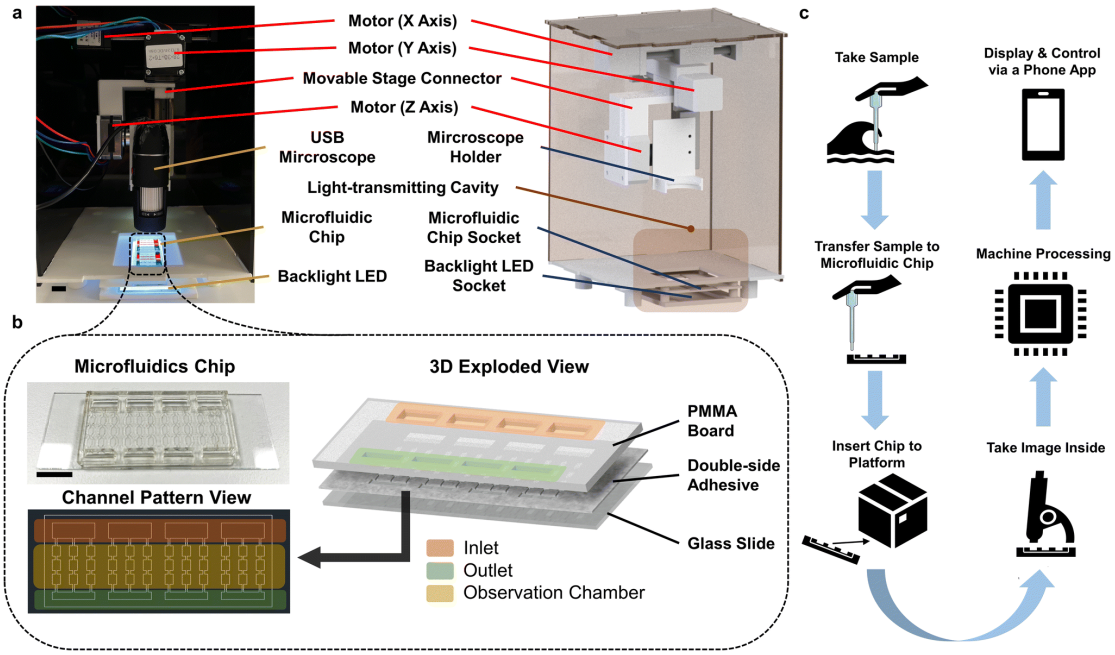

Figure 3.1 Schematic illustration of the AIMP.

a) Actual image and design schematic of the imaging part of the AIMP. b) Schematic representation of the microfluidic chip used to load and observe microalgae. c) Schematic diagram of the workflow of the AIMP. Scare bars are 1 cm.

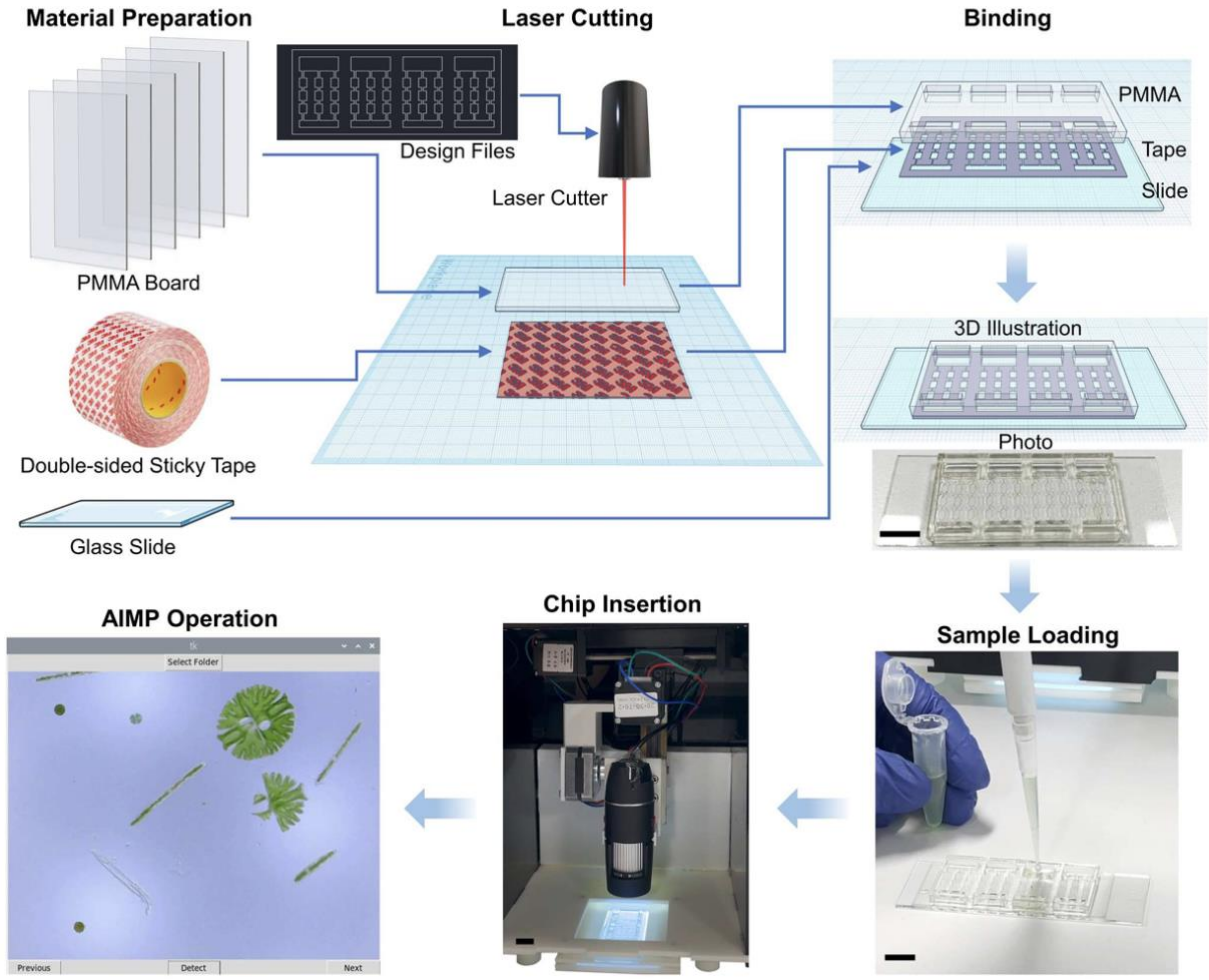

Figure 3.2 Microfluidic chip fabrication process and the AIMP operation procedures. Scale bars are 1 cm.

3.3.2 Dataset preparation and machine learning

As a proof-of-concept demonstration of the AIMP for minimising the human effort involved in the detection of microalgae and reducing the expertise required of the sampler, four species of microalgae, varying in size and morphology, are selected to create the dataset used for the training of the microalgae detection ML network. From an initial set of 812 captured images, we curate 630 labels for *Cosmarium*, 770 for *Closterium*, 737 for *Haematococcus Pluvialis*, and 736 for *Micrasterias*, thus establishing the raw image dataset, as illustrated in the histogram in Figure 3.3. To enhance the dataset's suitability for analysis, we subject it to a series of preprocessing steps, including auto-orientation, resizing to 640 × 640 dimensions, automatic contrast adjustment (contrast stretching), tiling (2 × 2), and filtering to exclude null images, ensuring that at least 90% of images retain annotations after preprocessing.

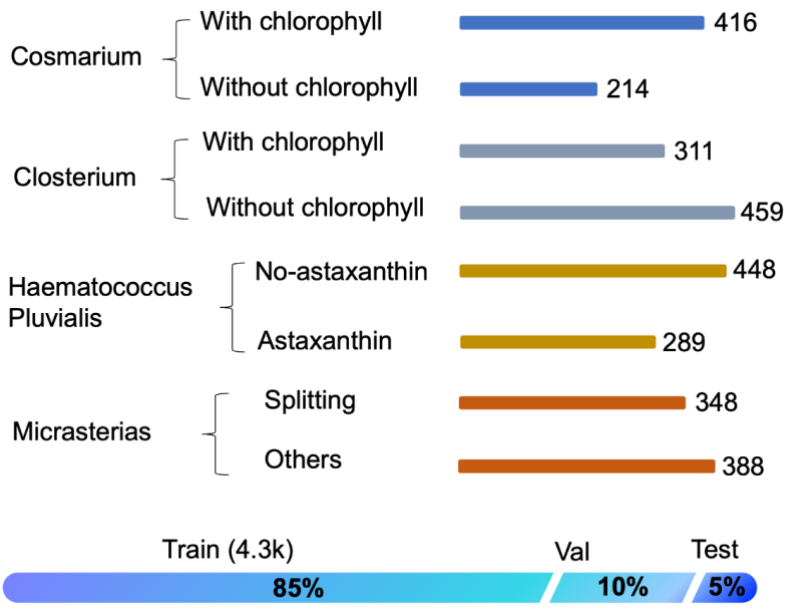

Figure 3.3 Dataset illustration

Size (without data augmentation) and structure (after data augmentation).

Given the relatively modest size of this dataset, we opt to expand it through an image augmentation process. Beyond the conventional flip and rotation augmentations, we introduce additional adjustments such as saturation (ranging from −30% to +30%) and brightness (between −10% and +10%) to compensate for potential variations in lighting conditions during USB microscope imaging. We also incorporate a blur adjustment (up to 1px) to counteract potential imperfections in focus when capturing images, as many microalgae specimens in our case are relatively small. Additionally, a Mosaic augmentation is applied. As depicted in Figure 3.4, during dataset construction, we initiate the process by preprocessing the original images using a 2 × 2 tiling approach, which aids in improving the model's accuracy in detecting smaller microalgae, such as *Cosmarium* and *Haematococcus Pluvialis*. Subsequently, the tiled image set undergoes a Mosaic augmentation to restore the original image size and introduce more background context, thereby enhancing the model's performance. An overall precision improvement of approximately 6% is observed, as demonstrated in the performance comparison graph in Figure 3.4. Upon completion of all data preprocessing and augmentation steps, the final dataset, as illustrated in the bar chart in Figure 3.3a, is divided into three distinct sets: training (85%, comprising 4276 images), validation (10%, with 484 images), and testing (5%, encompassing 243 images).

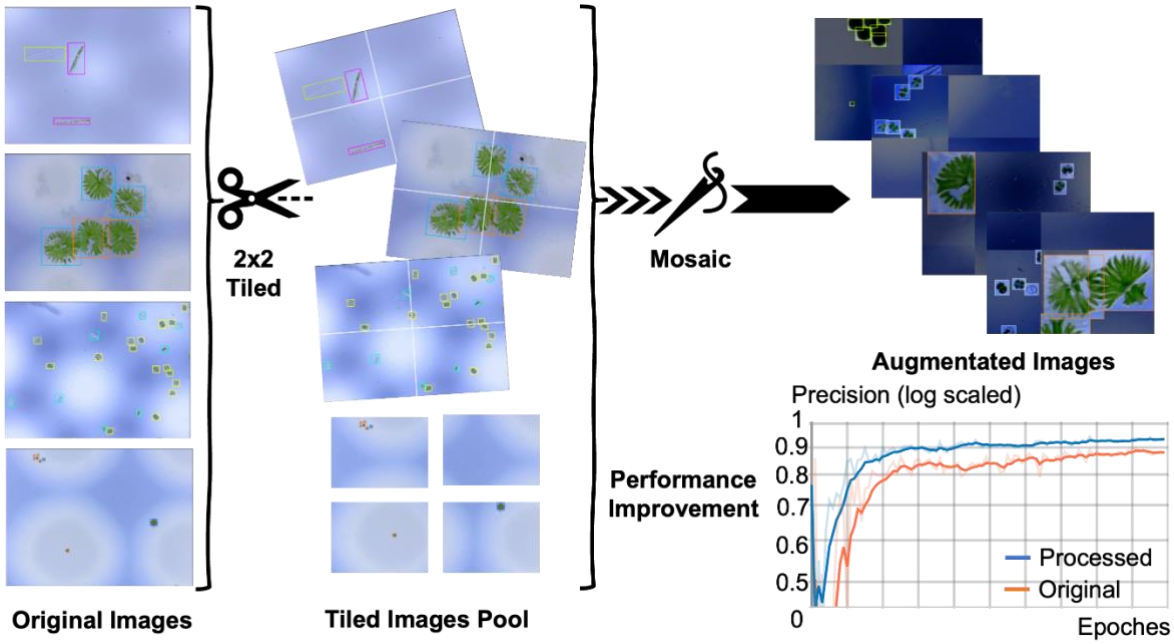

Figure 3.4 Data augmentation process and performance improvement.

Based on the microalgae dataset, we train a microalgae species detection network (MSDN) for 100 epochs with batch size 16 using the YOLOv5 architecture[34]. The training process is monitored, and details can be found in Figure 3.5. It shows the training and validation curves over 100 epochs, tracking three key loss components and key performance metrics. The box loss (box_loss) in the first column reflects the regression error for predicting each bounding box's location and dimensions. The objectness loss (obj_loss) in the second column measures the network's confidence in whether an anchor box truly contains an object. While the classification loss (cls_loss) in the third column assesses how accurately the model assigns a species label to each detected box. All three losses steadily decrease, indicative of the network's improving anchor box spatial alignment and categorisation. Meanwhile, precision, recall, and mean average precision (mAP) rise throughout training, converging near epoch 80. This trend

confirms that the MSDN progressively refines its detection ability, culminating in stable, reliable predictions by the final training stages.

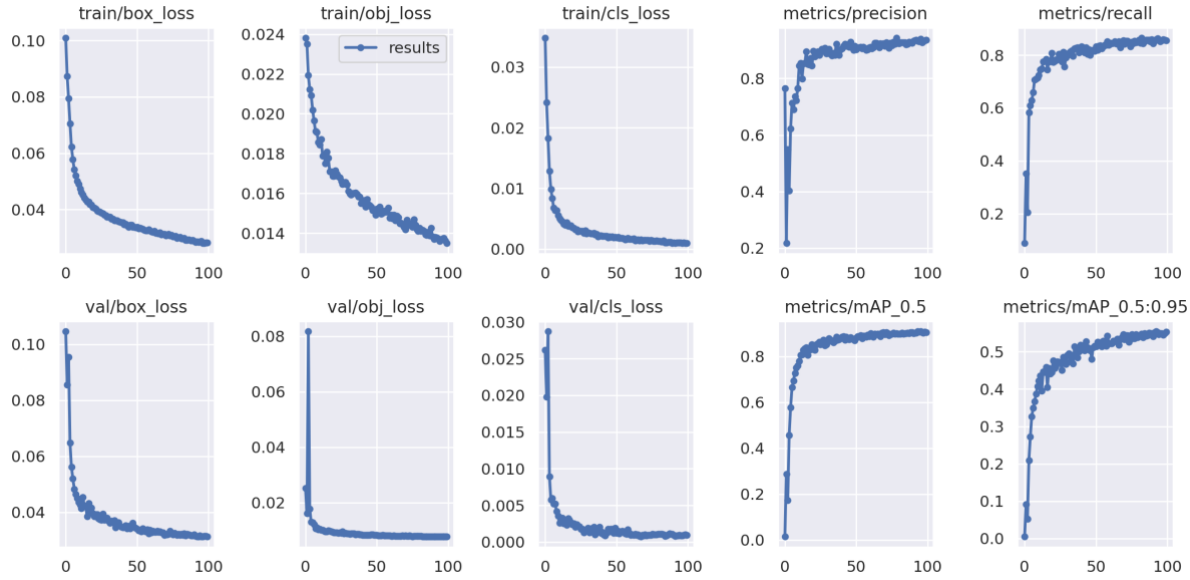

Figure 3.5 Training process

Trained on YOLOv5s, 100 epochs, 16 batch size

The detection results of the trained network on the test image set and its evaluation matrices for each microalgae species are given in Figure 3.6. Since each object in the analysed image may belong to a different class, only true positive (TP), background false negative (FN) and background false positive (FP) are meaningful in the confusion matrix. The precision (TP/(TP + FP)) and recall (TP/(TP + FN)) of the model for each microalgae species are calculated (Figure 3.6). In this figure for sample detection outputs from the YOLOv5-based MSDN, the model achieves 87.0% precision and 94.0% recall for *Cosmarium*, indicating that the network identifies most *Cosmarium* cells while producing few FPs. For *Haematococcus Pluvialis*, 67.1% precision aligns with occasional over-detection of rounded objects, yet 96.0% recall confirms that it instances are rarely missed. *Closterium* obtains 76.0% precision and 79.0%

recall, likely due to its elongated, subtly outlined shape creating moderate confusion in the classifier. Finally, *Micrasterias* stands at 86.7% precision and 91.0% recall, suggesting that its distinctive radial form makes classification relatively straightforward despite occasional misclassifications under partial occlusion or overlapping cells.

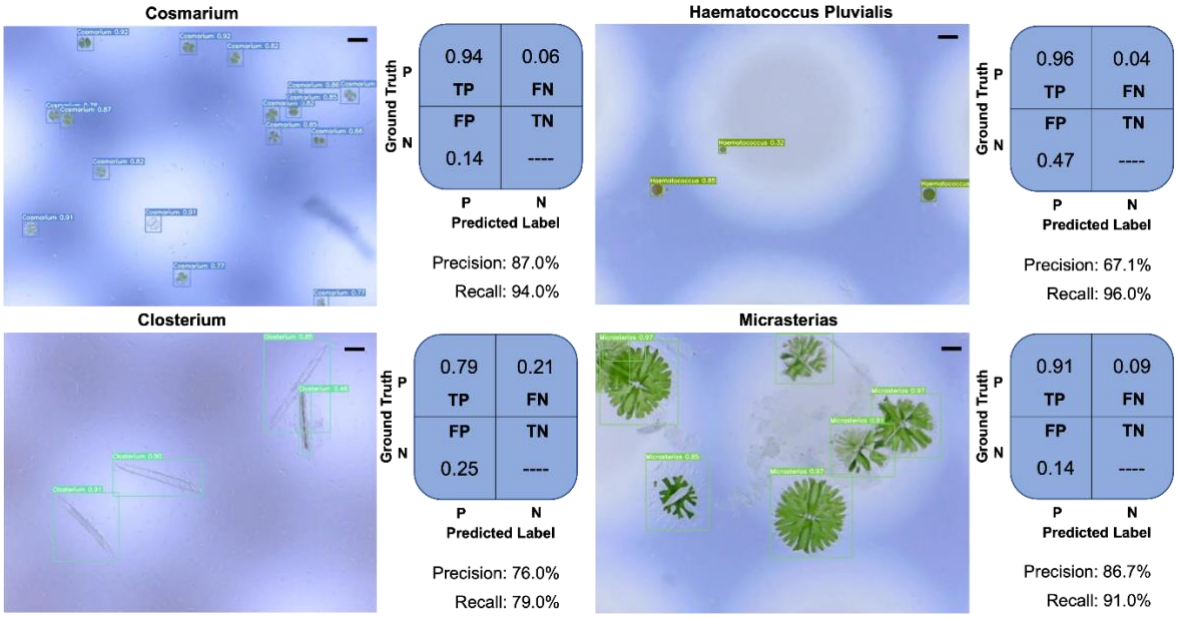

Figure 3.6 Performance of the MSDN

Performance of the object detection network trained on the YOLOv5 architecture for the four microalgae species and presentation of representative sample images after analysis. The images shown for the detection analysis are taken by the AIMP (magnification of 1000×, scale bar = 20 um).

To further evaluate the trained model in an overall sense, we calculated Precision (P), Recall (R) and F1 score using three basic evaluation values, TP, Background FN and Background FP for each microalgae species to be detected, where

$$Precision\ (P) = \frac{TP}{TP + FP} \tag{1}$$

$$Recall\ (R) = \frac{TP}{TP + FN} \tag{2}$$

$$F1 = \frac{2 * P * R}{P + R} \tag{3}$$

Since this is an object detection task, we induced a confidence score for better evaluation. The confidence score (Conf) is associated with each bounding box that the model predicted, which can indicate the model's belief in the presence of the microalgae being detected and its species within the predicted bounding box. With this value induced, the following P vs Conf (Figure 3.7a), R vs Conf (Figure 3.7b) and F1 vs Conf (Figure 3.7c) could be found. These curves were obtained by calculating P, R and F1 values under different confidence scores (from 0 to 1), respectively. The PR curves (Figure 3.7d) are composed of the values of precision and recall plotted at different confidence thresholds for each species.

The average precision (AP) for each category can be derived by calculating the area under the PR curve. The area under the PR curve can usually be obtained using the trapezoidal rule:

$$AP = Area\ Under\ PR\ Curve = \sum_{i=1,2,\ldots,n}^{n} \frac{(R_i - R_{i-1}) * (P_i + P_{i-1})}{2} \tag{4}$$

where n is the number of unique confidence scores, R_i is the R value at the i-th threshold, and P_i is the P value at the i-th threshold. Based on the AP, the mean average precision (mAP) can be derived by using:

$$mAP = \frac{1}{S} * \sum AP \tag{5}$$

where S is the number of species to be detected (in this case, S = 4).

The intersection-over-union (IoU) threshold is also a consideration when evaluating the model. To calculate mAP@k (k is the IoU value), we first consider a prediction as a true positive (TP) only if its IoU with the ground truth bounding box is greater than or equal to k, resulting in

P@k and R@k. The corresponding mAP@k is then derived according to the above process. With the above evaluations, we find the value of mAP@0.5, which is the mean average precision at 0.5 intersection-over-union (IoU) threshold, is 92.8%.

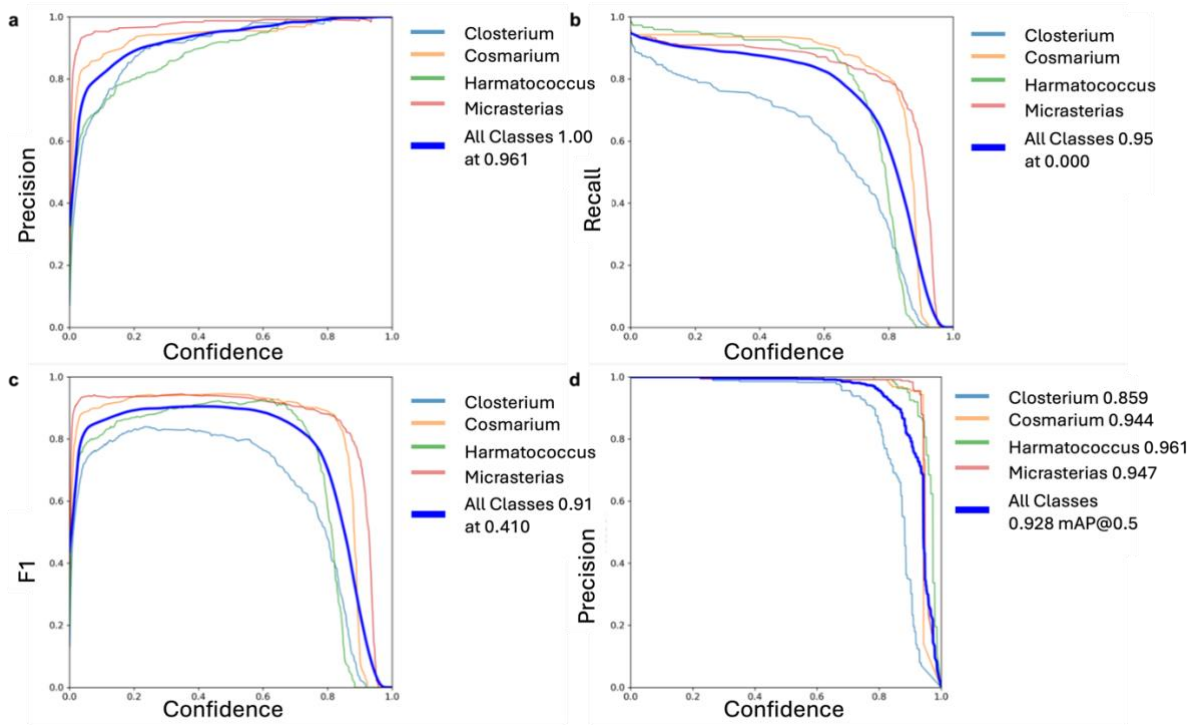

Figure 3.7 Evaluation of the trained microalgae species detection model.

In addition to the YOLOv5 architecture, other YOLO series (YOLOv7, YOLOv8)[34, 35] are used for comparison (Table 4.2). For YOLOv8 we compared architectures with different numbers of parameters (from n, s, m, l, with increasing numbers of parameters in that order). Same as YOLOv5, YOLOv7 and v8 were trained for 100 epochs with a batch size of 16 using the same dataset. As indicated in Table 3.2, they all have a > 90% performance on microalgae detection. As the depth and parameters of the model increase, YOLOv7 and v8 do not show a significant advantage in microalgae detection accuracy. However, deeper model architectures and more parameters clearly make the model run slower. To facilitate comparison, we trained

a *Cosmarium* classifier based on Haar Cascade[36] (see Table 3.2). It is important to note that both training and deploying low-resource-cost models like Haar Cascade offer advantages in terms of reduced computing power requirements. However, it often demands a more extensive dataset to achieve the desired results. In our case, we used the same raw dataset, designating images containing *Cosmarium* as positive samples and the remaining images as negative samples. To create a test set for subsequent model evaluation, we extracted 5% of positive samples and 5% of negative samples from the raw dataset. Considering the typical size of *Cosmarium* in the images, we employed a 20 × 20 window size until reaching an Acceptance Ratio Break Value of 10-6. In comparison to the YOLOv5-based MSDN, which achieved 87.0% precision and 94.0% recall in *Cosmarium* detection, the Haar Cascade Classifier exhibited much poorer performance with 56.2% precision and 40.9% recall trained on the same dataset. For saving computational resources and time, training on the Haar Cascade Classifier for other species of microalgae detection was not performed. This discrepancy is likely attributed to the relatively small dataset size and the relatively uniform background in the microalgae images provided by AIMP. Therefore, to mitigate the data collection costs for individual microalgae species and facilitate the future inclusion of additional microalgae species, we selected YOLOv5 as an example to showcase the capabilities of AIMP.

Table 3.2 Evaluation of the trained microalgae species detection model.

Network Architecture	**Precision**	**Recall**	**F1 Score**	**mAP@0.5**	**Speed (Tesla T4 GPU)**
YOLOv7	0.946	0.842	0.89	0.902	12.3 ms
YOLOv8n	0.937	0.845	0.89	0.921	7.6 ms
YOLO v8s	0.933	0.863	0.90	0.927	11.6 ms
YOLO v8m	0.948	0.843	0.89	0.915	18.9 ms
YOLOv8l	0.932	0.868	0.90	0.920	34.3 ms
Haar Cascade (*Cosmarium* Only)	0.562	0.409	-	-	-

Limited by the field of view (FOV) of the USB microscope at 1000× magnification, the observation chamber of the microfluidic chip cannot be fully covered in a single image taken directly. Therefore, to be able to capture panoramic images of the observation chamber, we integrate an automatic image stitching function in the platform, as detailed in Figure 3.8. The USB microscope first takes images of the upper part of the observation chamber by moving along the x-axis. Then, the microscope moves along the y-axis to take images of the lower part of the chamber. This process is repeated until the acquired images cover the entire observation chamber. By using the stitcher tools in OpenCV, each row of captured images is first parallelly stitched together. The resulting horizontally stitched set of images is rotated 90 degrees and then stitched again using the stitcher tool to complete the raw stitched image. The raw stitched image that covers the whole observation chamber then rotates back to its original orientation. As the raw stitched image has black edges due to non-ideal shifts that occur during the USB microscope movement, we use the pixel indexing method to crop the outermost black edges to

obtain the final stitched image. The microalgae exhibit minimal movement during the process of generating panoramic images, as shown in Movie 4.1.

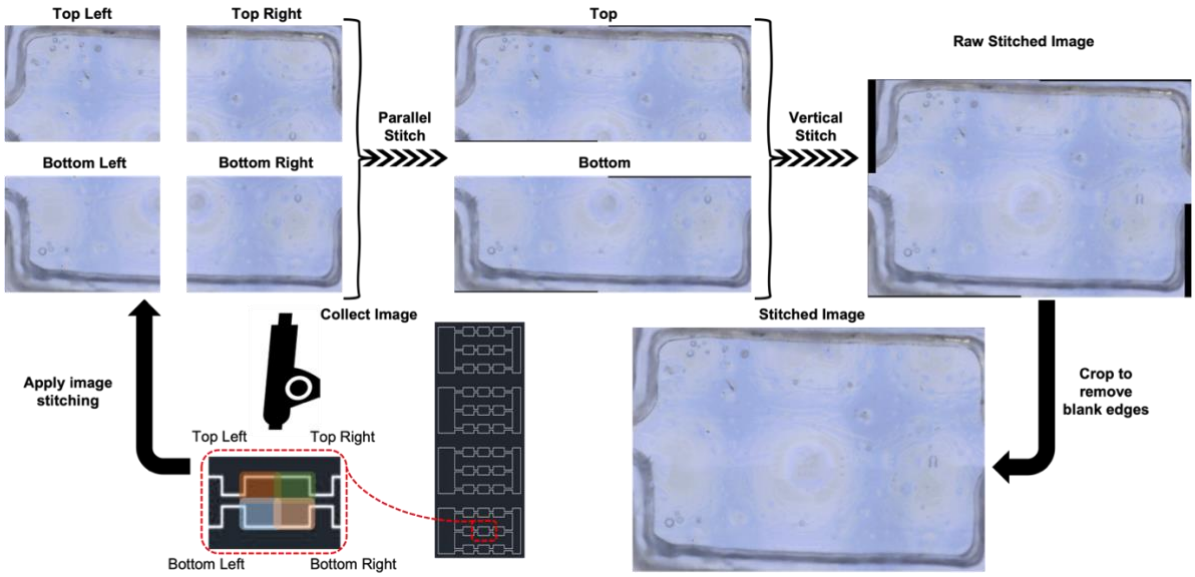

Figure 3.8 Automatic stitching function of the AIMP to recover panoramic image of an individual observation chamber.

To further classify the detected microalgae for monitoring the stage of growth, we validate the use of two different methods – colour extractor for *Cosmarium* and *Haematococcus Pluvialis* (Figure 3.9) and EfficientNet-Lite0 network-based-classifiers for *Closterium* and *Micrasterias* (Figure 3.10). EfficientNet-Lite0 belongs to the EfficientNet-Lite set, which is a set of mobile-end-friendly network models for image classification. The EfficientNet-Lite model architecture has been validated in many application scenarios[37, 38]. *Cosmarium* and *Haematococcus Pluvialis* exhibit pronounced colour changes, green chlorophyll variations or red astaxanthin accumulation respectively, allowing straightforward colour-based image processing tracking with > 95% accuracy, without requiring complex shape analysis. In contrast, *Closterium* cells can appear in V- or W-shaped configurations, rendering

a colour threshold-only classifier unreliable for determining chlorophyll levels for the cell. Instead, the overall morphological cues offer a more robust indicator of internal states (with accuracy >90% by training an EfficientNet-Lite0 classifier). Likewise, in *Micrasterias*, detecting whether a cell is undergoing division hinges on subtle shape differences in its lobed outline, rather than significant shifts in colour intensity. Accordingly, an EfficientNet-Lite0 classifier is employed to capture these nuanced geometric features and achieves 77% accuracy in state discrimination. The reason why this accuracy is lower compared to others is caused by the limitation of dataset size, since the classifier here needs to deal with a more complex cell morphology.

For monitoring the growth of *Cosmarium* via colour extractor, we first crop out the *Cosmarium* cells identified in the image. We then mask the parts that are not in the target colour range by performing a pixel-by-pixel inspection of the HSV (Hue, Saturation, Value) values for each *Cosmarium* cell. By comparing the mask area with the unmasked area within the target colour range, the proportion of chlorophyll contained in *Cosmarium* cells can be derived. As chlorophyll is an important value in microalgae that can be extracted and utilised[39], knowing its proportion in the sample of *Cosmarium* cells can provide a valuable guide for possible subsequent sorting and extraction. A similar colour extractor function is used for identifying *Haematococcus Pluvialis* cells that produce astaxanthin. *Haematococcus Pluvialis* algae are known for their ability to produce astaxanthin, an important nutritional supplement chemical that is widely used in food, feed, nutritional products and pharmaceuticals[40]. Whereas, in this case, we first set green and red as the target colours to obtain the overall area of the cell excluding the background, and then set red only as the target colour to obtain the area of red-coloured astaxanthin accumulated in the cell, which provides an indicator for the possible sorting and extraction.

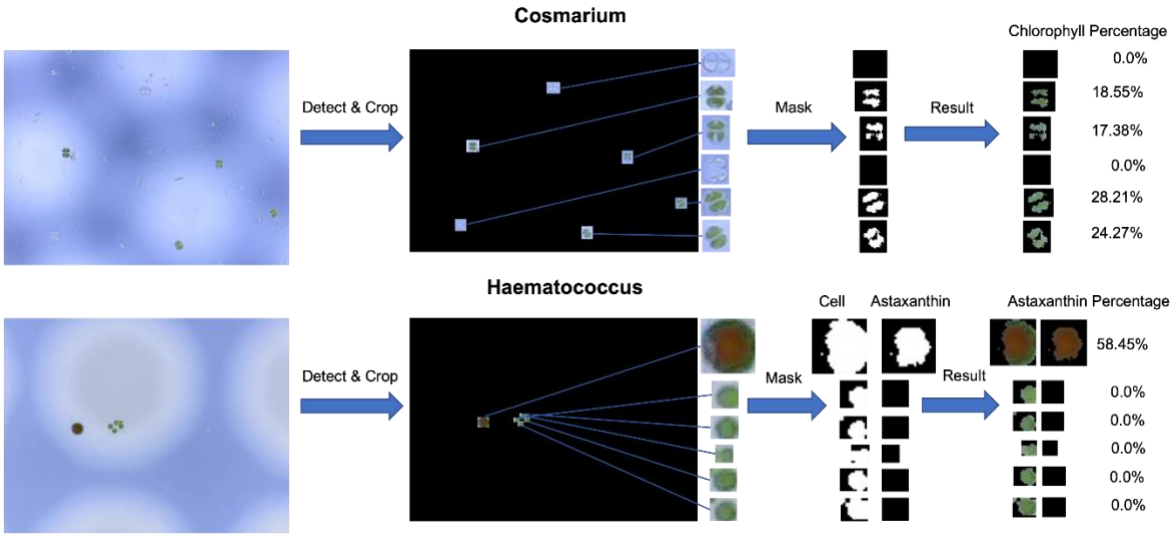

Figure 3.9 Additional functions of the AIMP for monitoring the growth stage of *Cosmarium* and *Haematococcus Pluvialis*.

Further classification of *Cosmarium* and *Haematococcus Pluvialis* detected by the microalgae detection model by a colour extraction function.

Closterium cells, characterised by their crescent or elongated strip-like morphology, present challenges when attempting to establish classification thresholds through chlorophyll occupancy analysis. Consequently, unlike the case of *Cosmarium* cells, we adopt a different approach for *Closterium* cells, segmenting them into two distinct groups: those with visible chlorophyll and those without visible chlorophyll. This division forms the dataset used to train the binary classifier based on the EfficientNet-Lite0 network architecture. This binary classifier achieved a classification accuracy of 93.9% after training (as shown in the image set on the left of Figure 3.10). Also, using the EfficientNet-Lite0 network architecture, we train a binary classifier on the detected *Micrasterias* cells for recognising whether they are in-division,

achieving a classification accuracy of 77.4% (as shown in the image set on the right of Figure 3.10).

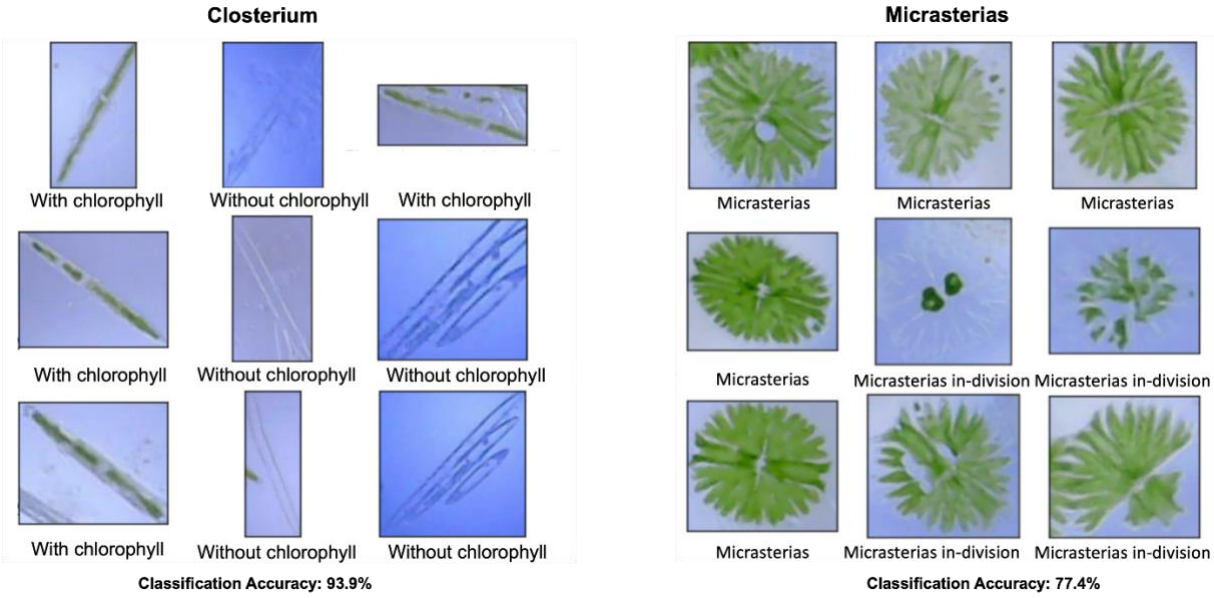

Figure 3.10 Additional functions of the AIMP for monitoring the growth stage of *Closterium* and *Micrasterias*.

Further classification of *Closterium* and *Micrasterias* using two specific trained classifiers based on the EfficientNet-Lite0 architecture.

3.3.3 Raspberry Pi APP development

To make the AIMP more user-friendly, a Raspberry Pi APP is developed to realise the functions of camera live-streaming, *XY* stage controlling, focusing tuning, picture capture, image processing, object detection, and object classification, as illustrated in Figure 3.11. The "Welcome Page" has two selections, one to access the "Camera" page and the other to access the "AI Function" page. The "Camera" page allows the interface for live streaming of the captured video from the USB microscope. The user can adjust the movement in

the *X* and *Y* directions *via* the "*XY* Stage Movement Control" panel in the operator interface, thus allowing the USB microscope to see the entire observation chambers of the microfluidic chip. Furthermore, the speed of movement can be adjusted, allowing for single-chamber observation at small steps and inter-chamber imaging at large steps. The focusing adjustment panel allows the distance between the USB microscope and the microfluidic chip to be adjusted in the *Z*-direction, resulting in in-focus and clear imaging. Similarly, with the "Focusing Speed Set" button, the movement speed in the *Z* direction can be adjusted, allowing coarse and fine adjustments for clear imaging. In the operation interface, the user can capture the currently displayed image (auto-saved in the PhotoWall folder) and invoke the automatic stitching function (auto-saved in the Stitched folder). Since the automatic stitching function is invoked to acquire sub-images from left to right and top to bottom and then stitch them together, before using the "One-step Channel Scanner", the user needs to ensure that the USB microscope's current imaging area is in the upper left of that observation chamber.

When entering the "AI Function" page, the user can select an image folder to access (*e.g.* PhotoWall folder or Stitched folder). When the image is displayed, the user can select to browse the previous and next images in the same folder. The "Detect" button located in the middle serves the purpose of taking the currently displayed image as input for the trained MSDN, which then retrieves information about the microalgae species present in the image along with their respective counts. After conducting MSDN analysis on 50 sample images, we find that, on average, the platform requires approximately 1.974 s per image from the moment the "Detect" button is pressed until the detection result is displayed in a pop-up window. By selecting the specific microalgae species within the pop-up window, the user can access their corresponding classification functions (explained in Figure 3.9 and 3.10). The result for the selected microalgae species after further classification will be displayed, as shown in the

screenshot at the bottom right of Figure 3.8. The full demonstration of the APP for controlling the AIMP for detecting and monitoring microalgae is given in Movie 4.2.

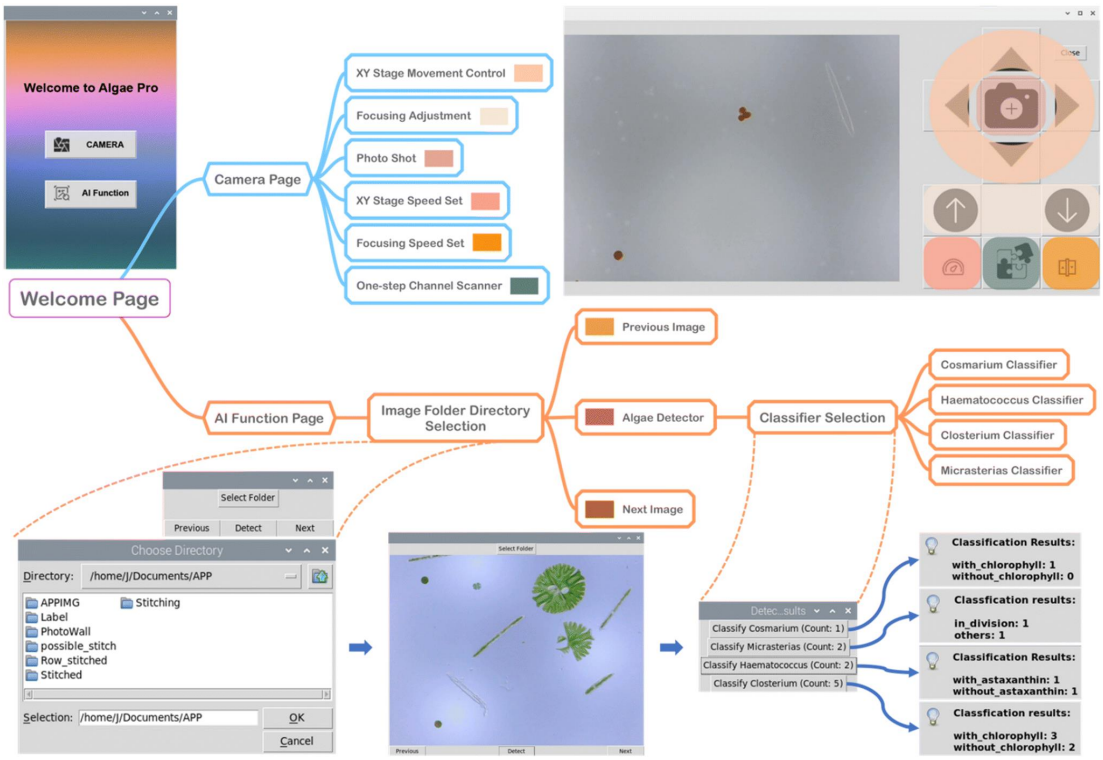

Figure 3.11 Schematic illustration of the Raspberry Pi APP for the AIMP and screenshots on each node.

3.3.4 Monitoring the accumulation of astaxanthin in Haematococcus Pluvialis

To further examine the capability of the AIMP in practical applications, we use it to monitor the accumulation of astaxanthin in *Haematococcus Pluvialis* over a period of 30 days and perform automatic platform-based analysis. Figure 3.12 shows the culture experiment data and comparison graph of the manual (blue columns) and AIMP (orange columns) obtained

statistics. Using equation (6), we compare the two sets of data and conclude that the AIMP achieves 97.5% accuracy of detection (Precicion_*D*) compared to the manual approach.

$$Precision\_D = \frac{\sum_{i=0,15,30}^{3} \frac{Day\_i\_Manual\_Count}{Day\_i\_Auto\_Count}}{3} \times 100\% \quad (6)$$

where Day_*i*_Manual_Count (*i* = 0, 15, 30) represents the number of *Haematococcus Pluvialis* with the accumulation of astaxanthin on *Day 0*, *Day 15* and *Day 30* obtained by manual counting; similarly, Day_*i*_Auto_Count (*i* = 0, 15, 30) represents the same significance obtained by the AIMP. The data points in the grey line at *Day 0*, *Day 15* and *Day 30* show the proportion of *Haematococcus Pluvialis* that aggregates astaxanthin (derived from manual statistics), while the data points in the yellow line represent the same significance derived from the AIMP. Here, the percentage of *Haematococcus Pluvialis* with astaxanthin aggregates is calculated using the following equation:

$$Ratio = \begin{cases} \frac{Cell\_with\_Astaxanthin\_Aggregate\_Manual\_Count}{Manual\_Count}, & if\ Manual\ Count \\ \frac{Cell\_with\_Astaxanthin\_Aggregate\_Auto\_Count}{Auto\_Count}, & if\ Auto\ Count \end{cases} \quad (7)$$

Therefore, the classifier accuracy (Precision_*C*) after considering both the *Haematococcus Pluvialis* detection accuracy and the subsequent dichotomous accuracy can be derived using equation (8). A comparison of these two sets of data shows that the AIMP achieves 96.3% accuracy in further dichotomising based on astaxanthin accumulation detection.

$$Precision\_C = \frac{\sum_{i=0,15,30}^{3} \frac{\left| Ratio_{Manual_{Count}} @ Day_i - Ratio\_Auto\_Count @ Day\_i \right|}{Percentage\_Manual\_Count @ Day\_i}}{3} \quad (8)$$

Figure 3.12b, c and d show example images of a single observation chamber collected using the automatic stitching function of the AIMP at *Day 0*, *Day 15* and *Day 30*, respectively.

The *Haematococcus Pluvialis* microalgae are initially very small (~10 μm) but grow bigger (~70 μm) after 30 days of culture. In our microfluidic chip, the height of the observation chamber is ~150 μm. Therefore, larger microalgae are less likely to overlap within the chamber, as opposed to smaller ones. Hence, when working with relatively small microalgae, we take measures to dilute and agitate them, effectively reducing the occurrence of overlap. Samples used on *Day 0* are diluted twofold and samples used on *Day 15* are triple diluted to reduce the overlap of *Haematococcus Pluvialis* cells. The samples used on *Day 30* are not diluted because *Haematococcus Pluvialis* cells at this time have become larger and less prone to overlap. To mitigate the effect caused by the unavoidable overlapping of microalgae, many images of microalgae with slight overlap are intentionally included in our training dataset, even for the larger ones. This deliberate inclusion helps ensure the model's robustness and ability to handle various scenarios.

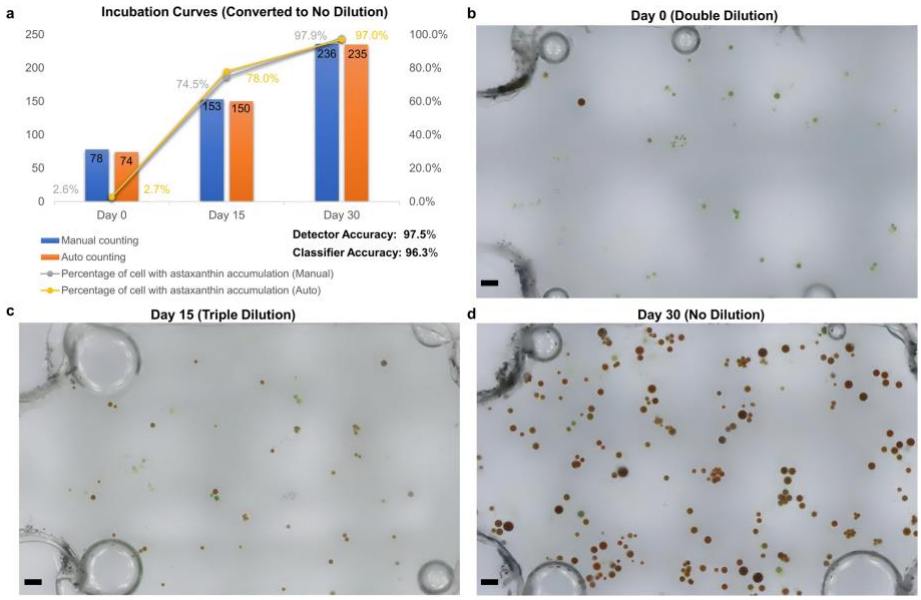

Figure 3.12 Monitoring the accumulation of astaxanthin in Haematococcus Pluvialis.

a) Culture experiment data and comparison graph of manual and AIMP obtained statistics. Example images of a single observation chamber at b) day 0 (samples are diluted twofold before

adding to the chip), c) day 15 (samples are tripled diluted before adding to the chip), and d) day 30 (samples are not diluted). Scale bars are 200 μm.

3.4 Conclusion

In summary, we develop the AIMP to overcome the significant time and labour cost associated with conventional methods for microalgae detection and monitoring. Using a USB microscope and the mini *XYZ* motorised stage, the AIMP achieves the affordability and portability requirements without sacrificing critical functionality. The use of laser-cut microfluidic chips instead of microfabricated microfluidic channels avoids the need for complex manufacturing processes. The capability of the AIMP is validated using four microalgae (*Cosmarium*, *Closterium*, *Micrasterias*, and *Haematococcus Pluvialis*) of varying sizes and morphologies. The MSDN (based on YOLOv5 architecture) trained on the established dataset achieved mAP@0.5 of 92.8%. In addition to MSDN, we use different image processing methods for each microalgae species for precise classification. This precise classification not only helps understand the growth stage of the samples but also serves as an indicator for the potential extraction of valuable cellular products like chlorophyll and astaxanthin. To ensure portability, the AIMP employs a microcomputer (Raspberry Pi 4B) to handle all mechanical control and data analysis processes. Furthermore, the versatility of the AIMP is demonstrated by monitoring the astaxanthin production of *Haematococcus Pluvialis* over 30 days. The AIMP achieved 97.5% accuracy in microalgae species detection and counting, as well as an overall classification accuracy of 96.3%. To enhance user-friendliness, an APP is developed to facilitate easy access to all the functions of the platform. The AIMP has showcased its vast potential as a solution for revolutionising conventional microalgae detection and monitoring methods. Although its performance is currently limited by a relatively small dataset, the AIMP

has the capability to make a transformative impact with the integration of more high-quality data. With continued research and development, the AIMP is poised to drive significant progress in intelligent microfluidics and enable a wide range of innovative applications in environmental science.

3.5 References

[1] A. Singh, P. S. Nigam, and J. D. Murphy, "Mechanism and challenges in commercialisation of algal biofuels," *Bioresource technology,* vol. 102, no. 1, pp. 26-34, 2011.

[2] R. Santoleri, V. Banzon, S. Marullo, E. Napolitano, F. d'Ortenzio, and R. Evans, "Year-to-year variability of the phytoplankton bloom in the southern Adriatic Sea (1998–2000): Sea-viewing Wide Field-of-view Sensor observations and modeling study," *Journal of Geophysical Research: Oceans,* vol. 108, no. C9, 2003, doi: https://doi.org/10.1029/2002JC001636.

[3] F. Gohin, L. Lampert, J.-F. Guillaud, A. Herbland, and E. Nézan, "Satellite and in situ observations of a late winter phytoplankton bloom, in the northern Bay of Biscay," *Continental shelf research,* vol. 23, no. 11-13, pp. 1117-1141, 2003.

[4] A. C. Thomas, D. W. Townsend, and R. Weatherbee, "Satellite-measured phytoplankton variability in the Gulf of Maine," *Continental Shelf Research,* vol. 23, no. 10, pp. 971-989, 2003.

[5] P. R. Hill, A. Kumar, M. Temimi, and D. R. Bull, "HABNet: Machine learning, remote sensing-based detection of harmful algal blooms," *IEEE Journal of Selected Topics in Applied Earth Observations and Remote Sensing,* vol. 13, pp. 3229-3239, 2020.

[6] D. M. Anderson, "Approaches to monitoring, control and management of harmful algal blooms (HABs)," *Ocean & coastal management,* vol. 52, no. 7, pp. 342-347, 2009.

[7] R. C. Cruz, P. Reis Costa, S. Vinga, L. Krippahl, and M. B. Lopes, "A Review of recent machine learning advances for forecasting harmful algal blooms and shellfish contamination," *Journal of Marine Science and Engineering,* vol. 9, no. 3, p. 283, 2021.

[8] S. L. Hinder *et al.*, "Toxic marine microalgae and shellfish poisoning in the British isles: history, review of epidemiology, and future implications," *Environmental Health,* vol. 10, pp. 1-12, 2011.

[9] N. Abdel-Raouf, A. Al-Homaidan, and I. Ibraheem, "Microalgae and wastewater treatment," *Saudi journal of biological sciences,* vol. 19, no. 3, pp. 257-275, 2012.

[10] K. Li *et al.*, "Microalgae-based wastewater treatment for nutrients recovery: A review," *Bioresource technology,* vol. 291, p. 121934, 2019.

[11] S. F. Mohsenpour, S. Hennige, N. Willoughby, A. Adeloye, and T. Gutierrez, "Integrating micro-algae into wastewater treatment: A review," *Science of the Total Environment,* vol. 752, p. 142168, 2021.

[12] M. A. Borowitzka, "Microalgae as sources of pharmaceuticals and other biologically active compounds," *Journal of applied phycology,* vol. 7, pp. 3-15, 1995.

[13] T. Suganya, M. Varman, H. Masjuki, and S. Renganathan, "Macroalgae and microalgae as a potential source for commercial applications along with biofuels production: a biorefinery approach," *Renewable and Sustainable Energy Reviews,* vol. 55, pp. 909-941, 2016.

[14] L. Brennan and P. Owende, "Biofuels from microalgae—a review of technologies for production, processing, and extractions of biofuels and co-products," *Renewable and sustainable energy reviews,* vol. 14, no. 2, pp. 557-577, 2010.

[15] T. M. Mata, A. A. Martins, and N. S. Caetano, "Microalgae for biodiesel production and other applications: a review," *Renewable and sustainable energy reviews,* vol. 14, no. 1, pp. 217-232, 2010.

[16] P. Spolaore, C. Joannis-Cassan, E. Duran, and A. Isambert, "Commercial applications of microalgae," *Journal of bioscience and bioengineering,* vol. 101, no. 2, pp. 87-96, 2006.

[17] F. Liu, C. Zhang, Y. Wang, and G. Chen, "A review of the current and emerging detection methods of marine harmful microalgae," *Science of the Total Environment,* vol. 815, p. 152913, 2022.

[18] P. Otálora, J. Guzmán, F. Acién, M. Berenguel, and A. Reul, "Microalgae classification based on machine learning techniques," *Algal Research,* vol. 55, p. 102256, 2021.

[19] M. Cao, J. Wang, Y. Chen, and Y. Wang, "Detection of microalgae objects based on the Improved YOLOv3 model," *Environmental Science: Processes & Impacts*, vol. 23, no. 10, pp. 1516-1530, 2021.

[20] Abdullah, S. Ali, Z. Khan, A. Hussain, A. Athar, and H.-C. Kim, "Computer vision based deep learning approach for the detection and classification of algae species using microscopic images," *Water*, vol. 14, no. 14, p. 2219, 2022.

[21] Y. Zhang *et al.*, "Microfluidic flow cytometry for blood-based biomarker analysis," *Analyst*, vol. 147, pp. 2895-2917, 2022.

[22] Z. Chen, Z. Pei, X. Zhao, J. Zhang, J. Wei, and N. Hao, "Acoustic microreactors for chemical engineering," *Chemical Engineering Journal*, vol. 433, p. 133258, 2022.

[23] Bayinqiaoge, Y. Zhang, T. Cole, J. Zheng, J. Guo, and S.-Y. Tang, "Recent advances in non-optical microfluidic platforms for bioparticle detection," *Biosensors and Bioelectronics*, vol. 222, p. 114944, 2023.

[24] M. L. Coluccio *et al.*, "Microfluidic platforms for cell cultures and investigations," *Microelectronic Engineering*, vol. 208, pp. 14-28, 2019.

[25] J. Zheng, T. Cole, Y. Zhang, J. Kim, and S.-Y. Tang, "Exploiting machine learning for bestowing intelligence to microfluidics," *Biosensors and Bioelectronics*, vol. 194, p. 113666, 2021.

[26] E. A. Galan, H. Zhao, X. Wang, Q. Dai, W. T. Huck, and S. Ma, "Intelligent microfluidics: The convergence of machine learning and microfluidics in materials science and biomedicine," *Matter*, vol. 3, no. 6, pp. 1893-1922, 2020.

[27] Y. J. Juang and J. S. Chang, "Applications of microfluidics in microalgae biotechnology: A review," *Biotechnology journal*, vol. 11, no. 3, pp. 327-335, 2016.

[28] H. S. Kim, T. P. Devarenne, and A. Han, "Microfluidic systems for microalgal biotechnology: A review," *Algal research*, vol. 30, pp. 149-161, 2018.

[29] B. Ozdalgic, M. Ustun, S. R. Dabbagh, B. Z. Haznedaroglu, A. Kiraz, and S. Tasoglu, "Microfluidics for microalgal biotechnology," *Biotechnology and Bioengineering*, vol. 118, no. 4, pp. 1716-1734, 2021.

[30] A. B. Alias *et al.*, "Microfluidic Microalgae System: A Review," *Molecules,* vol. 27, no. 6, p. 1910, 2022.

[31] G. Zheng, Y. Wang, Z. Wang, W. Zhong, H. Wang, and Y. Li, "An integrated microfluidic device in marine microalgae culture for toxicity screening application," *Marine pollution bulletin,* vol. 72, no. 1, pp. 231-243, 2013.

[32] J. Wang *et al.*, "An integrated microfluidic chip for treatment and detection of microalgae cells," *Algal Research,* vol. 42, p. 101593, 2019.

[33] G. Jaworski, J. Talling, and S. Heaney, "The influence of carbon dioxide-depletion on growth and sinking rate of two planktonic diatoms in culture," *British Phycological Journal,* vol. 16, no. 4, pp. 395-410, 1981.

[34] G. Jocher *et al.*, "ultralytics/yolov5: v7. 0-yolov5 sota realtime instance segmentation," *Zenodo,* 2022.

[35] C.-Y. Wang, A. Bochkovskiy, and H.-Y. M. Liao, "YOLOv7: Trainable bag-of-freebies sets new state-of-the-art for real-time object detectors," in *Proceedings of the IEEE/CVF conference on computer vision and pattern recognition*, 2023, pp. 7464-7475.

[36] S. Soo, "Object detection using Haar-cascade Classifier," *Institute of Computer Science, University of Tartu,* vol. 2, no. 3, pp. 1-12, 2014.

[37] D. H. Fudholi, S. Rani, D. M. Arifin, and M. R. Satyatama, "Deep learning-based mobile tourism recommender system," *Scientific Journal of Informatics,* vol. 8, no. 1, pp. 111-118, 2021.

[38] M. N. Ab Wahab, A. Nazir, A. T. Z. Ren, M. H. M. Noor, M. F. Akbar, and A. S. A. Mohamed, "Efficientnet-lite and hybrid CNN-KNN implementation for facial expression recognition on raspberry pi," *IEEE Access,* vol. 9, pp. 134065-134080, 2021.

[39] A. Hosikian, S. Lim, R. Halim, and M. K. Danquah, "Chlorophyll extraction from microalgae: A review on the process engineering aspects," *International journal of chemical engineering,* vol. 2010, 2010, doi: https://doi.org/10.1155/2010/391632.

[40] R. R. Ambati, P. Siew Moi, S. Ravi, and R. G. Aswathanarayana, "Astaxanthin: Sources, extraction, stability, biological activities and its commercial applications—A review," *Marine drugs,* vol. 12, no. 1, pp. 128-152, 2014.

4 CHAPTER 4: BIOMARKER CONJUGATION ENABLED MICROBEAD PATTERNS FOR INTELLIGENT POINT-OF-CARE BIOSENSING

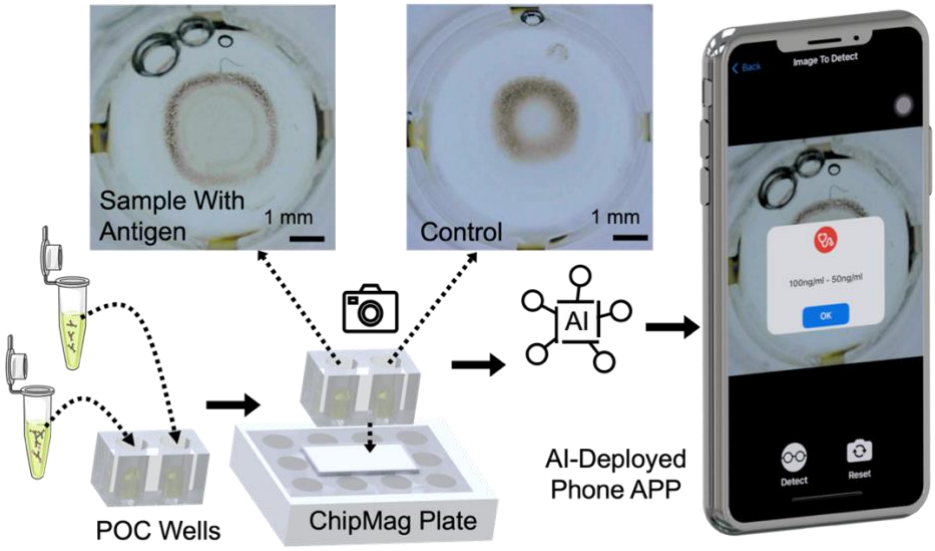

Graphic Table of Contents

Results of this chapter have been submitted: **J. Zheng**, Y. Zhang, Bayinqiaoge, T. Cole, Y. Wang, S.-Y. Tang, and C. Zhang (2024). "Biomarker conjugation enabled microbead patterns for intelligent point-of-care biosensing." submitted for publication

Author Contributions: Conceptualisation: **J. Z.**, C. Z. and S.-Y. T. Data curation: **J. Z.** Formal analysis: **J. Z.** Funding acquisition: C. Z. and S.-Y. T. Investigation: **J. Z.**, , Y. Z., Bayinqiaoge, T. C., Y. W., S.-Y. T. and C. Z. Methodology: **J. Z.** and C. Z. Supervision: Y. W., S.-Y. T. and C. Z. Writing (original draft): **J. Z.** Writing (review and editing): Y. Z., Bayinqiaoge, T. C., Y. W., S.-Y. T. and C. Z.

4.1 Introduction

Cytokines, as crucial mediators in the immune system, orchestrate responses through pro-inflammatory, anti-inflammatory, or context-dependent effects, thus playing a significant role in health[1]. They are mainly secreted by immune cells such as leukocytes, lymphocytes (T cells) and epithelial cells[2]. While cytokines are essential for mounting an effective immune response to eliminate infections, their abnormal or over-increased production can lead to detrimental effects, including serious tissue damage and organ failure[3]. In practice, the imbalance and dysregulation of cytokine production are associated with various diseases and unhealthy conditions. Take the COVID-19 pandemic as an example: it can induce a cytokine storm, a phenomenon where pro-inflammatory cytokines are rapidly and excessively released into the bloodstream, leading to the poor prognosis of severe cases of COVID-19[4, 5]. In addition, for many different diseases, such as intraocular inflammation[6], sepsis[7], asthma[8], cancer[9], and depression[10], the detection and quantitative monitoring of cytokines can provide patients with valuable information about their immune status and can be an important reference for adjusting disease therapies.

The most commonly used cytokine detection methods, such as enzyme-linked immunosorbent assays (ELISA) and polymerase chain reaction (PCR), offer high specificity and sensitivity in biosensing but are limited by long processing times, the need for sophisticated laboratory equipment, and specialised personnel[1]. These constraints make them not suitable for all applications, such as in regions with low availability of laboratory equipment and when patient initial self-determination is required in times of severe stress on the healthcare system. Point-of-care testing (POCT) has the potential to overcome these limitations as it can provide a near real-time, simple and cost-effective diagnosis at or near the patient site, which meets the World Health Organisation's ASSURED criteria (affordable, sensitive, specific, user-friendly, rapid

and stable, device-independent and deliverable to the end user)[11]. Utilising different signal transduction mechanisms, such as optical[12-14] and electrochemical[15-18], various POCT systems have been subjected to wide investigation. Among them, electrochemical-based POCT systems offer high sensitivity in biosensing and good potential for miniaturisation. However, they typically necessitate relatively complex fabrication processes, such as microfabrication[16, 19, 20], which constrains their potential to be widely used as a price-friendly POCT. While optical POCT systems are widely used due to their sensitivity and ease of visualisation, in most cases, they require specialised equipment for quantitative analysis and can be susceptible to interference from complex sample matrices[21].

Lateral flow assays (LFAs), as a type of optical biosensor, have gained prominence during the COVID-19 pandemic for rapid antigen testing[22]. However, when LFAs are utilised as POCT devices independent of centralised testing facilities, a major limitation is that they typically provide only qualitative results, indicating merely the presence or absence of the target analyte. Although the integration of sensors into smartphones and their computational capabilities support the deployment of machine learning models—thereby granting LFAs a certain degree of semi-quantitative analysis in decentralised settings—they remain susceptible to variations in environmental lighting and colour differences in the tested matrices[14, 23]. This is because LFAs usually use colour as the main reading, and cannot make full use of the information collected from the pattern morphology.

Microparticle agglutination immunoassays, often referred to as latex agglutination tests when polymer beads are used as carriers for antibodies, are a type of immunoassay based on morphology information[24]. When using this immunoassay method, latex particles coated with antigen-specific antibodies agglutinate in the presence of antigen, and the degree of agglutination is directly proportional to the antigen concentration. In addition to visual

judgement of the precipitate, quantitative analysis can be performed by measuring transmitted or scattered light[25]. Although these assays are employed for serological testing[26], their reliability on identifying macroscopic or nephelometric signal changes that may be susceptible to 'false positives' caused by non-specific agglutination or variations in environmental lightning conditions. However, the strategy outlined here, exploiting magnetically induced microbead pattern formation, maintains the advantages of bead-based assays, such as rapid (results in ~15 minutes) and simplicity (provide binary positive/negative outputs based on visible clumping) while improving detection specificity through spatial pattern analyses rather than relying solely on turbidity or colour shifts. This approach also addresses key colloidal stability challenges faced by standard latex immunoassays[27] because the magnetic fields can help concentrate or localise beads, thereby minimising non-specific aggregation.

Magnetic beads (MBs) have been employed in immunoassays for more than 30 years, largely popularised by immunomagnetic separation protocols in which MB-bound antibodies efficiently capture and isolate target analytes[28, 29]. Compared to traditional immobilisation on plates or membranes, MBs offer several key benefits, such as simple recovery via magnets rather than centrifugation and more uniform dispersion during incubation, thereby reducing background noise in many assays[30]. Once the beads are separated, they can be detected by straightforward colourimetric[31] or fluorescence measurements[32]. However, combining these MB-based techniques with image-based machine learning to achieve quantitative or semi-quantitative immunoassays offers a good opportunity to fully develop the morphological potential of magnetic bead aggregation.

In this work, enabled by the concentration-related patterns formed by biomarker-conjugated magnetic microbeads, we present an image-based, artificial intelligence-driven point-of-care testing (AID-POCT) platform for cytokine detection. The device utilises magnetic microbeads

coated with polyclonal antibodies to rapidly capture corresponding antigenic proteins in the sample. We exploit that with magnetic field applied, the polyclonal antibody-conjugated magnetic microbeads form distinct patterns with varying concentration of target antigen presented in the test sample. Remarkably, the AID-POCT platform simplifies the biomarker detection process, by reducing the whole detection period to a few minutes. By capturing images of the magnetic bead patterns formed during the assay and feeding them to be analysed by a trained machine learning (ML) classifier running on the mobile phone APP, our device offers a solution for cytokine monitoring without the need for bulky equipment or specialised training. The feasibility of the device is demonstrated by detecting IFN-γ at various concentrations, achieving an overall classification accuracy of 87.2%. Physiologically, IFN-γ levels in human plasma often remain in the low picogram-per-millilitre range (*e.g.*, <50 pg/mL)[33, 34], which would be classified into the 'control' group with our classification model. However, elevated cytokine activity, such as during autoimmune conditions, severe infections, or cytokine storms, can drive IFN-γ concentrations into the high picogram or even nanogram range[35]. Therefore, although the current AID-POCT setup demonstrates the capacity to detect IFN-γ levels extending into the nanogram range, which encompasses extreme inflammatory conditions, this study is best viewed as a proof-of-concept for the underlying MB pattern-based ML-aided immunoassay design. Future efforts may adapt the same platform to target additional biomarkers, such as Fetuin-B and Cluster of Differentiation 14 (CD14), which exhibit clinically relevant ranges and could better highlight the assay's adaptability[36, 37]. Moreover, as this work remains in an early development stage, further optimisation and clinical validation will be necessary before applying the system in routine diagnostic settings.

4.2 Materials and Methods

4.2.1 Preparation of samples

i. Buffer Preparation

A blocking buffer consisting of 1% (w/v) bovine serum albumin (BSA) in phosphate-buffered saline (PBS) was prepared to minimise nonspecific binding and maintain protein stability. Before use, the solution was filtered through a 0.22 μm sterile filter (Millipore) to ensure sterility and remove particulates.

ii. Magnetic Microbeads and Antibody Conjugation

Magnetic microbeads (MB) (Dynabeads™ MyOne™ Streptavidin C1) were used for antibody conjugation. The MB were first washed three times with sterile DI water and then resuspended in 1% BSA in PBS. For the conjugation process (Figure 4.1), the resuspended MB and biotinylated interferon-gamma (IFN-γ) polyclonal antibody (500-P32BT, PeproTech®) were mixed at a mass ratio of 80:1 in a microcentrifuge tube. The mixture was incubated at room temperature for five minutes with gentle rotation at 30 rpm using a tube rotator (Thermo Scientific™) to facilitate binding. Polyclonal antibodies were selected due to their lower cost compared to many monoclonal alternatives. The price of getting per raw image data is an important factor that needs to be considered for data collection when training a data-hungry machine learning model. Also, polyclonal antibodies can bind multiple epitopes on the target antigen[38], potentially enhancing the pattern formation of the magnetic microbeads.

iii. Antigen Capture

The polyclonal antibody-conjugated beads (MB-pAb) were used to capture the target antigen, human IFN-γ recombinant protein (300-02, PeproTech®) (Figure 4.1). The mixture was incubated in a blocked 96-well plate (3599, Corning™ Costar™) or a fabricated polymethyl

methacrylate (PMMA) point-of-care (POC) chip with shaking at room temperature for an additional five minutes to allow antigen–antibody interaction. If the matching antigen is present in the sample, the polyclonal antibodies can bind to different epitopes on the same antigen[38], causing the MB to form a dendritic structure in the solution after incubation. In contrast, when no matching antigen is present, the MB-pAb remain separate.

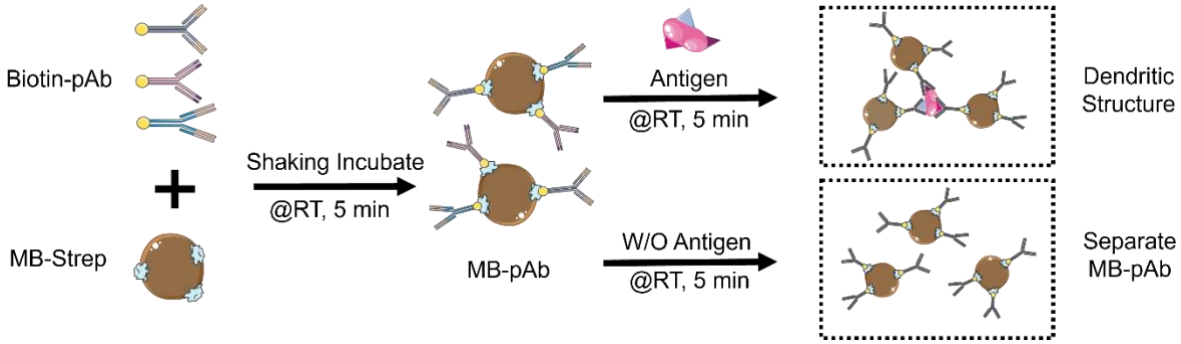

Figure 4.1 Schematic representation of the MBs preparation and antigen capture.

4.2.2 Fabrication of devices

i. Magnetic Plate

For MB manipulation, two types of magnetic plates were prepared. The first was a 96-magnet plate designed for 96-well plates to enable high-throughput image data collection. A magnet holder was 3D-printed using tough polylactic acid (PLA) filament (Ultimaker 3D printer) and crafted to accommodate ninety-six 6 mm × 4 mm N52 neodymium disk magnets (EP657N52, e-Magnets UK). Each magnet was inserted into the holder with the same north pole orientation to ensure a non-distorted magnetic field across the plate. The second magnetic device, called the MagChip, was fabricated following the same protocol as the 96-magnet plate but was designed to hold only twelve magnets. This smaller-scale device offered a more compact alternative for point-of-care (POC) settings.

ii. Lab-based Well Plate Analyse Platform

An image capture platform was assembled to facilitate the imaging of the MB assays (Figure 4.2). The platform consisted of an XY stage, a USB microscope, an LED backlight pad, and a control system. The XY stage was created using two stepper motor linear actuators with sliders that provided a resolution of 0.025 mm per step, allowing precise positioning of samples. A USB microscope (Jiusion Digital Microscope) was mounted above the stage to provide imaging capabilities. To ensure uniform illumination of the samples, an LED backlight pad was placed beneath the sample area. A Raspberry Pi 4B was employed as the microcontroller for motor control, image capture, and communication with a computer.

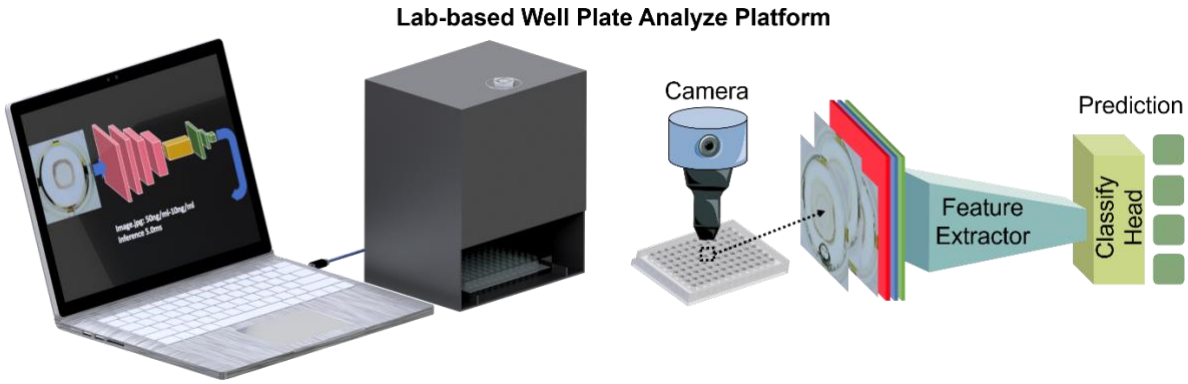

Figure 4.2 Schematic representation of the image capturing and network training in lab.

iii. POC Wells

The POC wells were fabricated to create a functional device for on-site assays with fabrication cost less than £5 per chip. The main chip body was made from a thick polymethyl methacrylate (PMMA) board with a thickness of 10 mm. This board was laser-cut using a Glowforge Pro Laser Cutter 15 (Glowforge Inc.) to form the wells of the chip. An adhesive layer consisting of 3M™ Optically Clear Adhesive (OCA) was also laser-cut to match the design of the main chip body and was attached for bonding purposes. The base of the chip was a thin PMMA board,

2.5 mm in thickness, which was cut to shape and served as the bottom base. This base was adhered to the main chip body using the OCA, ensuring a secure and transparent bond. The chip lid was fabricated by 3D printing using polylactic acid (PLA) filament (Ultimaker 3D printer), providing a precise fit to the chip wells and protection for the chip's contents.

iv. Distinctions from AIMP

Although the same imaging hardware from previous Chapter's AIMP, which is the USB microscope mounted on an XYZ motorised stage, remains in use, the overall fluid handling in this study differs. In previous AIMP research, a laser-cut microchannel structure was designed to support microalgae detection and monitoring, with each chamber and the motorised stage optimised for automated panoramic imaging with stitching. Here, the assay relies on static wells (96-well plates) imaging in lab-based well plate analyse platform that collect images from well to well. In addition, in the proof-of-concept experiment for POC device, this Chapter's work utilises a mobile phone APP with smartphone camera directly, without the need of platform-based imaging for detection.

4.3 Results and Discussion

4.3.1 Workflow

The workflow of the AID-POCT platform for cytokine detection is illustrated in Figure 4.3. The process begins with adding the 90 µl test samples and 90 µl control solutions to 10 µl of the pre-prepared MB-pAb within the POC wells. The mixture is gently shaken at room temperature for 5 minutes to facilitate the binding of target cytokines (antigens) to the antibody-coated MB, ensuring sufficient interaction. After incubation, the POC wells containing the samples are placed onto the magnetic plate and allowed to stand for an additional 5 minutes. The magnetic field induces the aggregation of the magnetic beads, causing them to form visible

patterns at the bottom of the wells. The formation of these patterns is influenced by the concentration of the target cytokines, as antigen–antibody complexes alter the MBs' behaviour under the magnetic field.

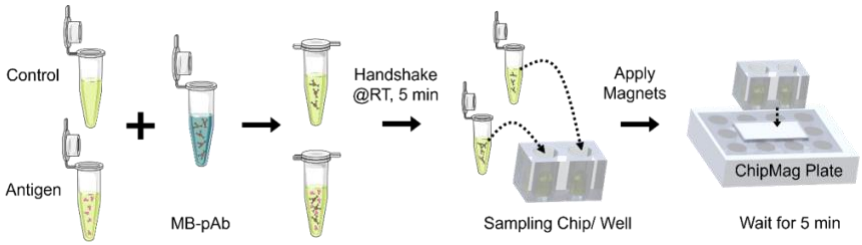

Figure 4.3 Schematic representation of the sample test workflow.

As depicted in Figure 4.4a, a qualitative assessment can be performed by visually comparing the bead patterns in the test samples to those in the control wells. In the presence of the target antigen, the magnetic beads display a distinct pattern different from that of the negative control. This visual differentiation allows for an at-a-glance preliminary indication of whether the sample contains the target cytokine. For quantitative analysis, a mobile APP equipped with a trained ML network is utilised (Figure 4.4b). After users capture images of the bead patterns using the camera on their mobile phones, the APP processes the image to provide a concentration range prediction based on the trained ML model.

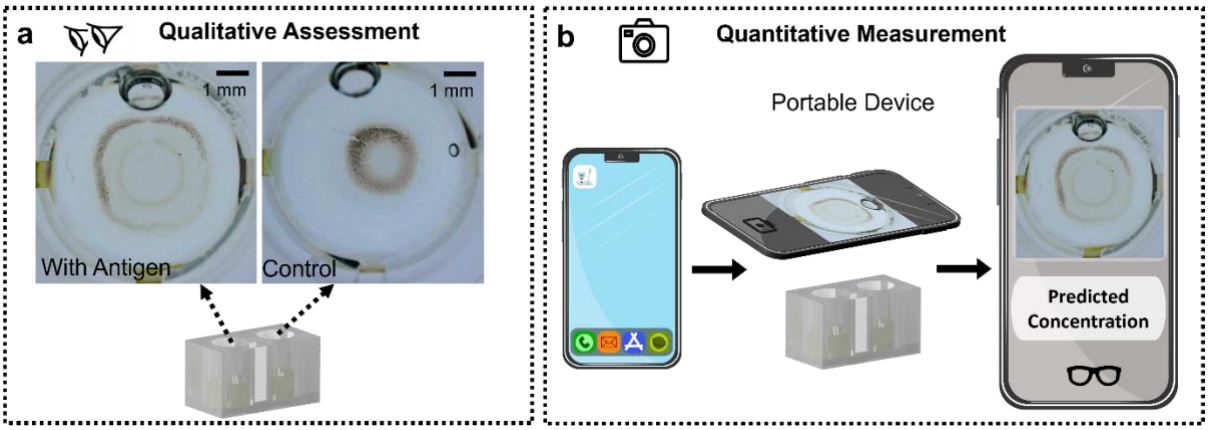

Figure 4.4 Schematic representation of the MB pattern assessment

a) Qualitative assessment of the sample results. b) Quantitative measurement by ML-enabled mobile device.

4.3.2 MB investigation

We investigate to compare two types of MBs to determine the most suitable for our assay: Dynabeads™ MyOne™ Streptavidin C1 (1 μm) and Dynabeads™ M-270 Streptavidin (2.8 μm). Both bead types share the same surface modification (streptavidin) and functionalities (carboxylic acid groups and hydrophilic surfaces) but differ in size. This comparison aims to assess how bead size affects pattern formation. As illustrated in Figure 4.5, at the same bead concentrations, both the 1 μm and 2.8 μm MBs exhibit a similar trend in pattern formation relative to antigen concentration. However, the 1 μm MBs demonstrate greater variability in pattern morphology across different antigen concentrations. We speculate that the larger size of the 2.8 μm beads results in increased momentum (i.e. mass and speed) of the outer beads as they migrate toward the centre under the influence of the magnetic field. This higher momentum may lead to the compression of the central MB network's pattern, thereby diminishing the system's MB pattern formation sensitivity to antigen concentration changes. Based on these observations, we select the 1 μm Dynabeads™ MyOne™ Streptavidin C1 for subsequent experiments. The influence of MB size suggests a potential avenue for further research. Optimising the MB size could enhance the detection capabilities of the system, potentially leading to improved performance in biomarker quantification.

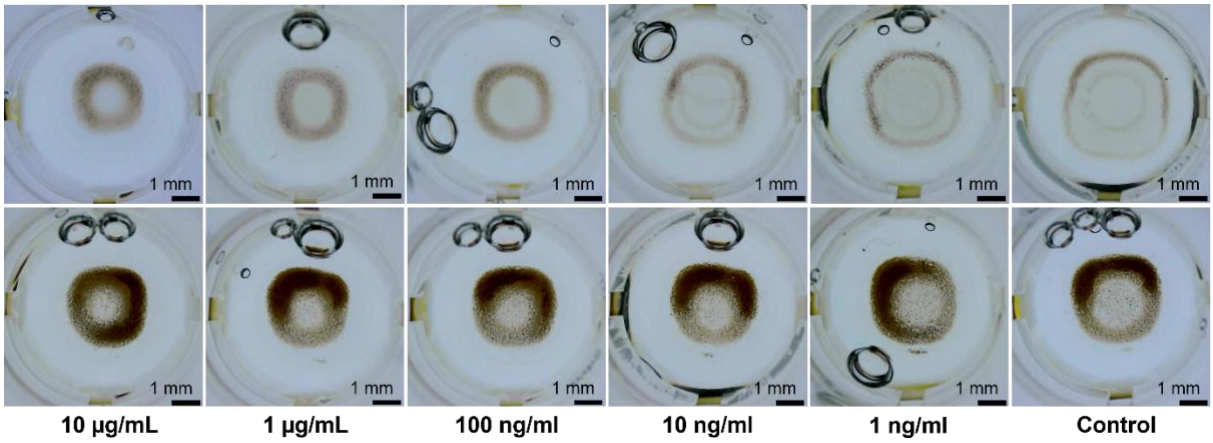

Figure 4.5 Investigation of MBs based on MB size

Comparison of the pattern formed by MB of different sizes with the same beads' concentration (Top: Dynabeads™ MyOne™ Streptavidin C1, 1 µm; Bottom: Dynabeads™ M-270 Streptavidin, 2.8 µm).

Using the selected 1 µm MBs, we explore the optimal mass ratio for incubating the MBs with biotinylated IFN-γ pAb. Following standardised washing and resuspension procedures for MBs of equal mass, we prepare MB-pAb conjugates with varying MB:pAb mass ratios of 200:1, 160:1, 125:1, 80:1, and 50:1. A control sample consisting of MBs without pAb conjugation is also prepared. Each MB-pAb preparation and the control sample are added to a 96-well plate in duplicate. To label the pAb bound to the MBs, we add an appropriate amount of fluorescent secondary antibody (Goat anti-Rabbit IgG (H+L) Cross-Adsorbed Secondary Antibody, Alexa Fluor™ 488, Invitrogen™) to each well. The samples are incubated with shaking to facilitate binding. After incubation, excess fluorescent secondary antibody is removed through washing steps. The fluorescence intensity (FI) of each sample is measured using a microplate reader (CLARIOstar® Plus). The raw FI readings along with their corresponding gain settings are presented in Table 4.1 and a corresponding plot is shown in Figure 4.6. These measurements allow us to quantify the amount of pAb successfully conjugated to the MBs at each incubation

ratio. By analysing the FI data, we identify the optimal incubation mass ratio as 80:1 which provides sufficient antibody conjugation. Due to limited reagent availability at this pilot stage, only two set of replicates was measured and recorded per ratio, serving primarily to validate the overall approach. While standard practice typically includes multiple replicates to improve statistical confidence, these preliminary data effectively guided subsequent design choices. Future studies will incorporate additional measurements to ensure robust experimental reproducibility.

Table 4.1 Fluorescence intensity (FI) readings with varying MB:pAb mass ratio.

Unit (AU)	**Blank Well**	**MB-Only**	**200:1**	**160:1**	**125:1**	**80:1**	**50:1**
Group 1 (Gain:2832)	8849	10877	127797	154278	193571	229492	230780
Group 2 (Gain:2791)	8974	10895	124652	144226	198114	220849	227112

Note: AU stands for Arbitrary Unit

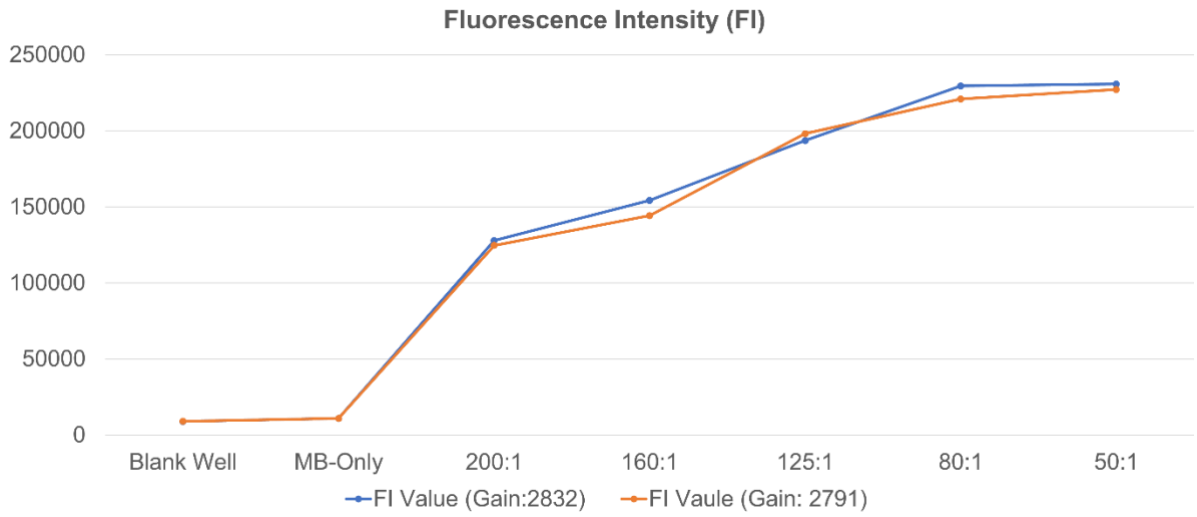

Figure 4.6 Investigation of MBs based on MB:pAb mass ratio

FI plot of MB-pAb conjugates prepared with different MB:pAb mass ratios, including controls without pAb and blank well readings.

4.3.3 Image collection and mechanism analysis

The ML network deployed in the mobile APP is trained using image data collected from the Lab-Based Well Plate Analysis Platform. An exploded view of the platform is shown in Figure 4.7. This platform captures and stores images with a resolution of 640 × 640 pixels of sampled wells in the 96-well plate. (more details are given in the Materials and Methods part). For dataset collection and following validation, the 96-well plate assay based on this platform are conducted. The POC device is only tested for proof-of-concept, which means the assays performed on POC device are directly used the trained ML model based on dataset collected by 96-well plate assays. The dataset is generated by conducting assays with known cytokine concentrations, covering a wide dynamic range (from 1 ng/ml to 10 μg/mL). The collected images are used to train the ML algorithms to recognise patterns corresponding to specific concentrations. As shown in Figure 4.8, the patterns formed by MB vary noticeably with

different antigen concentrations in the test samples, captured using the well plate analysis platform. Both the captured images and the grayscale intensity analyses demonstrate that higher antigen concentrations lead to the formation of larger ring-shaped patterns.

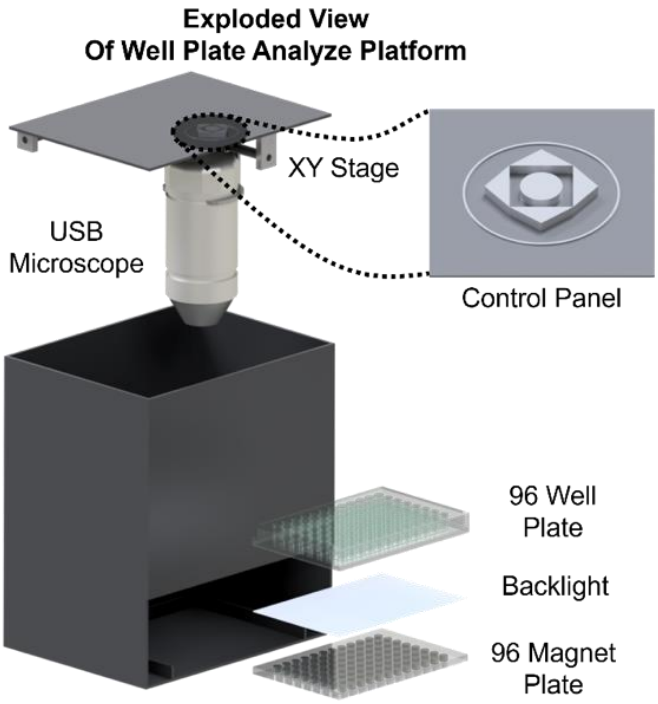

Figure 4.7 Exploded view of the well plate analyse platform.

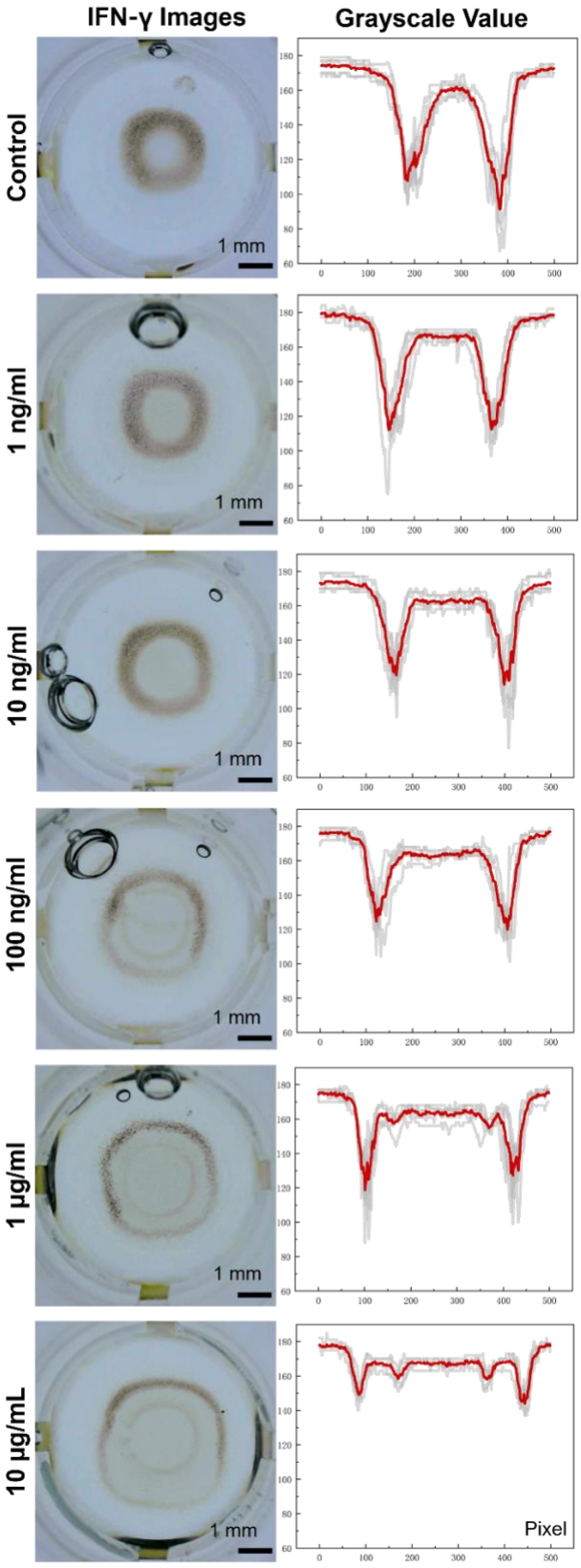

Figure 4.8 MB pattern results with IFN-γ assay.

We further investigate the MB patterns under various conditions using a high-definition inverted microscope, as shown in Figures 4.9, 4.10 and 4.11. For MBs without any conjugated polyclonal antibodies (pAb), these uncoated MBs aggregate into a cluster at the centre of the well upon the application of a magnetic field (Figure 4.9). A closer look at the edges of this cluster reveals that each MB is suspended in the solution without forming obvious chains. We believe that this is due to the fact the surfaces of the uncoated MBs are relatively smooth and lack significant adsorption or repulsion forces. Consequently, the MBs rely primarily on magnetic dipole interactions—mutual attraction induced by the magnetic field—to aggregate, resulting in a simple, centralised cluster pattern.

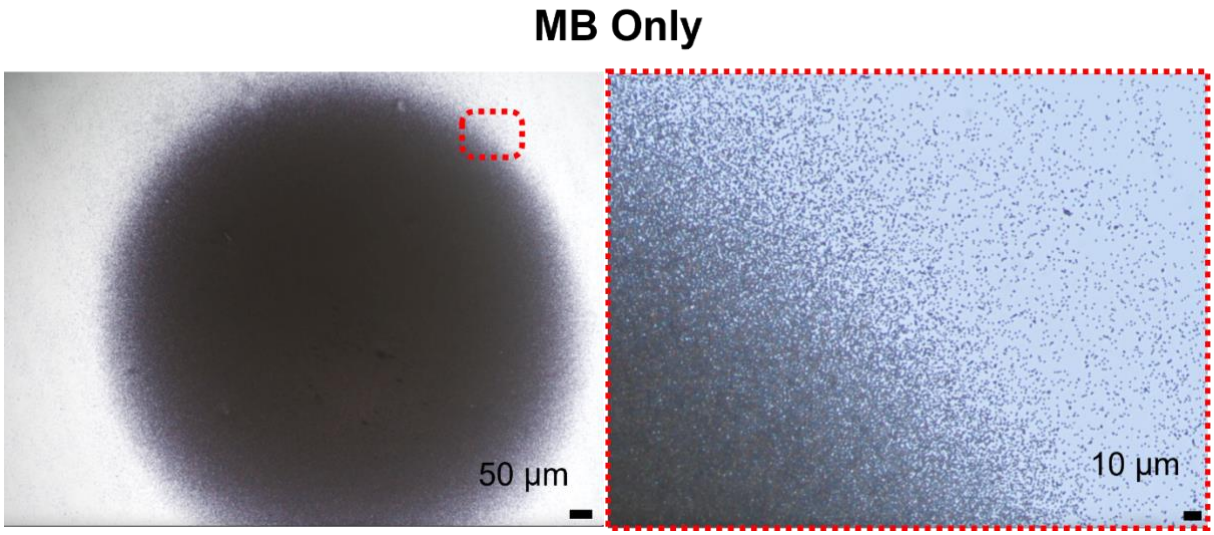

Figure 4.9 Details on MB pattern for MB-only (without pAb coating) with zoom-in for the edge of the dot.

In contrast, when MBs are conjugated with pAb but without the presence of antigen in the sample (Figure 4.10), the aggregation behaviour changes significantly. Antibody molecules are macromolecules with complex spatial structures. Once coated onto the MB surfaces, these antibodies increase hindrance and introduce additional interaction forces. This prevents the

MBs from clustering together as readily as uncoated MBs. Instead, they tend to connect with one another to form long chains (Figure 4.10.i). These chains further develop into a more loosely organised network structure (Figure 4.0.ii). This network structure, originating from the centre, hinders the MB chains at the periphery from moving toward the centre (Figure 4.10.iii). As a result, a ring-like pattern is formed, rather than a central cluster.

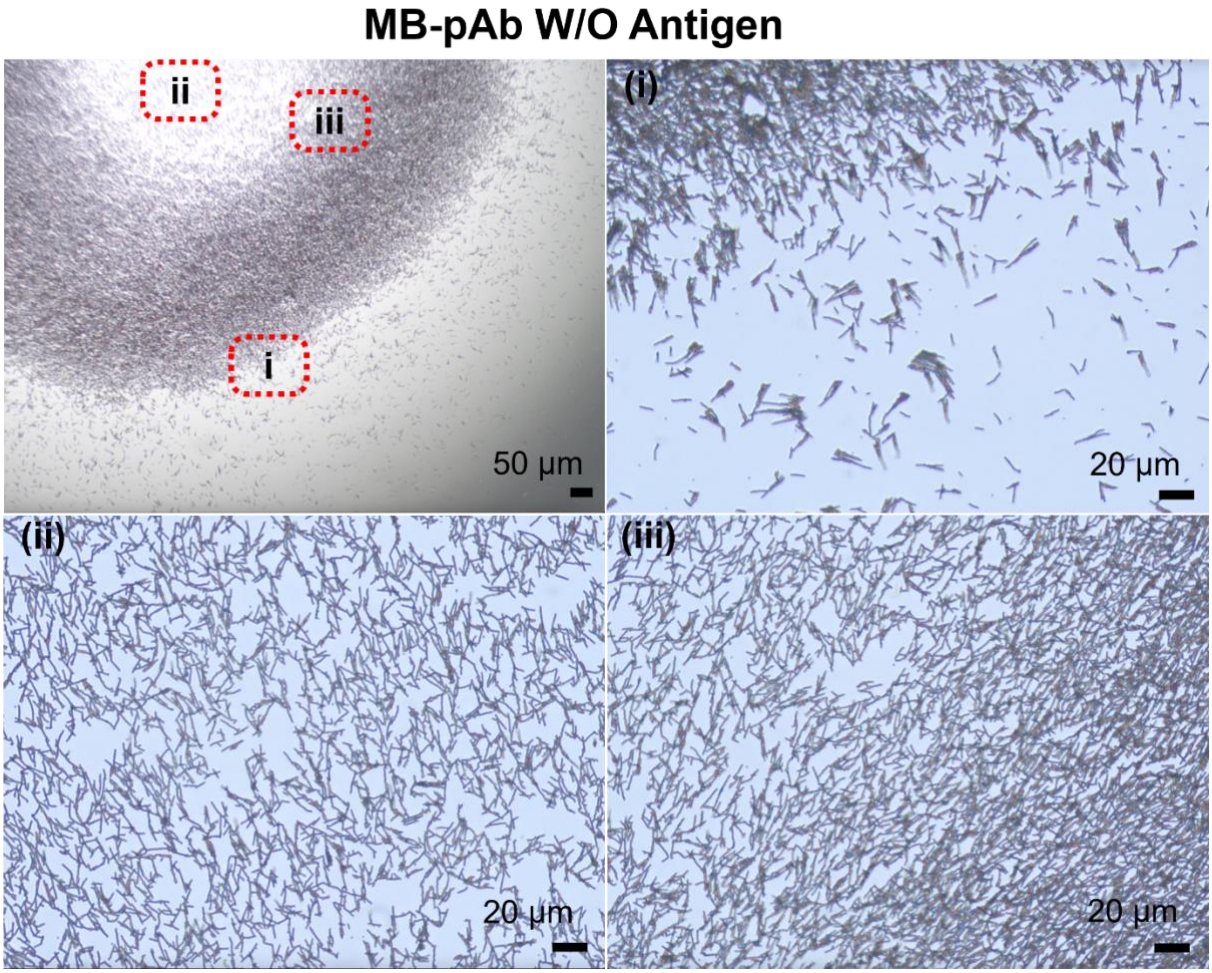

Figure 4.10 Details on MB pattern for negative controls

Zoom in for i. Outer edge of the ring, ii. Inside the ring, iii. Inner edge of the ring.

When the paired antigen is present in the sample, the MB-pAb conjugates form dendritic structures before the application of the magnetic field (as illustrated in Figure 4.1). This pre-

aggregation occurs because the antigens bind to the antibodies on the MB surfaces, promoting cross-linking between beads. We observe relatively shorter chains forming at locations farther from the centre of the well compared to the scenario without antigen (Figure 4.10.i and 4.11.i). Upon application of a magnetic field, a complex network structure of shorter chains forms rapidly from the centre outward, with a looser arrangement. This structure is sufficient to prevent the MBs at the periphery of the well from moving toward the centre (Figure 4.11.ii and Figure 4.11.iii). This leads to the formation of a larger ring-like pattern. At higher antigen concentrations, an increased number of short-chain structures form before the application of the magnetic field. When these MBs in the outer regions cannot continue moving inward, they begin to form additional network structures, which in turn prevent more peripheral MBs from approaching the centre, causing a dual-ring pattern. These dynamic processes are vividly captured in Movie 5.1, which provides a visual demonstration of the phenomenon.

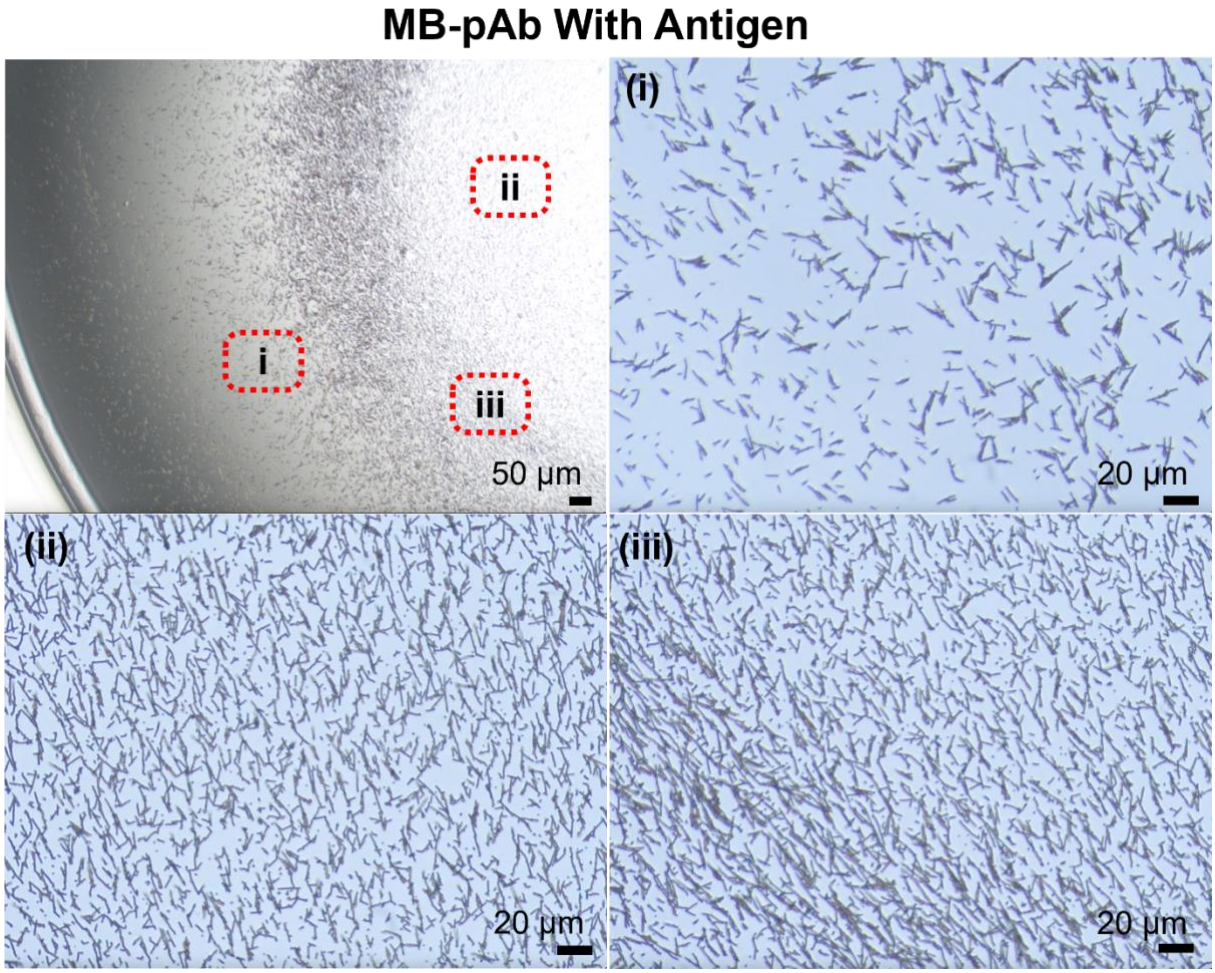

Figure 4.11 Details on MB pattern for positive samples

Zoom in for i. Outer edge of the ring, ii. Inside the ring, iii. Inner edge of the ring.

4.3.4 MB patterns

Our cytokine detection system primarily utilises MB coated with IFN-γ pAb. To evaluate the biosensing specificity and potential for multiplexing of our assay, we conduct experiments using both IFN-γ pAb and, for comparison, tumour necrosis factor-alpha polyclonal antibody (TNF-α pAb).

In Figure 4.12, MBs coated with IFN-γ pAb are used to detect varying concentrations of IFN-γ antigen in the samples. Two replicates are performed to assess the repeatability of the assay. The consistent patterns observed across replicates confirm the reliability and reproducibility of our detection method for IFN-γ. As the concentration of IFN-γ antigen increases, the MB patterns exhibit a clear trend of forming larger ring-shaped structures. To evaluate the biosensing specificity of our detection system, we conduct a cross-reactivity test. MB coated with IFN-γ pAb are exposed to samples containing varying concentrations of TNF-α antigen (Figure 4.13). The MB patterns show no significant changes across different TNF-α concentrations, indicating the MB-pAb conjugates specifically bind to their target antigen (IFN-γ). To demonstrate the adaptability and potential for multiplexing of our detection system, we prepare MBs coated with TNF-α pAb and use them to detect TNF-α antigen concentrations in the samples (Figure 4.14). The MB patterns corresponded well with the TNF-α antigen levels, indicating that by changing the antibody conjugated to the MB, the system can be effectively adapted to detect different cytokines. This verifies that our detection platform can be migrated to other antigen-antibody pairs beyond IFN-γ.

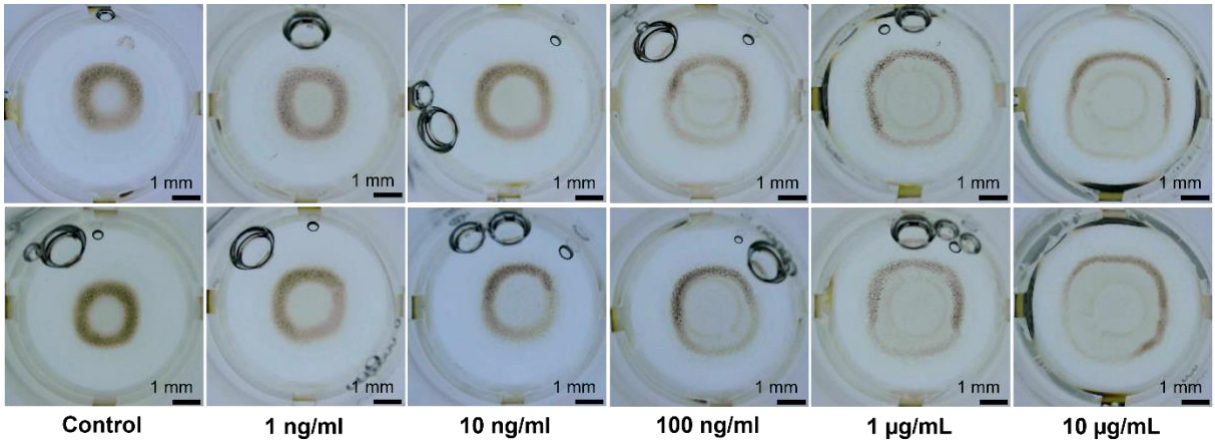

Figure 4.12 MB patterns for IFN-γ

MB coated with IFN-γ pAb detecting IFN-γ antigen concentrations in samples. Two replicates were conducted to verify assay repeatability.

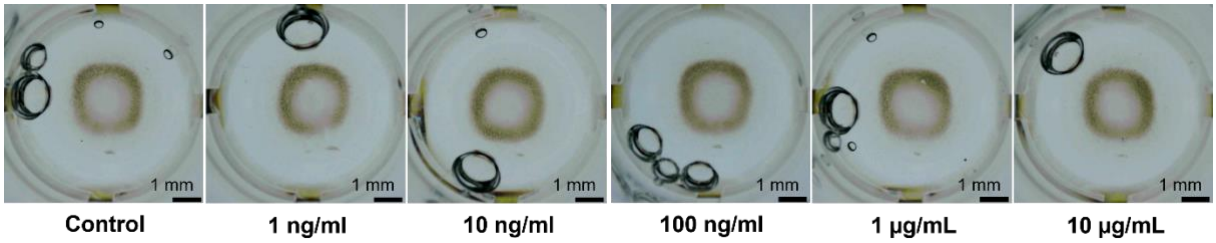

Figure 4.13 MB-IFN-γ biosensing specificity

MB coated with IFN-γ pAb exposed to TNF-α antigen concentrations in samples, demonstrating the biosensing specificity of the detection.

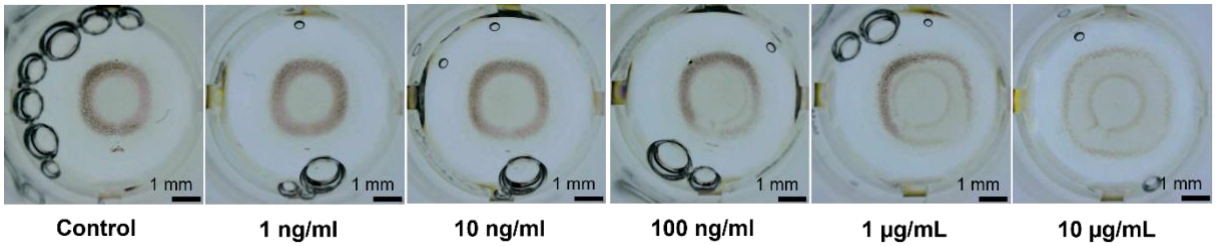

Figure 4.14 MB patterns for TNF-α

MB coated with TNF-α pAb detecting TNF-α antigen concentrations in samples, verifying that the detection system can be adapted to other antigen-antibody pairs.

To evaluate the performance of our cytokine detection system in a more physiologically relevant environment, we replace the standard working buffer (1% BSA in PBS) with 10% human serum (Normal Human Serum, Invitrogen, Thermo Scientific™) in PBS (HS-PBS).

This modification aims to assess the assay's applicability for detecting IFN-γ directly in human serum, which contains various proteins and biomolecules that could potentially interfere with the assay. All testing samples contain 100 ng/mL of IFN-γ antigen. When the working buffer is replaced with HS-PBS, the MB patterns become less distinct compared to the one observed with the standard working buffer, as shown in Figure 4.15. The reduced clarity and definition of the patterns are likely due to nonspecific interactions and increased background noise caused by complex serum components, which can affect the purposed antigen–antibody binding[39] and thus change the aggregation behaviour of the MBs. To optimise the assay performance in the presence of serum, we introduce Tween-20[40], a non-ionic surfactant known for its ability to reduce nonspecific binding and improve assay specificity. Tween-20 is added to the HS-PBS at concentrations of 0.5%, 1%, and 5%. The inclusion of 1% Tween-20 notably improved the MB pattern clarity, yielding results comparable to those obtained with the standard working buffer. However, despite the enhancements achieved with 1% Tween-20, the assay's performance in human serum is still not as optimal as in the working buffer alone. This matrices effect is a common challenge faced by many biosensors when transitioning from ideal buffer conditions to complex biological matrices like serum[41]. Factors such as the high protein content, presence of interfering substances, and variable viscosity in serum can hinder the sensitivity and specificity in biosensing of our detection system. This preliminary finding indicates that while our detection method shows promise for use with human serum samples, further optimisation is necessary. Adjustments could include fine-tuning the concentration of Tween-20 or other surfactants, incorporating additional blocking agents, or modifying incubation times to enhance biosensing specificity and reduce background interference.

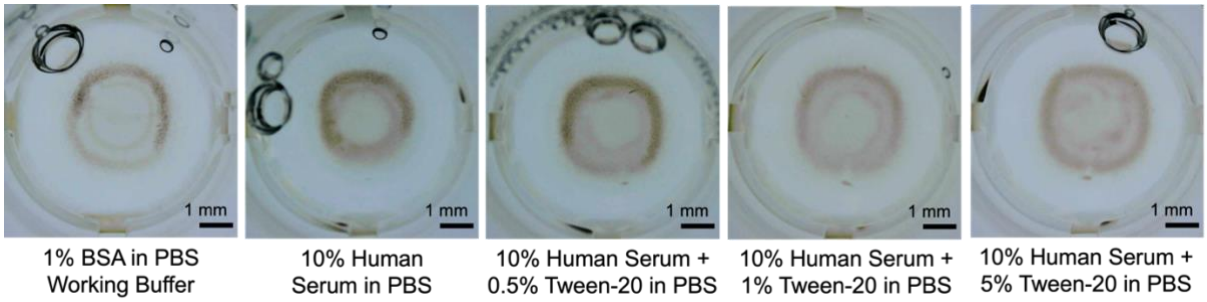

Figure 4.15 MB pattern results under different buffer conditions

For detecting IFN-γ at 100 ng/mL.

4.3.5 YOLO-based classification network

In this work, a YOLO (You Only Look Once) network is employed to perform image classification for IFN-γ concentration detection. YOLO is a state-of-the-art, real-time network that has revolutionised the field due to its ability to achieve high accuracy and speed simultaneously[42]. The architecture of YOLO for classification, shown in Figure 4.16, consists of a feature extractor as its backbone and a classification head for making class predictions based on the input image features. A detailed block diagram of the network can be found in Figure 4.17.

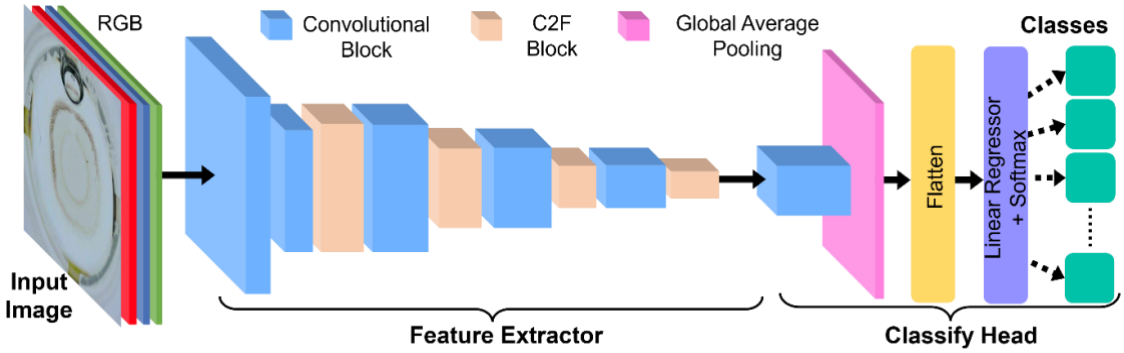

Figure 4.16 Schematic representation of YOLO-based classification network structure.

Figure 4.17 illustrates the architecture of the YOLOv8 network, highlighting the key components: the feature extractor and the classify head. The network incorporates several types of blocks, such as convolutional blocks, bottleneck blocks, and C2f blocks, as explained in the figure. These blocks work together to process the input images and generate predictions of cytokine concentrations.

The feature extractor processes the input images to extract salient features that are indicative of different cytokine concentrations. It employs a series of convolutional blocks and C2f blocks to capture visual patterns. The classify head, as the follow-up, maps the complex features to specific output classes corresponding to various concentration levels based on the features extracted. The three important blocks for building the YOLO network are also illustrated in Figure 4.17. The Convolutional block, as the fundamental building block of the network, consists of a convolutional layer followed by an activation function (SiLU in this case). These blocks detect local features in the input images, such as edges, textures, and shapes formed by the MB. Bottleneck block is largely used in C2f block, which fuses features from earlier and later layers, allowing the network to consider both shallow features and deep features simultaneously.

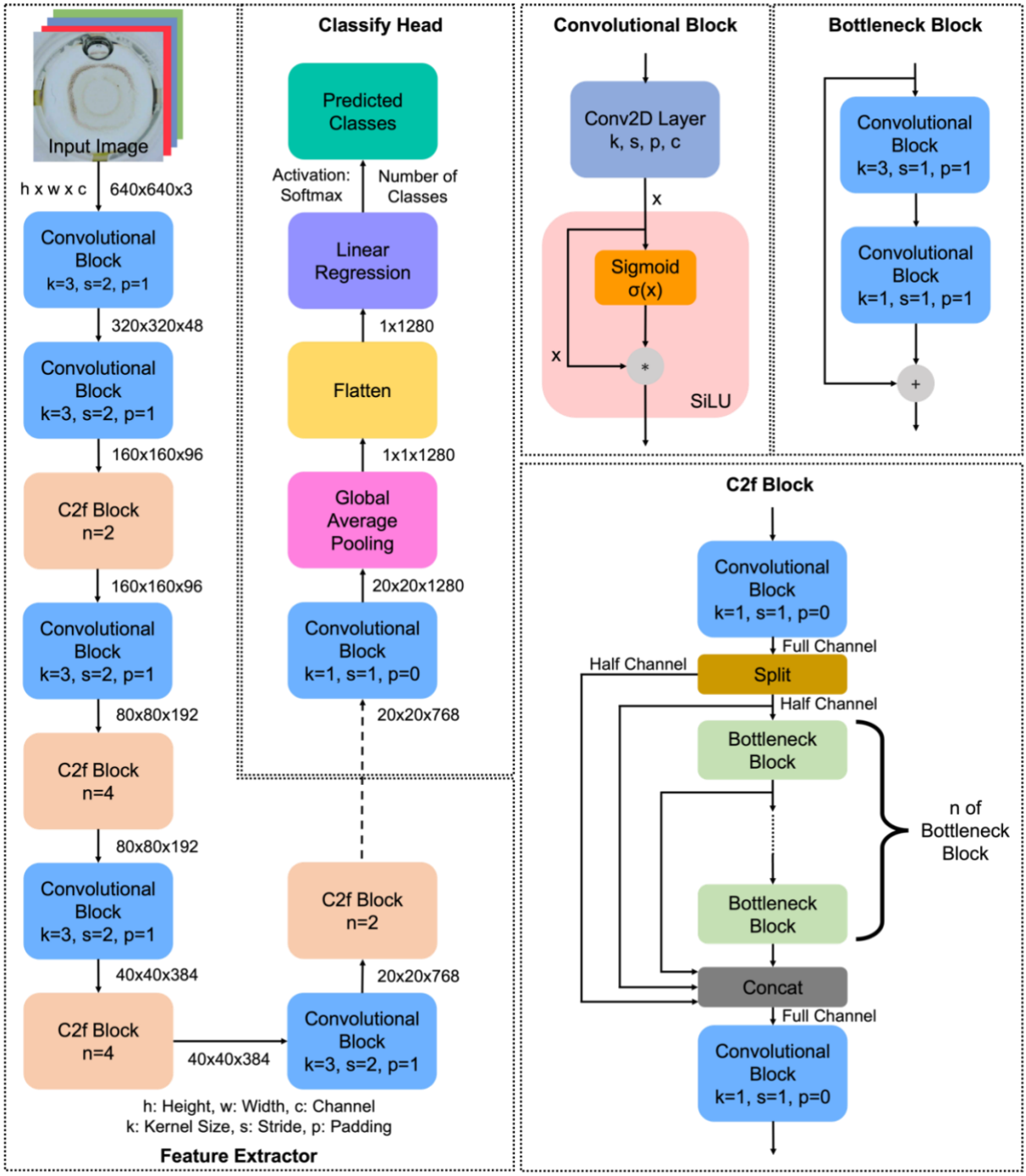

Figure 4.17 Schematic representation of the YOLOv8 network used for MB pattern analysis. The diagram illustrates the flow from input RGB image (640×640×3) through the feature extractor—comprising convolutional, bottleneck, and C2f blocks—to the classify head that outputs the cytokine concentration level prediction.

To train the YOLO network, we prepare a dataset consisting of approximately 40 raw images for each level of IFN-γ concentration to ensure class balance. Several augmentation techniques, including flipping (horizontally and vertically), rotation (-30° to +30°), brightness and contrast adjustment (-20% to +20%), and blurring (up to 3 pixels), are applied to enhance the dataset and prevent overfitting. These augmentations increase the dataset size by five times, resulting in a more diverse and robust dataset. The dataset is then split into 70% for training set and 20% for validating set during training. The rest of 10% image data is used as testing set, which would be combined to the previous validating set to form a new validation for model evaluation after training.

With the trained YOLO network, our AID-POCT device allows near-instantaneous analysis of MB patterns, which enhances its usability as a POCT device. In addition, the modular structure of YOLO facilitates adjustment and expansion. By expanding or updating the training dataset and modifying the output categories, if necessary, the network can be fine-tuned or retrained to further improve prediction accuracy with a larger dataset on the same cytokine or to detect other cytokines.

The performance of the trained network is evaluated using a confusion matrix, shown in Figure 4.18. Each row of the matrix represents the actual class label for the image, while each column represents the predicted class. The diagonal elements of the matrix indicate correct classifications, where the predicted class matches the actual class, representing the accuracy for each class. In contrast, the off-diagonal elements represent misclassifications. Although misclassifications occur, especially between neighbouring concentration levels, when classes are split based on the logarithm (base 10) of concentrations, the model performs relatively well, with all classes achieving over 80% ML classification accuracy. The trained network achieves an average accuracy (i.e. Σ Accuracy for each class/Total number of classes) of 87.2% with a

14.8 ms inference time tested on iPhone 15 Pro. Additionally, the model achieves a macro-averaged precision of 85.5% and a macro-averaged recall of 86.4%. The model trained with early-stop at ~78 epochs to prevent from overfitting. However, the control class attains 100% ML classification accuracy. This shows clear differentiation of samples lacking antigen but meanwhile indicates that the current version of model is still data hungry, thus likely facing overfitting if keep training for more epochs. The performance of current ML model is primarily limited by the dataset size.

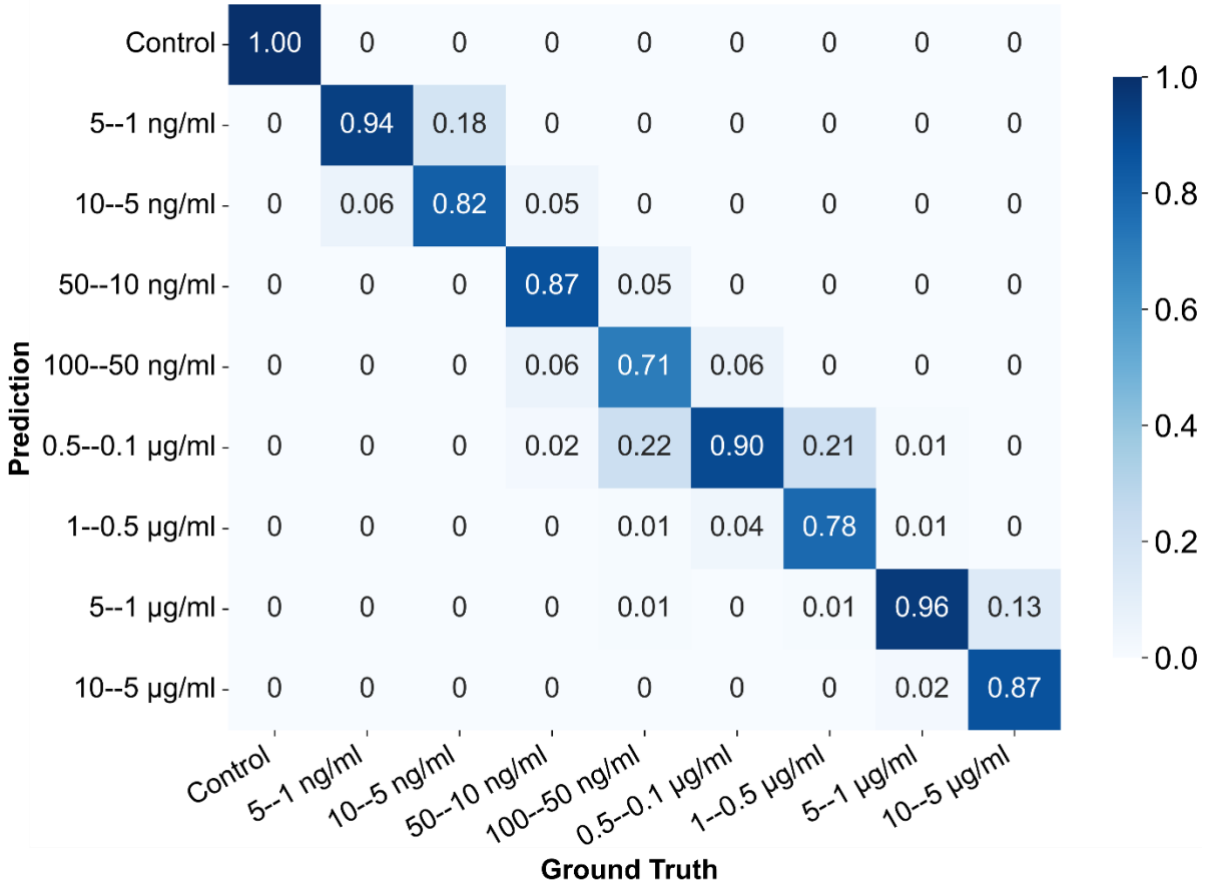

Figure 4.18 Confusion matrix of the trained model performance on validation set.

4.3.6 POC device and mobile phone APP development

The development of the AID-POCT device and its accompanying mobile phone APP is a critical component of this work, aiming to enable rapid and user-friendly cytokine detection. The various aspects of this development have been illustrated, including the workflow of the APP (Figure 4.19), the camera and image display pages of the APP (Figure 4.20), and an exploded view of the POC device components (Figure 4.21).

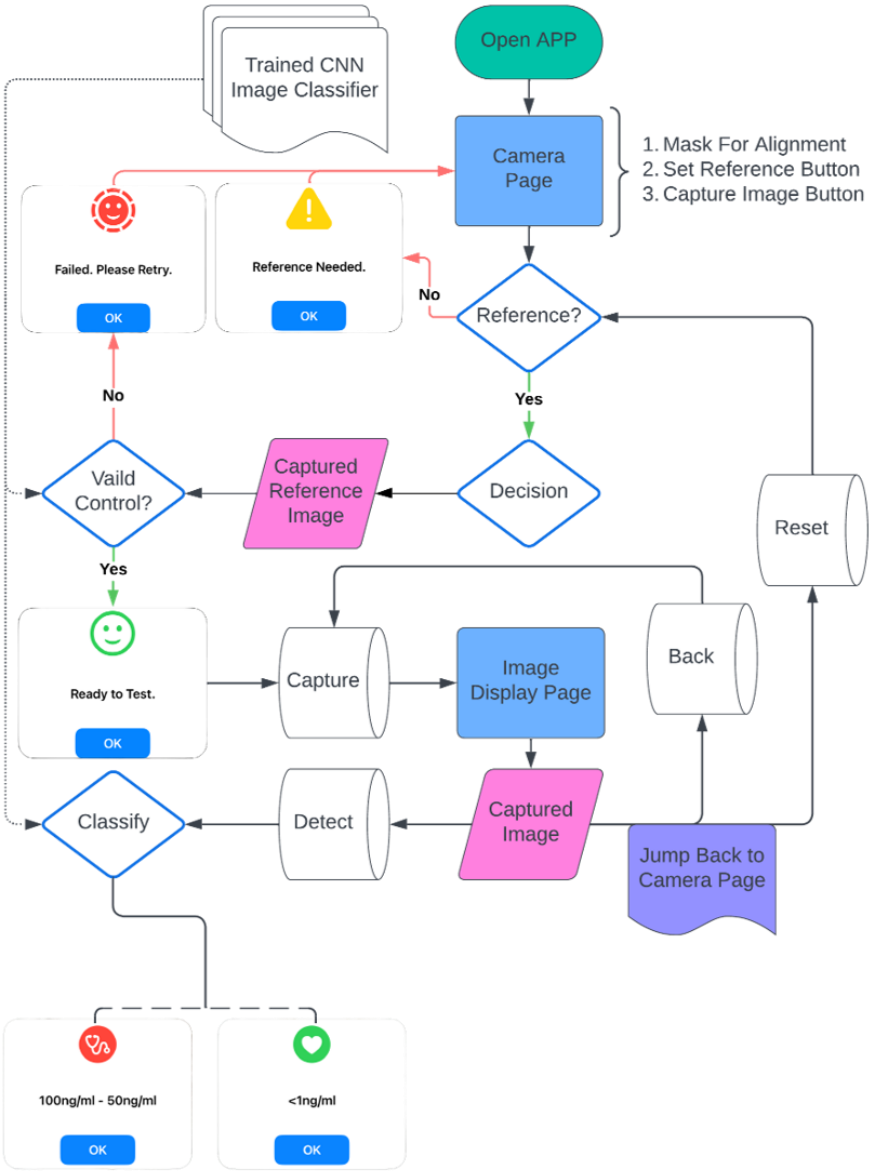

Figure 4.19 Workflow diagram of the mobile APP.

Upon launching the mobile APP, the camera page, which have a central circular mask designed to align with the outer-diameter of 96-well plate wells or the POC wells during image capture, is presented. This alignment is essential for capturing consistent images feeding to the analysis running in the background. The interface on this page includes two buttons: the 'Reference' button located at the top and the 'Capture' button at the bottom of the screen, as shown in Figure 4.20. The 'Reference' button allows users to capture the image of the control sample, which serves as a reference image. A valid reference image should be identified as 'control' by the deployed ML classifier. The 'Capture' button is activated only after capturing a valid reference image. This ensures that the previous sample processing, such as shaking time, is appropriate for analysing. After capturing the image of the sample, the APP transitions to the image display page (Figure 4.20). This page displays the recently captured image and provides three functional buttons for further interaction. The 'Detect' button, located at the bottom left, initiates the concentration prediction by feeding the image to the in-APP ML network and shows the prediction result. The 'Back' button at the top left is for returning to the camera page to retake the test sample image without resetting the reference image, which is useful if the initial capture was misaligned. The 'Reset' button at the bottom right clears the current reference image, allowing users to begin a new test with a different POC chip.

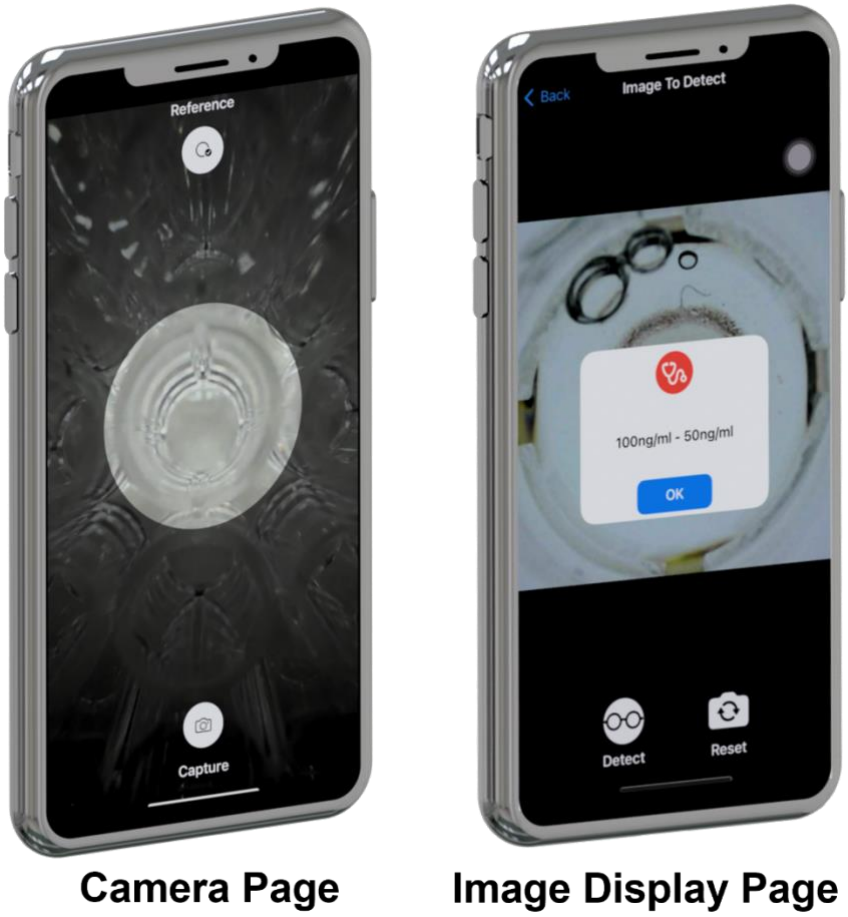

Figure 4.20 Screenshots of the mobile APP interfaces.

The POCT device set, as illustrated in Figure 4.21, comprises several components designed for ease of use and optimal functionality. The main component is the POC wells with a lid, which includes a sampling well where the MB-pAb interact with the test samples and a control well for setting reference. The lid serves to protect the samples from contamination and spill during the shaking process. The MagChip, which is a magnet plate designed with a white background, and a slot specifically for accommodating the chip, facilitates the MBs aggregation process and enhances image contrast during capture. A holder tightly houses the MagChip and aligns it with

the LED pad, which provides uniform illumination from beneath for capturing high-quality images of the MB patterns formed.

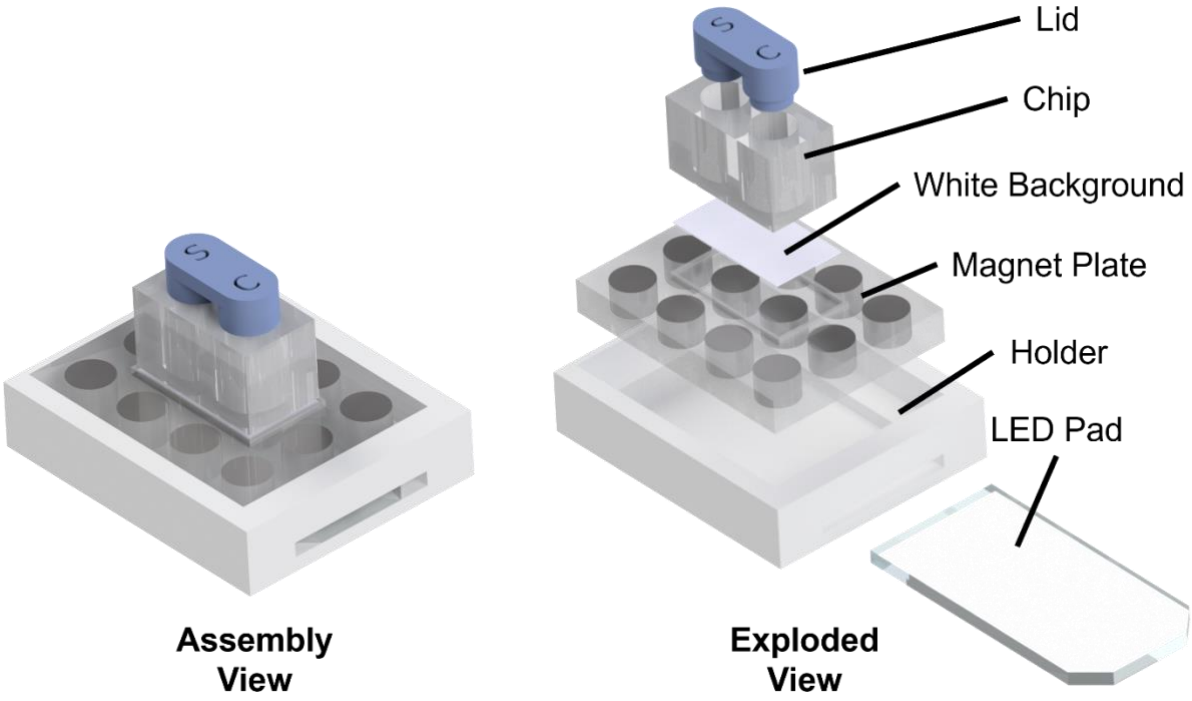

Figure 4.21 Schematic illustration of the POC device components.

For designing the MagChip, to understand the influence of the magnetic field distribution on the MB pattern formation within the POC wells, we conducted simulations of the magnetic field distribution using COMSOL (COMSOL Multiphysics Version 5.6). Figure 4.22 illustrates the simulated magnetic field profiles under two different configurations: one is a central pair of magnets surrounded by additional magnets, and the other is the same central pair of magnets without any surrounding magnets. In our AID-POCT device design, although only two magnets are positioned directly beneath the POC wells and are primarily responsible for inducing the MB pattern formation, the inclusion of surrounding magnets plays a crucial role in achieving a uniform magnetic field across the wells.

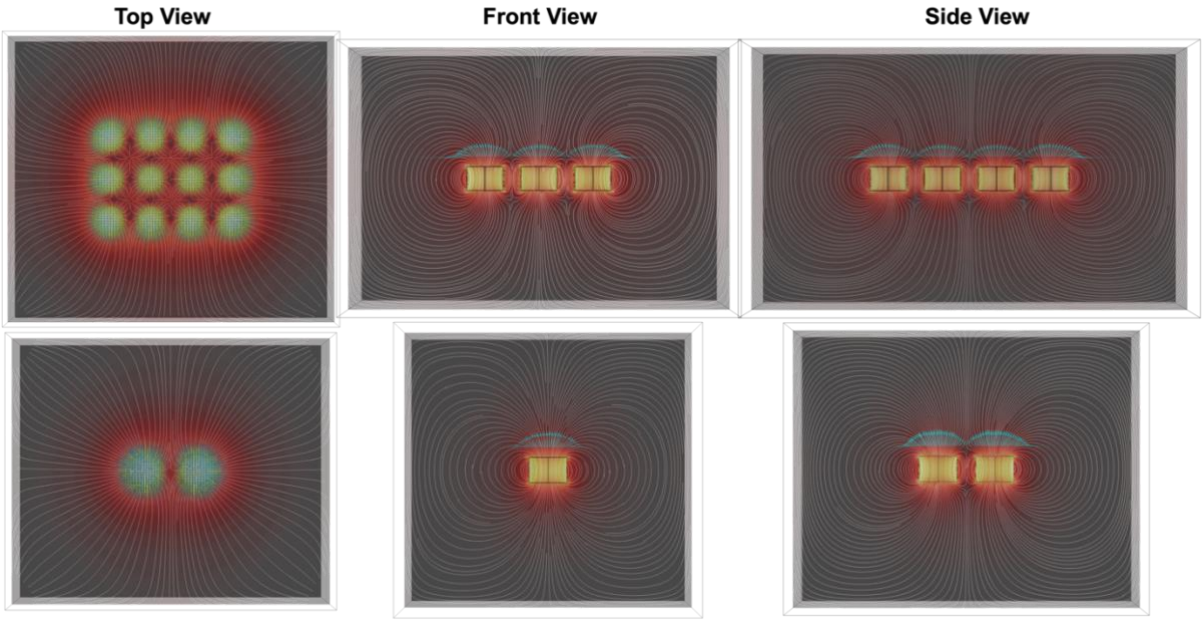

Figure 4.22 Magnetic field simulations.

Magnetic field simulations illustrating the effect of surrounding magnets on field distribution within the POC wells (Top: a central pair of magnets surrounded by additional magnets of the same type and orientation; Bottom: only the central pair of magnets without any surrounding magnets). All magnets used are 6mm (diameter) x 4mm (height) and graded as N52, with the north pole facing upwards from the front view.

The primary function of the central magnets is to generate a magnetic field that influences the MBs within the wells, causing them to aggregate and form patterns indicative of cytokine concentrations. However, when only the central magnets are present, the magnetic field lines exhibit significant distortion at the edges of the magnets. This distorted magnetic field leads to inconsistencies in MB behaviour and pattern formation. By incorporating surrounding magnets with the same polarity orientation as the central magnets, the magnetic field lines become non-distorted and similar within the region of interest—the POC wells. The surrounding magnets

effectively reduce edge effects and magnetic field gradients by providing a more homogeneous magnetic environment. This uniformity results in a more reliable and reproducible pattern formation.

The design of both the AID-POCT device and the mobile APP emphasises user-friendliness, reusability and price-friendliness making the system accessible to more users with minimal training. The integration of the ML network within the APP enhances the diagnostic capability by providing precise quantitative analysis without the need for complex laboratory equipment and a long waiting period. This combination is particularly beneficial in remote or resource-limited settings where traditional laboratory infrastructure is unavailable. A demonstration of how to use the POC device with the phone APP is captured in Movie 5.2.

4.4 Conclusion

In summary, we develop an AID-POCT platform for the rapid (result in ~10 min), quantitative and decentralised detection of biomarkers such as IFN-γ. The AID-POCT platform leverages the formation of distinct MB patterns after applying with magnetic field in response to varying cytokine concentrations, which are captured by the paired pAb conjugating on the MBs. The MB patterns are then captured by a mobile phone camera and analysed by the ML network deployed with the APP in real-time. The platform achieves 87.2% overall ML accuracy on IFN-γ concentration levels based on variations in pattern morphology. Additionally, the development of a user-friendly mobile APP facilitated seamless interaction with the device, guiding users through the testing process and providing near-to-immediate (less than 20 ms) results. This platform ensures its rapidity, classification accuracy, and accessibility by integrating the MB pattern-based assays with POCT device setup and an AI-enabled mobile phone APP. Though the current platform is built for IFN-γ detection, the experiments on TNF-

α proves AID-POCT's biosensing specificity and adaptability, where through changing the pAb conjugation, the platform shows the potential to detect different biomarkers. Despite the current performance limitation of the AID-POCT platform due to a small dataset, with the integration of more high-quality data and continued research and development on the MB pattern-based assays, the AID-POCT platform has the potential to make a transformative impact on POC diagnostics. However, because the present ML model predominantly addresses IFN-γ ranges that may exceed common physiological levels, further refinement and validation remain essential for routine clinical use. Ongoing work will expand the assay's sensitivity to typical concentration ranges, explore alternative biomarkers (*e.g.*, Fetuin-B and CD14), and strengthen the underlying dataset, ultimately positioning the AID-POCT platform for transformative impact in point-of-care diagnostics.

4.5 References

[1] C. Liu, D. Chu, K. Kalantar-Zadeh, J. George, H. A. Young, and G. Liu, "Cytokines: from clinical significance to quantification," *Advanced Science,* vol. 8, no. 15, p. 2004433, 2021.

[2] M. Huse, B. F. Lillemeier, M. S. Kuhns, D. S. Chen, and M. M. Davis, "T cells use two directionally distinct pathways for cytokine secretion," *Nature immunology,* vol. 7, no. 3, pp. 247-255, 2006.

[3] H. Chaudhry *et al.*, "Role of cytokines as a double-edged sword in sepsis," *In vivo,* vol. 27, no. 6, pp. 669-684, 2013.

[4] P. Mehta, D. F. McAuley, M. Brown, E. Sanchez, R. S. Tattersall, and J. J. Manson, "COVID-19: consider cytokine storm syndromes and immunosuppression," *The lancet,* vol. 395, no. 10229, pp. 1033-1034, 2020.

[5] J. B. Moore and C. H. June, "Cytokine release syndrome in severe COVID-19," *Science,* vol. 368, no. 6490, pp. 473-474, 2020.

[6] D. Wakefield and A. Lloyd, "The role of cytokines in the pathogenesis of inflammatory eye disease," *Cytokine,* vol. 4, no. 1, pp. 1-5, 1992.

[7] F. A. Bozza *et al.*, "Cytokine profiles as markers of disease severity in sepsis: a multiplex analysis," *Critical care,* vol. 11, pp. 1-8, 2007.

[8] M. A. Berry *et al.*, "Evidence of a role of tumor necrosis factor α in refractory asthma," *New England Journal of Medicine,* vol. 354, no. 7, pp. 697-708, 2006.

[9] J. Massagué, "TGFβ in cancer," *Cell,* vol. 134, no. 2, pp. 215-230, 2008.

[10] Y. Dowlati *et al.*, "A meta-analysis of cytokines in major depression," *Biological psychiatry,* vol. 67, no. 5, pp. 446-457, 2010.

[11] G. Liu, C. Jiang, X. Lin, and Y. Yang, "Point-of-care detection of cytokines in cytokine storm management and beyond: Significance and challenges," *View,* vol. 2, no. 4, p. 20210003, 2021.

[12] H. Zhu, S. O. Isikman, O. Mudanyali, A. Greenbaum, and A. Ozcan, "Optical imaging techniques for point-of-care diagnostics," *Lab on a Chip,* vol. 13, no. 1, pp. 51-67, 2013.

[13] F. B. Myers and L. P. Lee, "Innovations in optical microfluidic technologies for point-of-care diagnostics," *Lab on a Chip,* vol. 8, no. 12, pp. 2015-2031, 2008.

[14] K. Fan, W. Liu, Y. Miao, Z. Li, and G. Liu, "Engineering Strategies for Advancing Optical Signal Outputs in Smartphone-Enabled Point-of-Care Diagnostics," *Advanced Intelligent Systems,* vol. 5, no. 6, p. 2200285, 2023.

[15] J. Wang, "Electrochemical biosensors: towards point-of-care cancer diagnostics," *Biosensors and Bioelectronics,* vol. 21, no. 10, pp. 1887-1892, 2006.

[16] Y. Wan, Y. Su, X. Zhu, G. Liu, and C. Fan, "Development of electrochemical immunosensors towards point of care diagnostics," *Biosensors and Bioelectronics,* vol. 47, pp. 1-11, 2013.

[17] Y. Dai and C. C. Liu, "Recent advances on electrochemical biosensing strategies toward universal point-of-care systems," *Angewandte Chemie,* vol. 131, no. 36, pp. 12483-12496, 2019.

[18] E. T. da Silva, D. E. Souto, J. T. Barragan, J. de F. Giarola, A. C. de Moraes, and L. T. Kubota, "Electrochemical biosensors in point-of-care devices: recent advances and future trends," *ChemElectroChem*, vol. 4, no. 4, pp. 778-794, 2017.

[19] Y. Zhang and N. Zhou, "Electrochemical Biosensors Based on Micro-fabricated Devices for Point-of-Care Testing: A Review," *Electroanalysis*, vol. 34, no. 2, pp. 168-183, 2022.

[20] S. Campuzano, M. Pedrero, P. Yáñez-Sedeño, and J. M. Pingarrón, "New challenges in point of care electrochemical detection of clinical biomarkers," *Sensors and Actuators B: Chemical*, vol. 345, p. 130349, 2021.

[21] O. Pashchenko, T. Shelby, T. Banerjee, and S. Santra, "A comparison of optical, electrochemical, magnetic, and colorimetric point-of-care biosensors for infectious disease diagnosis," *ACS infectious diseases*, vol. 4, no. 8, pp. 1162-1178, 2018.

[22] J. Budd *et al.*, "Lateral flow test engineering and lessons learned from COVID-19," *Nature Reviews Bioengineering*, vol. 1, no. 1, pp. 13-31, 2023.

[23] N. Jiang *et al.*, "Low-cost optical assays for point-of-care diagnosis in resource-limited settings," *ACS sensors*, vol. 6, no. 6, pp. 2108-2124, 2021.

[24] A. Lafong and E. Crothers, "Simple latex agglutination method for typing pneumococci," *Journal of clinical pathology*, vol. 41, no. 2, p. 230, 1988.

[25] J. Molina-Bolívar and F. Galisteo-González, "Latex immunoagglutination assays," *Journal of Macromolecular Science, Part C: Polymer Reviews*, vol. 45, no. 1, pp. 59-98, 2005.

[26] H.-C. Slotved, M. Kaltoft, I. Skovsted, M. Kerrn, and F. Espersen, "Simple, rapid latex agglutination test for serotyping of pneumococci (Pneumotest-Latex)," *Journal of clinical microbiology*, vol. 42, no. 6, pp. 2518-2522, 2004.

[27] J. Ortega-Vinuesa and D. Bastos-González, "A review of factors affecting the performances of latex agglutination tests," *Journal of Biomaterials Science, Polymer Edition*, vol. 12, no. 4, pp. 379-408, 2001.

[28] B.-I. Haukanes and C. Kvam, "Application of magnetic beads in bioassays," *Bio/technology*, vol. 11, no. 1, pp. 60-63, 1993.

[29] S. Lu and J. Forcada, "Preparation and characterization of magnetic polymeric composite particles by miniemulsion polymerization," *Journal of Polymer Science Part A: Polymer Chemistry*, vol. 44, no. 13, pp. 4187-4203, 2006.

[30] I. Safarik and M. Safarikova, "Magnetic techniques for the isolation and purification of proteins and peptides," *Biomagnetic research and technology*, vol. 2, pp. 1-17, 2004.

[31] S. Wignarajah, G. A. Suaifan, S. Bizzarro, F. J. Bikker, W. E. Kaman, and M. Zourob, "Colorimetric assay for the detection of typical biomarkers for periodontitis using a magnetic nanoparticle biosensor," *Analytical chemistry*, vol. 87, no. 24, pp. 12161-12168, 2015.

[32] J. Schotter, P.-B. Kamp, A. Becker, A. Pühler, G. Reiss, and H. Brückl, "Comparison of a prototype magnetoresistive biosensor to standard fluorescent DNA detection," *Biosensors and Bioelectronics*, vol. 19, no. 10, pp. 1149-1156, 2004.

[33] K. Schroder, P. J. Hertzog, T. Ravasi, and D. A. Hume, "Interferon-γ: an overview of signals, mechanisms and functions," *Journal of Leucocyte Biology*, vol. 75, no. 2, pp. 163-189, 2004.

[34] A. Billiau and P. Matthys, "Interferon-γ: a historical perspective," *Cytokine & growth factor reviews*, vol. 20, no. 2, pp. 97-113, 2009.

[35] F. A. Bozza *et al.*, "Cytokine profiles as markers of disease severity in sepsis: a multiplex analysis," *Critical care*, vol. 11, pp. 1-8, 2007.

[36] W.-q. Diao *et al.*, "Fetuin-B (FETUB): a plasma biomarker candidate related to the severity of lung function in COPD," *Scientific Reports*, vol. 6, no. 1, p. 30045, 2016.

[37] A. G. Rosas-Taraco, A. Revol, M. C. Salinas-Carmona, A. Rendon, G. Caballero-Olin, and A. Y. Arce-Mendoza, "CD14 C (-159) T polymorphism is a risk factor for development of pulmonary tuberculosis," *The Journal of infectious diseases*, vol. 196, no. 11, pp. 1698-1706, 2007.

[38] N. S. Lipman, L. R. Jackson, L. J. Trudel, and F. Weis-Garcia, "Monoclonal versus polyclonal antibodies: distinguishing characteristics, applications, and information resources," *ILAR journal*, vol. 46, no. 3, pp. 258-268, 2005.

[39] A. Frutiger, A. Tanno, S. Hwu, R. F. Tiefenauer, J. Voros, and N. Nakatsuka, "Nonspecific binding—fundamental concepts and consequences for biosensing applications," *Chemical reviews,* vol. 121, no. 13, pp. 8095-8160, 2021.

[40] M. Steinitz, "Quantitation of the blocking effect of tween 20 and bovine serum albumin in ELISA microwells," *Analytical biochemistry,* vol. 282, no. 2, pp. 232-238, 2000.

[41] M. L. Sin, K. E. Mach, P. K. Wong, and J. C. Liao, "Advances and challenges in biosensor-based diagnosis of infectious diseases," *Expert review of molecular diagnostics,* vol. 14, no. 2, pp. 225-244, 2014.

[42] J. Terven, D.-M. Córdova-Esparza, and J.-A. Romero-González, "A comprehensive review of yolo architectures in computer vision: From yolov1 to yolov8 and yolo-nas," *Machine Learning and Knowledge Extraction,* vol. 5, no. 4, pp. 1680-1716, 2023.

5 CHAPTER 5: CONCLUSION AND FUTURE WORK

5.1 Conclusion

This thesis addressed the limitations of traditional detection and monitoring methods, which are often centralised, costly, and time-consuming, by integrating microfluidic technology with image-based machine learning to develop pocket-fit, decentralised platforms capable of detection in environmental and biomedical applications.

Starting with a literature review of previous research findings on intelligent microfluidics, the necessity and potential of using machine learning in microfluidics is explored. The literature review highlights intelligent microfluidics' ability to generate diverse datasets and process them using machine learning to produce innovative solutions. Despite promising applications of intelligent microfluidics in various disciplines, challenges such as ensuring accuracy in complex environments, dealing with uneven data volumes, enhancing automation, increasing acceptance, and improving computing capabilities in mobile devices are identified.

Focusing on expanding the intelligent microfluidics platform-based detection in environmental monitoring to offer a on-site replacement to the traditional microalgae detection and monitoring methods, an Automated and Intelligent Microfluidic Platform (AIMP) is presented. The AIMP combines a USB microscope with laser-cut microfluidic chips and a compact motorised stage, creating a backpack-fit yet functional system. The platform is validated using four microalgae species of varying sizes and morphologies, achieving a mean average precision (mAP@0.5) of 92.8% with the trained machine learning model based on the YOLOv5 architecture. The AIMP demonstrates high accuracy in species detection and counting, as well as in classifying the growth stages of microalgae, which is crucial for ecological studies and commercial applications. An accompanying Raspberry Pi APP is developed to enhance user accessibility, facilitating on-site environmental monitoring with minimal expertise required.

Based on a similar development path, an Artificial Intelligence-Driven Point-of-Care Testing (AID-POCT) platform for cytokine detection is introduced, which not only focuses on increasing automation, but also emphasises finding a new pattern morphological-based method to better utilise captured image to copy with complex test environments. Recognising the critical role of cytokines in immune responses and the limitations of conventional detection methods, the AID-POCT platform offers a rapid (result in ~10 mins), quantitative, and decentralised solution. It employs magnetic microbeads coated with specific antibodies to capture target cytokines, forming distinct patterns under a magnetic field in response to varying concentration levels. These patterns are captured using a mobile phone camera and analysed in real-time through a machine learning model deployed within a user-friendly mobile APP. The platform achieves an overall ML classification accuracy of 87.2% for interferon-gamma (IFN-γ) detection and demonstrates adaptability by successfully detecting tumour necrosis factor-alpha (TNF-α), indicating the potential for detecting other biomarkers.

Collectively, the thesis demonstrates the feasibility and effectiveness of integrating microfluidics with image-based machine learning to develop backpack-fit, cost-effective, and rapid detection platforms. These intelligent microfluidic systems address the critical need for decentralised diagnostics in environmental monitoring and healthcare, offering advancements over traditional methods. The findings contribute to the field by showcasing practical implementations that overcome common limitations, paving the way for broader adoption of intelligent microfluidics across various disciplines.

5.1.1 Alignment with objectives

(a): Investigate and identify knowledge and application gaps in intelligent microfluidics.

Achievement: Chapter 3 provided a thorough review of advancements since 2017, clearly identifying gaps such as the need for portable, cost-effective intelligent microfluidic platforms.

(b): Develop a compact (fits into a 10-litre backpack) and low-cost (<£200) automated intelligent microfluidic platform.

Achievement: As detailed in Chapter 4, the developed AIMP successfully met these criteria with total component costs of approximately £170 and a compact footprint of approximately 14×16×28 cm.

(c): Integrate ML models on source-constrained hardware to enable real-time (<100 ms) classification and detection.

Achievement: Both Chapter 4 (YOLOv5-based microalgae detection running on Raspberry Pi) and Chapter 5 (smartphone-based microbead immunoassay classification) demonstrated real-time processing, consistently achieving inference times much under 100 ms per image on edge devices.

(d): Validate environmental application feasibility with microalgae monitoring, achieving >80% detection accuracy.

Achievement: The AIMP platform showed high overall accuracy, with species-level detection achieving 87–94% accuracy (mAP@0.5 approximately 92.8%), successfully meeting the stated benchmark.

(e): Develop a rapid (<10 min) microbead-based immunoassay module leveraging ML-detectable pattern formation.

Achievement: Chapter 5 demonstrated the assay's completion in approximately 10 minutes, achieving an overall ML accuracy of 87.2% in classifying IFN-γ concentration levels, matching the resulting speed of typical LFAs.

5.1.2 Findings

- Cost-effective, accessible platform:

Successfully demonstrated that a robust and functional microfluidic system can be constructed with commercially available, inexpensive components, achieving quantitative objectives such as cost and size.

- Real-time ML integration:

Validated the practicality of deploying powerful ML algorithms with deep neural networks on resource-constrained hardware (without professional GPUs) with inference times consistently below 100 ms and with overall model detection or classification accuracy >85%, clearly meeting the quantitative targets outlined.

- Adaptability and versatility:

The AIMP successfully identified multiple microalgae species and tracked physiological changes over extended periods (*e.g.*, astaxanthin production in *Haematococcus pluvialis* over 30 days).

The AID-POCT demonstrated capability in rapidly quantifying IFN-γ and showed adaptability to other cytokines such as TNF-α through simple antibody substitutions, validating flexibility and specificity.

5.1.3 Limitations and possible methodological improvements

- Dataset size and quality:

Limited dataset size restricted robust statistical confidence. Future improvements include significantly expanding the datasets, incorporating multiple replicates, and enhancing the data diversity to minimise model overfitting and enhance generalisability.

- Detection range sensitivity:

Current immunoassay configuration targets high physiological concentrations of IFN-γ. Further methodological refinement is necessary to reliably detect lower, clinically relevant ranges (picogram-per-millilitre levels) with enhanced antibody affinity or assay chemistry. Additionally, it is worthwhile exploring other biomarkers such as Fetuin-B and CD14, whose clinically meaningful testing ranges are already within the detection capabilities of our current AID-POCT system.

- Lack of a golden standard benchmark:

A significant challenge identified during the research in this field is the current lack of a universally accepted 'gold standard' benchmark dataset for intelligent microfluidic applications, like Large Language Model (LLM) Benchmark. This absence limits direct objective comparisons and the ability to robustly assess the performance and reliability of newly

developed methods. Establishing comprehensive benchmark datasets or standardised testing protocols would greatly enhance comparative studies and support iterative improvement within this emerging field.

5.2 Future Work

Building upon the findings and acknowledging the limitations of the current research, several avenues for future work are proposed:

1. Enhancing dataset quality and quantity

While the current performance of machine learning models deployed to the AIMP and AID-POCT platforms is achieves overall accuracy >85%, both are trained and tested on relatively small datasets. Expanding the dataset is crucial to improving accuracy and robustness. Collecting more diverse and larger amounts of samples helps the model generalise better to real-world scenarios. In addition to data augmentation, which is used in AIMP and AID-POCT development, techniques such as synthetic data generation and collaborative data sharing are also important methods to improve the dataset size and diversity.

2. Expanding applications and adaptability

Exploring new applications for the intelligent microfluidic platform can demonstrate its versatility, thereby facilitating the promotion of this research direction and increasing interdisciplinary recognition. For the AIMP, its use can be expanded to detect other microorganisms or environmental pollutants. For the AID-POCT platform, it shows a great potential to detect a wider range of biomarkers, including nucleic acids or metabolites. Additionally, optimising the size of the magnetic beads and adjusting the type and amount of surfactants in the buffer used in the AID-POCT can potentially increase MB pattern formation sensitivity and enhance the capability to detect biomarkers in complex biofluids such as serum.

3. Enhancing platform automation and user experience

Further automation of the platforms can reduce the need for user intervention and minimise potential errors. Integrating advanced hardware components, such as automated sample handling and integrated sensors, can streamline the workflow. Additionally, despite the development of user-friendly apps, they may still be difficult for end users who are not familiar with such technology or who cannot access them using visual guides. This directly reduces the audience for AID-POCT in particular. More intuitive and diverse interaction methods and sufficient user guidance are essential for practical application.

6 APPENDIX A: SUPPORTING VIDEOS

Movie 4.1 Platform Moving Stability Test

Movie 4.2 AIMP Testing and APP Demonstration

Movie 5.1 Dynamic Process of MBs' Moving with Magnets Applied

Movie 5.2 AID-POCT Testing and Mobile APP Demonstration